

The Pennsylvania State University
The Graduate School
Department of Mechanical and Nuclear Engineering

**MICROWAVE PLASMA TORCH
FOR ALUMINUM COMBUSTION**

A Thesis in
Mechanical Engineering
by
Michael Anthony Vamos

Submitted in Partial Fulfillment
of the Requirements
for the Degree of

Master of Science

August 2018

The thesis of Michael Anthony Vamos was reviewed and approved* by the following:

Richard Yetter
Professor of Mechanical Engineering
Director of the Kuo High Pressure Combustion Lab
Thesis Advisor

Stefan Thynell
Professor of Mechanical Engineering

Sean Knecht
Assistant Teaching Professor
School of Engineering Design, Technology and Professional Programs

Sven G. Bilén
Professor of Engineering Design, Electrical Engineering, and Aerospace
Engineering

Karen Thole
Department Head of Mechanical and Nuclear Engineering
Distinguished Professor of Mechanical Engineering

*Signatures are on file in the Graduate School

ABSTRACT

Aluminum particles can be used as a fuel source in combustion systems. Breaching the protective oxide shell is critical in the initiation of the particle's combustion, since the aluminum center cannot react until the shell is cracked or vaporized. Microwave plasma torches have been shown to be effective at igniting various fuels, including aluminum. This work investigates workable conditions of a coaxial microwave plasma torch for igniting aluminum powder. The plasma filament and aluminum particle interaction were also investigated.

An argon plasma was formed in a coaxial torch and aluminum particles were passed through the filaments without any oxidizer. Through the use of spectroscopy, aluminum and aluminum oxide spectral peaks were observed. The post-plasma particles were collected and observed using a scanning electron microscope, showing that many particles were fused together. A plasma temperature fitting was performed with Specair showing an approximate temperature between 2500–3400 K.

Combustion tests were performed using air, steam, and carbon dioxide as oxidizers. Combustion was achieved with all three oxidizers. The aluminum–air flame produced a stable and anchored flame. Aluminum–steam also produced a favorable anchored flame; however, it was not repeatable. Aluminum–carbon dioxide reacted with a small flame. Further tests with carbon dioxide still need to be performed.

The aluminum–air flame was characterized over several equivalence ratios. The flame was anchored at the injector tip for lean and near stoichiometric conditions. Fuel-rich experiments still burned; however, the flame was thinner at the injector tip. For the lean and near stoichiometric conditions, the microwave power was able to be turned off after combustion began.

The most stable configuration for the coaxial microwave plasma torch for igniting aluminum was: Equivalence ratio of 0.9 , annulus velocity of 8.8 m/s (10° swirl), core flow velocity of 1.0 m/s, and 200 W of microwave power with air in the outer flow and argon and aluminum powder in the core flow.

TABLE OF CONTENTS

List of Figures.....	vii
List of Tables.....	xii
Nomenclature	xii
Acknowledgments	xiv
Chapter 1 Introduction	1
Aluminum Plasma Torch Applications	2
Aluminum Combustion Fundamentals	2
Thesis Goals.....	3
Thesis Organization.....	4
Chapter 2 Literature Review	5
Previous Aluminum Combustion Research	5
Diffusion vs. Kinetic Regimes.....	6
Particle Size Trends	7
Flame Structure of Aluminum.....	7
Choice of Experimentation.....	9
Aluminum–Air Mechanism.....	11
Aluminum–Steam Mechanism	12
Plasmas	12
Plasma-Assisted Combustion	14
Effect of Plasma on H ₂ –O ₂ Mechanism	15
Microwave Torch.....	15
Spectroscopy.....	18
Argon	19
Steam	20
Aluminum and Aluminum Oxide	21
Temperature Fitting	22
Aluminum Particle Burning Temperature.....	23
Past Work on Plasma-Assisted Combustion.....	24
Coaxial Fluid Flows	26
Chapter 3 Equipment List	28
Microwave Generation	29
Burner and Injector.....	31
Fluid Flows.....	38
High Velocity Aluminum Feeder and Shearing Device.....	42
Calibration of High Velocity Feeder.....	44
Low Velocity Aluminum Feeder	45
Cameras.....	46
Spectroscopy	47

Ventilation.....	49
LabVIEW	50
Addressing Safety	51
Chapter 4 Experimental Development	53
Single Tube Injector	53
Coaxial Injector.....	58
Plasma	60
Aluminum Through an Argon Plasma	68
High Velocity Feed System Combustion Tests	75
Chapter 5 Results — Low Velocity Aluminum Feed	80
Aluminum Through Argon Plasma — Low Velocity Feeder	83
Aluminum—Steam — Low Velocity Feeder	84
Aluminum—Air Combustion Tests	90
Effect of Stoichiometry	92
Premix Configuration.....	96
Aluminum—CO ₂ Combustion Tests	97
Particle Temperature Fitting.....	98
Effect of Microwave Power on the Flame.....	104
Chemical Equilibrium Analysis.....	107
Plasma Temperature Fitting	109
XRD	110
Chapter 6 Conclusions and Future Work	112
Conclusions	112
Future Work	114
References	116
Appendix A Aluminum – Steam Combustion Checklist.....	119
Appendix B Aluminum – Air Procedure	122
Appendix C Thermal Fitting Code.....	124
Appendix D Calibrating a Spectrometer Using the Tungsten Filament Lamp at the HPCL	126

LIST OF FIGURES

Figure 2-1. Aluminum-air Luminous Region at 2 and 60 atmospheres ¹⁶	8
Figure 2-2. Comparing Flame Structure for Air and Steam ¹⁶	9
Figure 2-3. Diagram of a Burner Attached to a Waveguide and Containing a Spacer for Adjusting Microwave Coupling	17
Figure 2-4. ANSYS HFSS Simulation of a Coaxial Injector Performed by Palomino ⁴¹	18
Figure 2-5. OH Radical Present From Steam Introduction to a Plasma.....	21
Figure 2-6. Palomino's Plasma Torch Configuration ⁴¹	25
Figure 3-1. Overall Schematic of Major Experimental Components.....	28
Figure 3-2. SGP-15AC DC High-Voltage Module Used to Provide Power to the Daihen SGM-15A Magnetron.....	29
Figure 3-3. Major Components of Burner Attached to the Waveguide	32
Figure 3-4. Aluminum Burner Connected to the Waveguide.....	33
Figure 3-5. Inner Tubing with Upper Adapting Unions.....	34
Figure 3-6. Location of Spacer and Resonant Cavity	35
Figure 3-7. Outer Tubing, Top Plate, Clamp, and 0.5" Swagelok Tee	36
Figure 3-8. Section View of Outer Tubing, Top Plate, Clamp and Inner Tubing	36
Figure 3-9. Section View of Mixing Tee and Inner and Outer Tubing.....	37
Figure 3-10. Boiler.....	39
Figure 3-11. Path of Steam Generation.....	40
Figure 3-12. Shearing Device Components for High Velocity Aluminum Feeder ⁴⁴	42
Figure 3-13. Electric Cylinder and Aluminum Cartridge Without Shearing Device.....	43
Figure 3-14. Schematic of High Velocity Aluminum Feeder and Shearing Device ⁴⁴	43
Figure 3-15. Calibration of Aluminum Mass Flow Rate for High Velocity Aluminum Feeder	44
Figure 3-16. Low Velocity Aluminum Feeder Cross Section	45
Figure 3-17. Phantom v7.3 Camera	47

Figure 3-18. HR 4000 Spectrometer	48
Figure 3-19. Example of Ocean Optics Computer Interface with Combustion Spectra Collected from HR 4000.....	48
Figure 3-20. Spectrometer Component Layout	49
Figure 3-21. Water Bucket and Ventilation System	49
Figure 3-22. LabVIEW Graphical User Interface for Microwave Power and Aluminum Feed Control	50
Figure 3-23. Main Components of LabVIEW Code.....	51
Figure 3-24. NARDA meter and Particle Respirator	52
Figure 4-1. Upright Atmospheric Argon Plasma: 1 SLM Argon, 200 W of Microwave Power.....	54
Figure 4-2. Inverted Single Tube Plasma Torch.....	55
Figure 4-3. Inverted Argon Plasma with Noticeable Recombination Zone	55
Figure 4-4. Argon Plasma: 2 SLM; Power = 100 W, 300 W, and 500 W (from left to right).....	56
Figure 4-5. Steam Plasma Filament: 1 g/s, 500 W of Microwave Power	57
Figure 4-6. Steam Plasma Filament: 1 g/s, 500 W of Microwave Power (colorized).....	57
Figure 4-7. Premixed Coaxial Injector Flows	59
Figure 4-8. Electromagnetic Simulation Performed by Palomino at the Applied Research Lab for the Coaxial Injector.....	60
Figure 4-9. Coaxial Injector Argon Plasma Displaying Multiple Filaments: 10 SLM of Argon Through Annulus, 300 W Microwave Power.....	61
Figure 4-10. Increased Intensity Varying Microwave Power for an Argon Plasma: 10 SLM — 200 W (blue), 300 W (red), 400 W (yellow), 500 W (purple), 600 W (green)	62
Figure 4-11. Argon Plasma with Entrained Steam: 10 SLM of Argon in the Annulus, 1 g/s Steam, 750 W.	63
Figure 4-12. Argon Plasma with Entrained Steam: 10 SLM of Argon in the Annulus, 1 g/s Steam, 750 W (colorized).....	63
Figure 4-13. Argon Plasma with Carrier Gas: 10 SLM of Argon in the Annulus, 30 SLM Argon Carrier Gas in the Core Flow, 300 W of Microwave Power	64

Figure 4-14. Progression of a Plasma: 10 SLM of Argon Annular Flow, 1 g/s of Steam and 800 W Microwave Power — 2 ms Between Frames	65
Figure 4-15. Comparison of Argon Plasma Spectra with and without Entrained Steam — No Steam (blue), With Steam (orange)	65
Figure 4-16. OH Radical Increase in Intensity When Steam Is Entrained — No Steam (blue), With Steam (orange)	66
Figure 4-17. H-Alpha Emission Present When Steam Is Entrained — No Steam (blue), With Steam (orange)	67
Figure 4-18. Oxygen Radical Emission Present When Steam Is Entrained — No Steam (blue), With Steam (orange)	67
Figure 4-19. Aluminum Powder Passing Through an Argon Plasma — 300 W and 0.1 g/s of Aluminum.....	68
Figure 4-20. Comparison of Argon Plasma (Blue) and Aluminum Passing Through an Argon Plasma (Orange): 7.5 SLM of Argon Plasma Gas, 1.9 SLM Nitrogen Swirl, 0.1 g/s of Aluminum, 30 SLM Argon Carrier Gas, and 300 W of Microwave Power.	69
Figure 4-21. Aluminum and Aluminum Oxide Spectra: 7.5 SLM of Argon Plasma Gas, 1.9 SLM Nitrogen Swirl, 0.1 g/s of Aluminum, 30 SLM Argon Carrier Gas, and 300 W of Microwave Power.....	70
Figure 4-22. Aluminum Passing Through Aluminum Plasma (Monochrome)	71
Figure 4-23. Large Agglomerations of Aluminum Collected After the Plasma 125× Magnification.....	72
Figure 4-24. Large Agglomerations of Aluminum Collected After the Plasma 250× Magnification.....	73
Figure 4-25. Close-up of Small Aluminum Particles Surface After Plasma 2000× Magnification.....	74
Figure 4-26. Combustion Test 4—H-Alpha Filter.....	77
Figure 4-27. Combustion Test 22 Propagation of Aluminum–Steam Flame — 2.5 ms Between Each Frame.....	78
Figure 4-28. Combustion Test 23 Propagation of Aluminum–Steam Flame — 2.5 ms Between Each Frame.....	79
Figure 5-1. Non-premixed Flow Configuration Used with Low Velocity Aluminum Feeder	81
Figure 5-2. Aluminum Passing Through an Argon Plasma and Reacting with Surrounding Air	84

Figure 5-3. Combustion Test 29 — Aluminum—Steam Continuous Flame — 2.5 ms Between Frames	85
Figure 5-4. Combustion Test 5 Attempt 4.....	87
Figure 5-5. Combustion Test 6 Attempt 4.....	88
Figure 5-6. Combustion Test 6 Attempt 4 Spectra Showing Tubing Reactions.....	88
Figure 5-7. Damaged Stainless Steel Tubing from a Stagnant Plasma Filament	89
Figure 5-8. Ignition Sequence of Aluminum–Air Flame — Combustion Test 34 — 2.5 ms Between Frames	91
Figure 5-9. Steady State Aluminum–Air Flame — Combustion Test 34 — 2.5 ms Between Frames	92
Figure 5-10. Combustion Test 38 — $\phi = 0.6$ — 2.5 ms Between Frames.....	94
Figure 5-11. Combustion Test 35 — $\phi = 0.9$ — 2.5 ms Between Frames.....	94
Figure 5-12. Combustion Test 40 — $\phi = 1.6$ — 2.5 ms Between Frames	95
Figure 5-13. Combustion Test 39 — $\phi = 0.9$ — 2.5 ms Between Frames	95
Figure 5-14. Combustion Test 39 — $\phi = 0.6$ — 2.5 ms Between Frames	96
Figure 5-15. Propagation of Premixed Aluminum — Air Flame Showing Shock Tube- Like Propagation — Premixed 3 — 2.5 ms Between Frames	97
Figure 5-16. Aluminum—CO ₂ Flame — Combustion Test 37 — $\phi=2.2$ — 2.5 ms Between Frames.	98
Figure 5-17. Example of Collected Raw Spectra — Combustion Test 35.....	100
Figure 5-18. Corrected Singular Spectra for Non-linearity — Combustion Test 35	101
Figure 5-19. Thermal Emission Fitting of Equation	101
Figure 5-20. Temperature Output for Each Spectra — Combustion Test 35	102
Figure 5-21. Shifting of Aluminum—Air Flame after Stopping Microwave Power — Combustion Test 17 — 2.5 ms Between Frames	105
Figure 5-22. Combustion Test 31 — First Two Images with Microwave Power (200 W) Second Two Images No Microwave Power — 2.5 ms Between Frames	106
Figure 5-23. Combustion Test 31 — Temperature Difference with and Without Microwave Power.	107

Figure 5-24. Example of Fitted Spectra in Specair — Raw Data (Black) and Fitted Curve (Blue).....	109
Figure 5-25. XRD Results from Raw Aluminum Sample.....	111
Figure 5-26. XRD Results from Burnt Combustion Products — Combustion Test 39	111

LIST OF TABLES

Table 2-1. Argon, Oxygen and Nitrogen Optical Emission Wavelength Used for Spectroscopy ³⁴	20
Table 3-1. Remote Pinout of SGP-15 AC DC High-Voltage Module	30
Table 4-1. High Speed Feeder Combustion Tests	76
Table 5-1. Low Velocity Feeder Combustion Test Matrix	82
Table 5-2- Various Low Velocity Feed Steam Tests	86
Table 5-3. High Speed Feeder Aluminum – Steam Test’s Average Temperature.....	103
Table 5-4. Low Velocity Feeder Test’s Average Temperature (Kelvin)	103
Table 5-5. CEA Reactants and Products for Combustion Test 29-35.....	108

NOMENCLATURE

c_0	Speed of Light
C_1	Constant 1
C_2	Constant 2
D	Diffusivity
d	Diameter of Particle
Da	Damkohler Number
G_f	Free Energy
H	Enthalpy
h	Planck's Constant
$H_{\text{vap-dis}}$	Heat of Vaporization-Dissociation
$H^o_{T,\text{vol}}$	Enthalpy at Volatilization Temperature
i	Intensity
K	Kelvin
k_B	Boltzmann Constant
k_s	Heterogeneous Specific Reaction Rate
L	Plasma Length Scale
p	Pressure
\dot{m}	Mass Flow Rate
$m_{\text{o}\infty}$	Mass Burning Rate
N_D	Number Density
n_e	Number Density of Electrons
psi	Pound Per Square Inch
q_e	Charge of an Electron
Q_R	Heat of Reaction
r_s	Radius of Solid
S_{ij}	Stress Tensor
T_e	Temperature of Electron
$t_{b,\text{kin}}$	Kinetic Burning Time
u	Fluid Velocity
u_1	Core Flow Velocity
u_2	Annular Flow Velocity
β	Burning Rate
ε	Emissivity
ε_0	Emissivity of Free Space
λ	Wavelength
λ_D	Debye Length
μ	Dynamic Viscosity
ρ_s	Density of Solid
τ	Collision with Neural Molecules
ϕ	Equivalence Ratio
ω	Plasma Oscillation Frequency

ACKNOWLEDGMENTS

I would like thank all of those who helped and supported me in graduate school and in writing this thesis. First, I would like to thank Penn State's Applied Research Lab and those involved with the Walker Graduate Fellowship. The support of ARL, both on the project and for me financially, have significantly improved my graduate school experience. To my academic advisor, Dr. Richard Yetter, for accepting me as an advisee and guidance throughout my time here. To Dr. Stefan Thynell for being my reader for this thesis. I appreciate you both taking the time to read this. To the project PI, Dr. Sean Knecht, thank you for choosing me for the project, always bringing a positive outlook to the project, and assistance with plasmas and optics. Dr. Eric Boyer, thank you for the assistance with the lab equipment, input on the project and always helping dive into a repair project (there were many). Special thank you to Jorge Palomino for his extensive help with the project. His past knowledge and technical contributions of the coaxial injector and microwave coupling simulation significantly improved the project. Thank you to Dr. Nathan Kempema for rewriting the thermal temperature fitting code for the flame temperature. To Dr. Sven Bilén for his support with equipment donations and electrical knowledge. To Jon Peters, thank you for being a good manager and for your input on the project. Also, thank you to those at ARL that I have come into contact with; Angus, Eric, Bella and Audie. Thank you to those at the KHPCL that have assisted me on the project. Specifically, Skylar Schirtzinger for showing me the ropes around the lab and Eric Yang for his assistance with experimentation.

Finally, I would like to thank my parents, Karen and George Vamos, for encouraging me to attend graduate school. Attending Penn State was a great choice and I am thankful for the opportunity. Thank you for always being a vent when the project hit a rough spot and for all the support throughout my life.

Chapter 1

Introduction

Combustion systems historically have been one of the most common ways to extract energy from fuel to power machines. A majority of combustion systems operate on hydrocarbon or other gaseous fuels. Coal, a solid, has been burned for electricity production and warmth for centuries.¹ In the search for alternatives to hydrocarbons and coal, metal combustion has been considered due to metals being energy dense.² Aluminum has been previously used in solid rocket motors to decrease instabilities in burning.³ Aluminum is favorable as a fuel for its energetic, density, and cost characteristics. Conversely, metals are more difficult to burn than hydrocarbons and often need a turbine to extract power from the products.

Commonly, micron-sized particles have been used in aluminum combustion,⁴ although nanoparticles⁵ have been investigated as an additive to increase the burn rate. Various oxidizers have also been tested with aluminum, most frequently air, H₂O, and CO₂. Some advantages of aluminum as a fuel are that in particulate form it is relatively inert, it has a high volumetric energy density, and its products of combustion are considered eco-friendly and can even be used for further energy harvesting (e.g., for generating hydrogen). The oxide shell that provides the inertness of the particle also increases the difficulty of ignition, making aluminum much more difficult to ignite than other gaseous fuels like hydrocarbons.⁴ An important step in achieving a successful aluminum combustor is the ability to initially ignite the particles. A microwave plasma torch has been shown to be able to ignite aluminum powder with steam. This work determines a useful set of flow conditions for a microwave coaxial plasma torch for ignition. Additionally, the basics behind the plasma filament and aluminum particle interactions is explored.

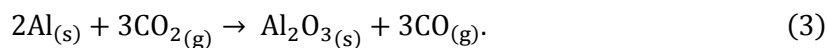
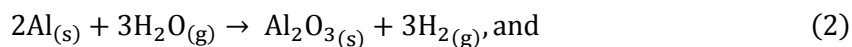
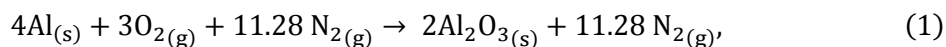
Aluminum Plasma Torch Applications

Aluminum combustion has a specific energy (mass based) that is comparable to other fuels; however, its energy density (volumetric) makes it a favorable choice for fuel. For underwater applications, volume is the critical parameter when engineering the overall system. Additionally, as (sea)water would surround any underwater application, the vehicle would not need to carry oxidizer. (Sea)water can be converted into steam, a possible oxidizer, for combustion. These factors have led aluminum fueled underwater vehicles to be proposed.^{6,7}

It has been proposed that a similar underwater system, the Stored Chemical Energy Power System (SCEPS), possibly could be used for a Venus surface mission.⁸ Potentially, aluminum–CO₂ could also be used for long-term refueling missions on Mars since CO₂ could be harvested from Mars' atmosphere and aluminum ore could be extracted from the soil. Burning aluminum could also provide an additional energy source for Martian colonists.

Aluminum Combustion Fundamentals

Fundamentally, aluminum reacts with air, steam, and CO₂ in the following global reactions:



In Reaction 1, aluminum reacts with the oxygen in air to produce aluminum oxide (enthalpy of formation = -1675 kJ/mol) and left over nitrogen gas from the air. Reaction 1 has a standard enthalpy of reaction of -3351 kJ/mol. Reaction 2 shows that, when aluminum reacts with steam (enthalpy of formation = -241 kJ/mol), aluminum oxide and hydrogen gas are formed. Reaction 2

has a standard enthalpy of reaction of -950 kJ/mol. Additionally, Reaction 3 states aluminum and carbon dioxide (enthalpy of formation = -393 kJ/mol) form aluminum oxide and carbon monoxide. There are various forms of Reaction 3; however, for this application, this was the most appropriate reaction as it is unlikely that pure carbon would be formed as a product. Reaction 3 has a standard enthalpy of reaction of -495 kJ/mol.

Aluminum has a heat of oxidation of 85 kJ/cm³, which is lower than boron (140 kJ/cm³), beryllium (120 kJ/cm³), titanium (90 kJ/cm³), and tungsten (90 kJ/cm³). Aluminum is higher than carbon (75 kJ/cm³), iron (60 kJ/cm³), lithium (20 kJ/cm³), and magnesium (50 kJ/cm³). Although other metals have better heats of oxidation, aluminum is relatively common and cheaper than other alternatives.

Thesis Goals

The goals of this thesis work are to:

- Further investigate the functionality and operable conditions of a microwave plasma torch specifically for igniting aluminum powder;
- To investigate the effect of different oxidizers on both the plasma behavior and combustion effectiveness;
- To determine how an aluminum particle is affected after passing through a plasma filament;
- To determine if a configuration for use as an igniter would be possible or practical;
- To determine if the microwave power can be turned off after ignition and have a flame continue to burn; and
- To understand how the plasma affects the flame structure.

Thesis Organization

In Chapter 2, a summary of relevant literature is provided. The review begins with past research on aluminum combustion that includes the realization that the oxide shell is very important to the burning mechanism, kinetic vs. diffusion regime, burning time, flame structure, dust cloud experiments, and chemical mechanisms for various oxidizers. Chapter 3 describes the equipment used for experimentation. Chapter 4 follows the experimental development for achieving a working coaxial plasma burner, beginning with a single tube injector with which just an argon plasma was formed. Other efforts to find potential solutions are also described: forming a solely steam plasma; the introduction of the coaxial design; plasma formation in the coaxial design; change in spectra due to steam addition; and aluminum passed through an argon plasma. Chapter 5 explains the various tests and summarizes the results from the collected information. Chapter 6 finalizes conclusions made from the work completed and suggests further questions that can be explored in the field.

Chapter 2

Literature Review

Previous Aluminum Combustion Research

Aluminum combustion research began in the late 1950s when metal particles were being considered for additives to solid rocket motors. Glassman⁴ recognized that the oxide shell melting temperature and the melting temperature of the raw metal were important in determining the burning mechanism. The melting point of aluminum oxide is ≈ 2300 K, whereas the boiling point of aluminum oxide is 2791 K. The melting point of aluminum is much lower, 930 K. It can be determined whether metals burn in the vapor phase or heterogeneously by examining the properties of the metal itself and the metal oxide that surrounds the particle. The heat of vaporization-dissociation, $\Delta H_{\text{vap-diss}}$, limits the flame temperature since it is greater than the enthalpy available, $\Delta H_{\text{available}}$.⁹ The enthalpy available is the heat of reaction, Q_R , minus the enthalpy required to raise the temperature to the volatilization point of the oxide, i.e.,

$$\Delta H_{\text{vap-diss}} > Q_R - (H^0_{T,\text{vol}} - H^0_{298\text{K}}) = \Delta H_{\text{available}}. \quad (4)$$

Metal particles like boron, silicon, and zirconium have higher boiling points than their oxide shell. Therefore, they burn heterogeneously with the oxide layer first and then expose the inner metal.⁹ Particles like aluminum, magnesium, and lithium have lower boiling points than their oxide shells. These particles can burn in the vapor phase. Aluminum is examined in this thesis and is the focus from here forward.

Diffusion vs. Kinetic Regimes

For diffusion-controlled reaction of metal particles, the burning rate, G_f , is defined as:¹⁰

$$G_f = \frac{\dot{m}}{4\pi r_s^2} = \rho_s \frac{dr_s}{dt} = \frac{\rho D}{r_s} \ln(1 + im_{\infty}), \quad (5)$$

where ρ is the density of the particle, D is the diffusion coefficient, r_s is the radius of the particle, m_{∞} fraction of oxidizer in the free stream, far from the particle, and i is the mass stoichiometry index. Simplifying Equation 5 to a burn time, $t_{b,diff}$:

$$t_{b,diff} = \frac{\rho_s d_0^2}{8\rho D \ln(1 + im_{\infty})}, \quad (6)$$

where d_0 is the original particle diameter. Changes to the diffusion of the oxidizer and the overall stoichiometry of the system are major contributors in the diffusion regime. The time has an approximate d^2 relation for the particle diameter, where d is the diameter of a particle. Further empirical research summarized in the next section has been conducted to determine the exact exponent for aluminum.

The kinetic regime burning rate can be found by:¹⁰

$$G_f = \frac{\dot{m}}{4\pi r_s^2} = \rho_s \frac{dr_s}{dt} = \rho_s m_{\infty} k_s = i\rho m_{\infty} k_s, \quad (7)$$

where k_s is the heterogeneous specific reaction rate. The burning time of the particle can be found by:

$$t_{b,kin} = \frac{\rho_s d_0}{2i\rho m_{\infty} k_s}. \quad (8)$$

It can be seen that, in the kinetic regime, the burning time is proportional to d .¹

To determine whether or not the system is diffusion or kinetically dominated, the

Damkohler number can be calculated:¹⁰

$$Da = \frac{t_{b,diff}}{t_{b,kin}} = \frac{d_0 i m_{\infty} k_s}{4D \ln(1 + im_{\infty})}. \quad (9)$$

For Damkohler numbers larger than 1, diffusion is dominant. If the value is lower than 1, then the system is kinetically controlled.

Particle Size Trends

It was found that there would be a strong dependence on particle size since smaller particles have large surface areas compared to their volumes. In the 1960s, aluminum was applied to solid rocket motors and was found to rid the motor of instabilities, as shown by Summerfield.¹¹ Specifically, it was found that the mass of the aluminum particles dampened out different acoustic frequencies based on particle size. Over the next decade, research continued on aluminum particle combustion, in particular, with measurements of burning times based on diameter and examination of the effect of pressure. Friedman and Mahek^{12,13} showed that ignition of single aluminum particles occurred around 2300 K, which is close to the melting point of Al_2O_3 .

Bazyn et al.¹⁴ provided a diagram of the different structures for diffusion, kinetic, and transition burning regimes. Transition of regimes occurs approximately at the surface of the particle or slightly farther out. The shrinking-core or kinetically controlled burning occurs when oxidizer moves inward to the particle and the reaction area shrinks with time. The temperature appearance relative to the Al_2O_3 boiling point is also shown. Diffusion raises the temperature above the Al boiling point and reaches the Al_2O_3 boiling point. For transitional and shrinking core burning, the temperature does not reach the Al_2O_3 boiling point.¹⁴

Flame Structure of Aluminum

Bucher et al.¹⁵ explored the distribution of AlO and Al_2O_3 around a burning aluminum particle. A luminosity region surrounds the individual burning particles. Butcher shows that the burning temperature peaks at two radii from the center of the particle. The concentration of Al_2O_3 does not peak until after a peak in temperature, around 2.5 to 3 radii away. The radical AlO ,

which is important in the chemistry of combustion, peaks earlier than Al_2O_3 . AlO is in high concentration around 1.5 to 2.5 radii away. This makes sense since the radical will be present in the reaction front between fuel and product.

Yetter and Dryer¹⁶ showed both the pressure effect and oxidizer effect on the burning structure of an aluminum particle, seen in Figure 2-1. In air at elevated pressures, aluminum particles were shown to have a much smaller luminous zone than at lower pressures. Since micron particles are diffusion controlled, the increase in pressure increases diffusion that results in a smaller luminous region.

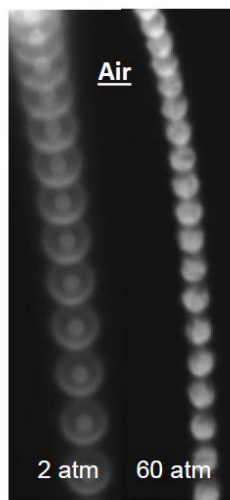


Figure 2-1. Aluminum-air Luminous Region at 2 and 60 atmospheres. A flame front that forms between the air oxidizer and vaporized aluminum is controlled by diffusion. Pressure and diffusion are proportional to each other, which means that as pressure increases, the luminous region decreases due to quicker diffusion. The flame approaches the surface of the particle as pressure is increased, which can be seen in the 60 atmosphere case.¹⁶

The oxidizer plays a critical role in the flame zone geometry. In air, the flame region is very spherical and well defined when burning under low Reynold's number and gravity conditions. As seen in Figure 2-2, in H_2O , the flame region is not symmetric and much smaller. The major reason for this change is that the reaction temperature of steam and aluminum is not as exothermic as that with air. Reaction 1, which shows the aluminum-air reaction has a standard

enthalpy of reaction of -3351 kJ/mol. Reaction 2, which is the aluminum-steam reaction has a lower enthalpy of reaction of -950 kJ/mol. Consequently, the flame temperature of aluminum-steam is lower than aluminum-air and closer to the vaporization temperature of aluminum. Therefore, the flame is close to the surface of the particle and the product aluminum oxide forms on the surface.

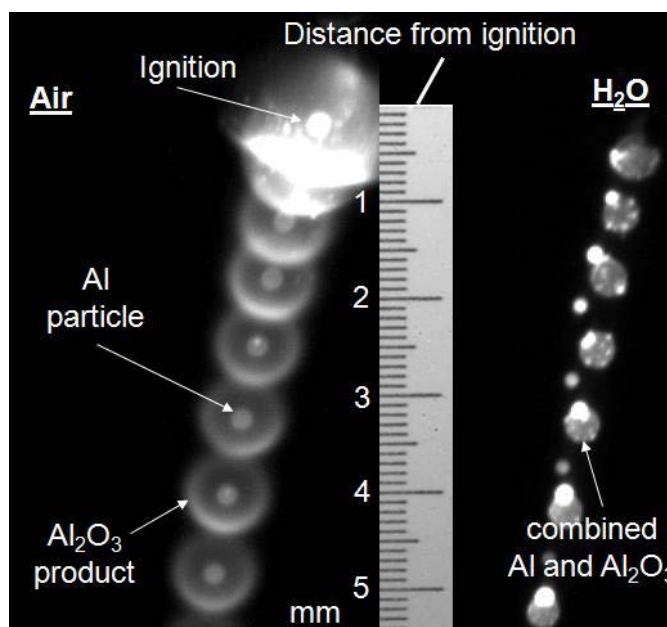


Figure 2-2. Comparing Flame Structure for Air and Steam. Aluminum-air flames for a luminous constant “halo” whereas aluminum-steam burn in more of a droplet shape is low Reynold’s number and low gravity conditions. The two main reasons for the difference in burn structure are that aluminum-air has a high standard enthalpy of reaction compared to aluminum-steam. The flame temperature of aluminum-steam is also lower and closer to the limit for vaporization of aluminum oxide. Therefore, the particle burns much closer to the surface, resulting in droplet shaped features.¹⁶

Choice of Experimentation

Due to the relationship to the works in this thesis, experiments that use a “dust cloud” fuel loading will be summarized. Goroshin¹⁷ looked at quenching distances, the minimum distance between flat plates where a flame cannot propagate, in aluminum dust clouds for laminar, turbulent, and oscillating flames. The quenching distance can be used to estimate the

laminar flame thickness, which is an important factor for combustion. Large plateaus were found for a range of fuel range mixtures for which the flame speed was approximately 20 cm/s for 21% oxygen concentration. Goroshin¹⁸ also ran other experiments in a Bunsen burner–type system to achieve burning velocities. The burning velocity was found to be largely proportional to the oxygen content and the carrier gas. Values ranged from 12 to 32 cm/s with increasing oxygen content and from 20 to 65 cm/s when switching carrier gases from argon to helium. Shoshin and Dreizin¹⁹ developed a lifted-flame aerosol burner to verify laminar flame speed. That work provides a reference for the flow conditions needed for a lifted flame. Additionally, that work verified a decrease in flame speed with higher particle concentrations. Work by Risha²⁰ explored the addition of hydrogen to improve thermal heat transfer and the addition of a percentage of nanoparticles. Hydrogen addition increased the flame speed since it has a much higher thermal conductivity than air. Nanoparticles also increased the flame speed; however, it also decreased the thickness and luminosity of the flame. Micron-sized particles burn longer and brighter than nanoparticles due to there being a large amount of aluminum compared to oxide shell.

Many experiments have been performed through the years, and are too numerous to discuss them all here. One of the main issues with aluminum research is there is no consistent experimental design, so multiple parameters vary from one experiment to another. An example of this is that some experiments use only single particles, whereas others use fairly dense particle loading. The result of heat transfer will affect the burning time of each test. Therefore, the important trends that were compiled by Beckstead²¹ are discussed below.

Theoretically, a burning time proportional to d^2 is found for spheres; however, the particle is not a complete sphere with respect to burning. The oxide cap reduces some of the area available. It is predicted that a $d^{1.8}$ value is more appropriate.²¹

Diffusion of oxidizer and fuel is a key process in aluminum combustion. Therefore, it makes sense that the burning time is proportional to the oxygen concentration.²¹ The choice of

diluent also affects the burning time. Diatomic molecules like nitrogen slow the burn time down more than gases like argon or helium due to their ability to store energy in the vibrational mode. If more energy is in the gas, less is going to heating up the particle for reaction.

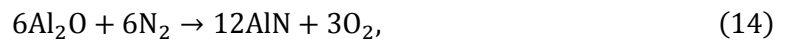
Aluminum typically has three common oxidizers: oxygen (air), H₂O, and CO₂. It has been proposed that oxygen is the best oxidizer followed by H₂O and then CO₂. Most experimentation has been done with oxygen, with fewer focusing on H₂O or CO₂. Huang et al.²² performed research based on differing oxidizer environments. They found that theoretically, that the aluminum–steam flame speed should be slightly larger than that of aluminum–air. Diffusion of the oxidizer and the addition of the H radical were hypothesized to contribute to the speed change.

Aluminum–Air Mechanism

As aluminum combusts with air, the chemical reactions can be separated into low temperature and high temperature reactions. At the beginning of combustion, the temperature is still low and the following reactions dominate:



Once the particles reach around 2800 K, the following reactions tend to dominate:



Aluminum–Steam Mechanism

It is important to try and understand the basics of the aluminum–steam combustion mechanism. It was proposed by Washburn²³ that the reaction could take two different forms:



In the past, it was believed that the first reaction rate was much smaller than the second. Further research has proved that the first reaction actually dominates and the second is not an elementary path. This is important in understanding the intermediate reactions.

Plasmas

Plasma is a state of matter composed of ionized gases, which are electrically charged, and create electric and magnetic fields. For low pressure plasmas, these fields are much stronger than the simple molecular collisions that occur at standard atmospheric conditions. For atmospheric plasmas, these fields are only stronger over a small distance. There are three parameters that must be met to be classified as a plasma:²⁴

$$\lambda_D \ll L, \quad (19)$$

$$N_D \gg 1, \text{ and} \quad (20)$$

$$\omega\tau > 1. \quad (21)$$

The Debye length, λ_D , must be much smaller than the length scale, L , of the plasma, the number of particles in the Debye sphere is much greater than one, and the plasma oscillation frequency, ω , times the time between collisions with neutral molecules, τ , is greater than unity.

The Debye length is the distance at which the electrical field drops to $1/e$ of its original value, where $e = 2.718$. The Debye length is found by:

$$\lambda_D = \sqrt{\frac{\epsilon_0 K T_e}{n_e q_e^2}}. \quad (22)$$

The Debye sphere is a control volume for which the radius of the sphere is the Debye length. The number of charged particles in this sphere must be much greater than one. This makes sense as anything less would be trivial.

The plasma oscillation frequency and the mean time between electron collisions with neutral atoms help determine between a plasma and inert gas.²⁴

The electromagnetic fields are significantly stronger than molecular collisions over a large range at lower pressure conditions. At atmospheric pressure, the fields are stronger over a short range.

There are various methods for producing a plasma. A DC discharge is used to create a plasma in a closed container that includes two electrodes.⁴⁶ A plasma forms as ion travel from along the created electromagnetic field to the cathode surface. As current increases and thus the electromagnetic field, a glow discharge will begin to form. If the current is increased even further, an arc plasma can form. Typically arc plasmas are used in industrial setting to cut metal. Sometimes DC discharges are pulsed to allow the power to increase and to have the ability to control the conditions better with the duty cycle. Microwave discharges are also used to create plasma. The microwave plasma discharge is formed using resonant cavities. Waveguide and coaxial cables are used to direct the microwaves and can be adjusted to maximize coupling. An inert gas then flows through the region of peak electrical coupling. If the electromagnetic field is large enough to overcome the breakdown voltage, a plasma will form.⁴⁶

Plasma-Assisted Combustion

Various plasma-based ignition and combustion studies have been performed in the past several years. Mainly, plasmas have been considered for igniting a wide range of fuel-to-air ratios and igniting supersonic fuel flows.

Laser-based spark ignition originally examined the effect of pressure on combustion gases.²⁵ Two laser wavelengths, 532 nm and 1064 nm, were used to determine the breakdown threshold.

Wang et al.²⁶ looked at transient plasma ignitions of fuels for an internal combustion engine application. It has been proposed that, as an alternative to a thermal spark, a plasma discharge could be used to create radicals for ignition. The plasma helped reduce ignition delays for hydrocarbon mixtures. Plasmas may be able to reduce the ignition time of aluminum particles as well.

The effect of plasmas on stabilizing low velocity flames has also been studied. Pulsed nanosecond plasma discharges were used to determine the effect on a premixed propane–air system.²⁸ The plasma significantly increased the velocity needed to blow-off, which allows a burner to operate over a wider range of volumetric flows for the same geometry. The blow-off velocity will limit the amount of energy that can be achieved from a particular burner, and with higher flows, more energy can be extracted. This phenomenon was most noticeable as the equivalence ratio approached 1. There was little effect around the lean limit equivalence ratio of 0.4. The plasma had a noticeable effect on the OH radical in the system. Both the intensity and location of the radicals shifted with the pulsed plasma. Without the plasma, the distribution of OH radicals is Gaussian. With the plasma, the intensity shifts closer to the base of the flame. This helps reactions to occur in a shorter amount of time to prevent blow-off.

Effect of Plasma on H₂–O₂ Mechanism

The enthalpy of combustion for hydrogen is 286 kJ/mol. Typically, the mechanism of a simple hydrogen–oxygen system looks like:



With the addition of a plasma discharge, the following dissociations could replace the chain initiation reaction:



The rate constant of these two reactions at normal conditions, without the electron, is $10^{-11} \text{ cm}^3/\text{s}$. The electron present in Equation 29 and 30 increases the rate constant to $10^{-9} \text{ cm}^3/\text{s}$. This suggests that the plasma discharge initiation is more efficient than one by a conventional thermal spark.²⁷

Microwave Torch

Plasma torches to achieve atmospheric thermal equilibrium discharges were designed using induction in 1960 by Reed.²⁹ Magnetrons that produce microwaves were later found to create plasmas that have different properties than other power sources. Musil³⁰ summarized the various designs that can be used to produce microwave plasmas. The waveguide discharge has been expanded on and detailed by Moisan et al.³¹ and Uhm et al.³² and shown to have application similar to the needs in this thesis. In all the papers mentioned, there is a tube that runs through the

waveguide carrying the intended plasma gas. Various seals and adjustable parts to increase coupling are detailed.

Moisan et al. proposed an axial gas injection similar to the device used in this work. Microwave power is provided to the torch through the use of a waveguide. Two separate adjustable tuners are used to change the electromagnetic coupling: a plunger on the waveguide and a tunable coaxial section. The two tuners can be adjusted to optimize the energy transferred to the plasma gas. In addition to Moisan et al.'s design, this work uses a coaxial design, which allows for a flow outside of the inner plasma tubing. Holes were drilled in the adjustable tuner to allow gases to pass through.

For this thesis, the two adjustable tuners are the plunger on the end of the waveguide that moves the reflecting surface and the spacer shown in the annulus of the coaxial injector. A waveguide is an object that allows electromagnetic waves, like microwaves, to travel without loss or expansion. The spacer contains holes or allowing fluids to pass, similar to Moisan's design. The burner attached to the waveguide and spacer location are shown in Figure 2-3.

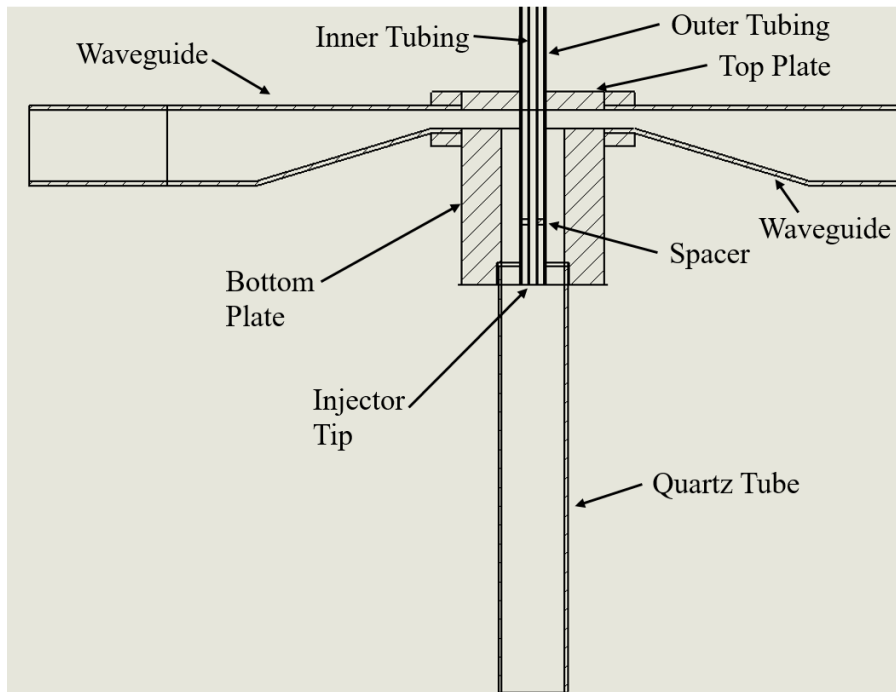


Figure 2-3. Diagram of a Burner Attached to a Waveguide and Containing a Spacer for Adjusting Microwave Coupling. The burner consists on a coaxial injector that is attached to a waveguide to couple microwave power. The coaxial injector is made up of an inner tube and outer tube that are used to carry gas for a plasma, fuel and oxidizer. The top plate and bottom plate attach the injector to the waveguide and form a seal securing the electromagnetic radiation. The waveguide allows for directing electromagnetic radiation from where it is generated to the injector. A spacer is used as one of the adjustable tuners that can be moved to optimize coupling, and in this case for a resonating cavity.

ANSYS High Frequency Structure Simulator (HFSS) simulates electromagnetic fields, including microwaves, applied to various geometries. Figure 2-4 is a simulation performed by Palomino showing the E Field and a specific combination of plunger and spacer locations. Iterations were performed to optimize the potential E Field, and thus the coupling.

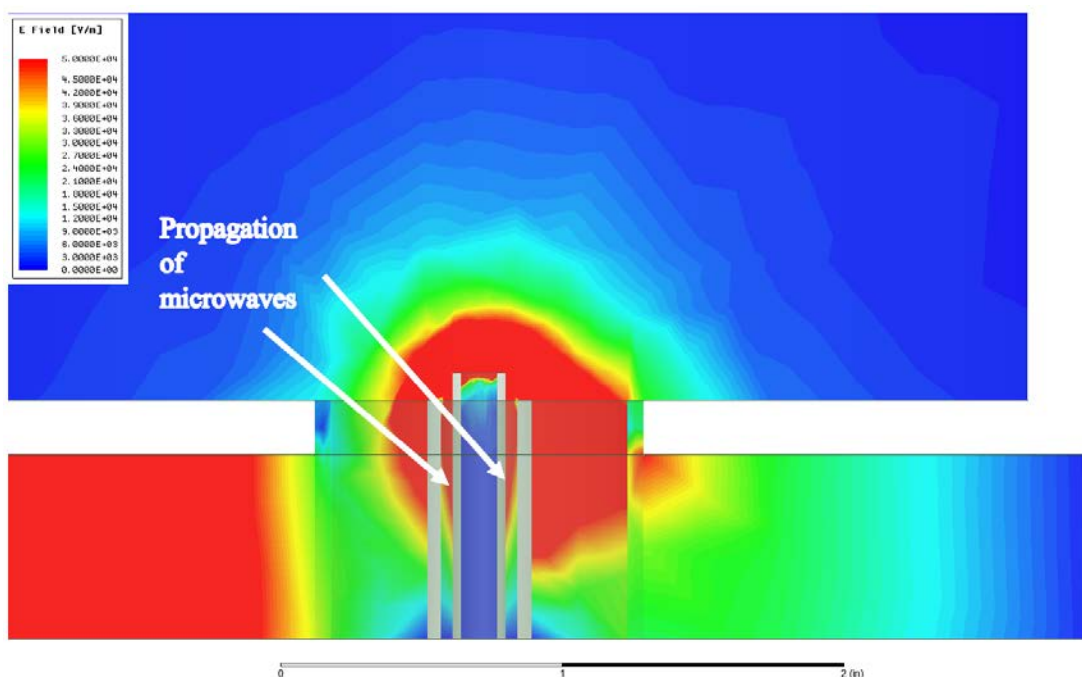


Figure 2-4. ANSYS HFSS Simulation of a Coaxial Injector Performed by Palomino.⁴¹ Ansys HFSS models electromagnetic fields and is used to determine the strength of the electric field created on a specific geometry. The software could not determine if a plasma itself would form, however it is helpful in determining optimized coupling positions of the spacer and the tuner on the waveguide.

Forward power is the amount of power that reaches and is coupled into the burner.

Reflected power is the measured value that is sent back through the waveguide which is not used.

Typically it is desired to maximize forward power and minimize reflected power. The higher the power that reaches the burner results in a larger electric field produced. Therefore, more power input to the magnetron results in more microwaves and a larger electric field. Each gas has a specified breakdown voltage. Once that value is exceeded, a plasma will form.

Spectroscopy

Optical emission spectroscopy is an important method for interpreting temperature and excited species in plasma experiments. Plasma and combustion are two sources of light emissions

in this experiment. Optical emission spectroscopy can be used to determine what excited species are present due to photon emissions. A spectrometer is a device used to measure the intensities of these emissions with respect to wavelength. The light from the source is passed through a grating, which diffracts the light. After some mirrors to adjust the positioning, the light reaches a detector that measures the intensity at each wavelength. It is important to see the intensity at different wavelengths to identify different excited species, since each excited species emit specific wavelengths. The intensity of various emissions increase with a change in temperature. A plasma temperature can be found by using temperature fitting software to fit certain species, like nitrogen. Additionally, thermally hot objects give off a broadband emission that can be fit using Planck's Law to determine a temperature.

Argon

Cullen and Milosavljević³³ characterized an argon plasma in ambient air, thus oxygen and nitrogen were introduced with the argon. A KinPenMD™ was used to generate the argon plasma. Volumetric flow rates were similar to those used in this experiment, 1.3–5 SLM. The power was significantly lower at 8 W. The spectra recorded in Table 2-1 was obtained. Various electron transitions occur for argon around 700–900 nm. Nitrogen shows about four distinct peaks between 300–400 nm. This can cause some overlap with the OH radical, which can introduce ambiguity to fitting results.

Table 2-1. Argon, Oxygen and Nitrogen Optical Emission Wavelength Used for Spectroscopy³⁴

Species	Wavelength (nm)
Ar I	696.543
Ar I	706.722
Ar I	714.704
Ar I	727.294
Ar I	738.398
Ar I	750.387
Ar I	763.511
Ar I	772.376
Ar I	794.818
Ar I	800.616
Ar I	811.531
Ar I	826.452
Ar I	840.821
Ar I	842.465
Ar I	852.144
O I	777.2
N2 (2+)	300-410
N2 (1-)	400-430

Steam

Ni et al.³⁵ used a DC-plasma water torch to create a steam plasma, which is different than a microwave plasma torch. An arc is created to both generate steam from liquid water and plasma discharge through a nozzle. Ni's experiment consisted of an arc plasma instead of a microwave torch and liquid water was directed to the plasma instead of creating steam first, which was done in this thesis. The spectroscopic results are still valid for identifying species despite the experimental differences. Two of the major radicals, OH and H were observed. The OH radical's emission is between 306–310 nm, shown in Figure 2-5. The major radical seen in hydrogen is H_α, which occurs at 656.28 nm.

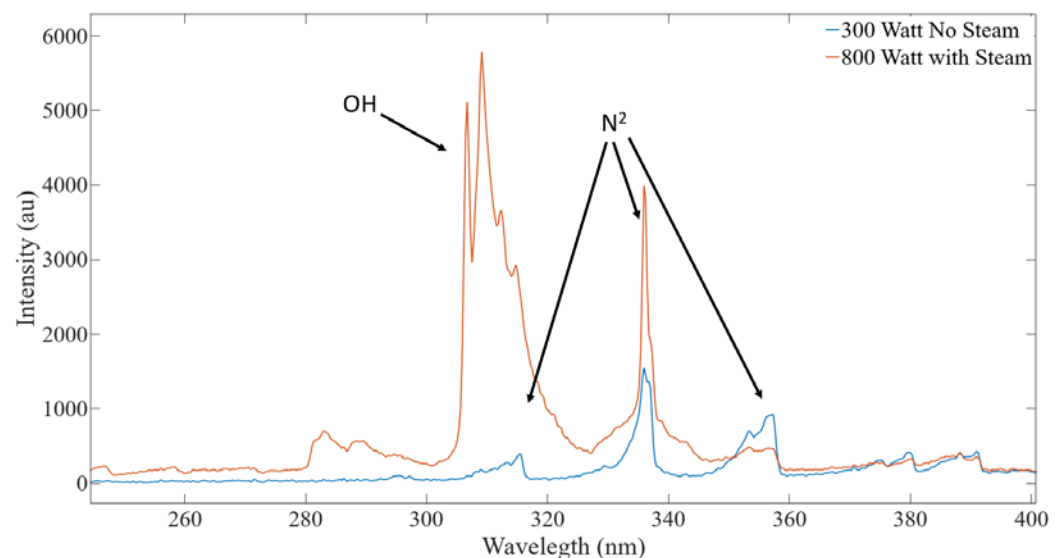


Figure 2-5. OH Radical Present From Steam Introduction to a Plasma. Data from two plasma was captured and compared, a 300 W argon plasma (blue) and an 800 W argon plasma with steam entrained (orange). OH radicals are much stronger intensity in the case with steam entrained. Potentially, some water vapor could have been introduced from impurities in the industrial gas, indicating small OH emissions in blue. The steam itself is interacting with the plasma and creating radicals. These radicals are important in continuing reactions after combustion has begun.

Aluminum and Aluminum Oxide

Spectroscopy has been used during aluminum combustion to identify some basic species. The problem with spectroscopy during combustion is that the thermal radiation quickly saturates most of the visible wavelengths. Goroshin et al.³⁶ used a Bunsen burner to ignite premixed aluminum–air mixtures. A laminar flame was achieved and scanned radially across the flame. The aluminum–air spectra was captured and clearly shows Al and AlO lines. In this thesis, the flame achieved was turbulent and not premixed. However, the same Al and AlO emission were seen.

Al appears with two sharp peaks at 394.4 and 396.2 nm. Presence of these two lines proves that there is vaporized aluminum oxide during an experiment. The AlO lines appear over

five wide peaks from 450–550 nm, which are also important in understanding the vaporization of the oxide shell. This also suggests that the oxide shell was broken so reaction with the internal aluminum would begin.

Temperature Fitting

Goroshin et al.³⁶ detail the derivation of temperature fitting of the condensed species to a broad optical emission (550–900 nm). Planck's Law relates emitted wavelengths and their intensity to temperature,

$$\ln \left(\frac{i_{\lambda,T} \times \lambda^5}{\varepsilon(\lambda, T) \times 2\pi \times C_1} \right) = \frac{C_2}{\lambda T}, \quad (31)$$

where $i_{\lambda,T}$ is the intensity, λ is the wavelength, and $\varepsilon(\lambda, T)$ is the emissivity. The constants are defined by:

$$C_1 = h \times c_0^2 = 6.626 \times 10^{-34} \times (3 \times 10^8)^2 = 5.9634 \times 10^{-17} \frac{\text{W}}{\text{m}^2} \text{ and} \quad (32)$$

$$C_2 = \frac{h \times c_0}{k} = \frac{6.626 \times 10^{-34} \times 3 \times 10^8}{1.38 \times 10^{-23}} = 1.44 \times 10^{-2} \text{ m} \cdot \text{K} \quad (33)$$

The gray-body assumption states that the emissivity is not dependent on wavelength. Therefore, the left hand side of the equation is constant and $1/\lambda$ is proportional to $1/T$. From the experimental data that Goroshin collected, it was seen that the data did not accurately fit the $1/\lambda$ assumed by the gray body. Wolfhard³⁷ suggest that the emissivity of the aluminum oxide, which dominates the emission, would follow closer to a $1/\lambda^2$ relationship. Goroshin's experimental data agree with this approximation. When substituting the $1/\lambda^2$ relationship for emissivity, Planck's Law becomes:

$$\ln(i_{\lambda,T} \times \lambda^7 \times 2\pi \times C_1) = \frac{C_2}{\lambda T}. \quad (34)$$

Further work by Kalman et al. examined aluminum oxide spectroscopy and determined that emissivity scales by $\lambda^{-1.4}$ from 2800–3500 K for micron-sized aluminum.³⁸ In another work, Kalman et al. investigate the effect of optical depth on aluminum oxide emissivity. The work suggests that $\lambda^{-1.4}$ relation for micron-sized aluminum is only valid for optically thin flames. For this experiment, the flame region would be at most 0.5–1.0 inch wide, which would still be in the optically thin region. Therefore, Planck's Law simplifies to:

$$\ln(i_{\lambda,T} \times \lambda^{6.4} \times 2\pi \times C_1) = \frac{C_2}{\lambda T}. \quad (35)$$

Aluminum Particle Burning Temperature

Ermakov et al.³⁹ investigated aluminum particle burning temperatures using an embedded thermocouple. A laser was used to heat the particles while observing the change in the thermocouple reading. Ignition of the particles was seen to occur around 2025 K. During combustion, the particles rose to 2430–2540 K depending on the amount of power input. The particles tested by Ermakov were significantly larger than those used in this work. Even with a size difference, the temperature should be relatively similar considering that the amount of energy density is equal. Knowing at what temperature the particles burn can allow for comparison between the temperature fittings to determine if the particles are actually combusting, or just getting hot.

Past Work on Plasma-Assisted Combustion

Work directly on the same topic as this thesis has been performed by two groups. Lee investigated a high temperature steam plasma torch for igniting aluminum powder.⁴⁰ Palomino investigated an argon–helium plasma torch for igniting aluminum.⁴¹

Lee et al. initially performed research on energetic metal particles passed through a thermal argon plasma. In the experiment, micron-sized aluminum particles flowed through a plasma without oxidizer. The exiting products were collected on a cold plate and examined. The results were a layer of smaller aluminum particles. It was predicted that the particles were vaporized and then reformed. With these results, it can be said that a thermal plasma provided enough energy to vaporize the aluminum oxide shell. It was proposed that in further experimentation, the inner aluminum can be exposed to an oxidizer and thus initiate combustion with a plasma.

Lee also performed experiments with a steam plasma torch. The torch was a DC igniter, which formed a plasma between the cathode and anode of the igniter. Liquid water was fed into the igniter tip, which had an initial startup time to achieve gaseous steam. The plasma jet reached ≈ 5000 K near the tip of the igniter. For application to aluminum combustion, the jet needed to reach a temperature higher than the aluminum oxide shell's melting point of ≈ 2300 K and also contain radicals to continue the reaction. Aluminum combustion was verified through spectral graphing of the AlO emission, x-ray diffraction (XRD), and energy-dispersive x-ray spectroscopy (EDS). The delivered power to the plasma was proportional to both the pressure and the amount of water mass flow. The concentration of OH radicals was measured using an intensified charge-coupled device (ICCD) camera. An increase in current to the igniter resulted in an increased in OH radicals.

Palomino performed research to develop a proof-of-concept microwave aluminum igniter. The design involved a 2.45-GHz magnetron and waveguide-based burner configuration. The setup (Figure 2-6) involved aluminum being carried with an argon carrier gas and mixing with the gas used to form a plasma prior to reaching the waveguide and finally the plasma. The plasma gases used were argon and helium. Steam was injected in the side of the quartz chimney used as the burner.

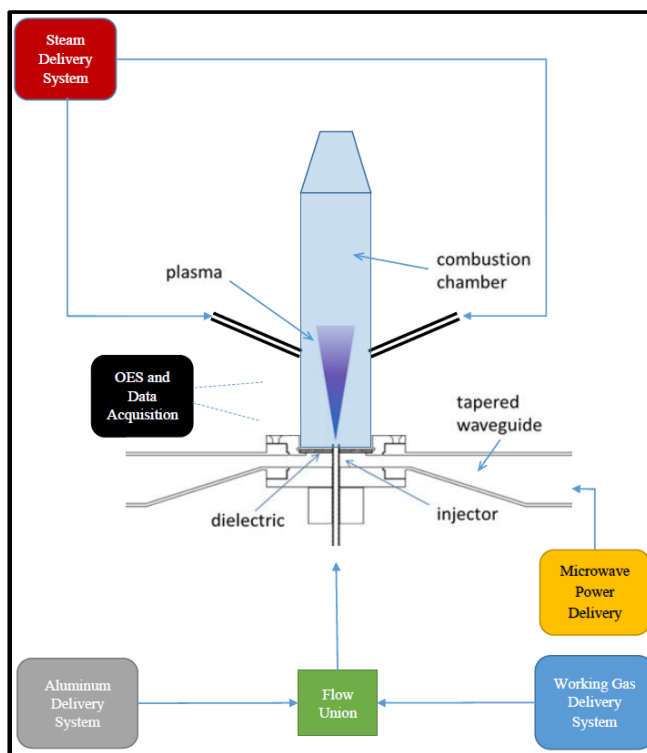


Figure 2-6. Palomino's Plasma Torch Configuration.⁴¹ Palomino used a non-premixed plasma igniter. The injector was attached to the waveguide for microwave coupling. The injector formed a plasma through which aluminum particles were fed from a particle feeder. There were two ports on the side of the combustion chamber for a steam inlet. Data acquisition was able to capture data through the combustion chamber, which was made from quartz.

Both the argon and helium plasmas that were used for combustion were characterized using spectroscopy. Temperature fittings were performed, and steam was introduced to the plasma. Dissociation of the steam was observed.

Coaxial Fluid Flows

Coaxial injectors are commonly used in combustion applications for delivering fuel and oxidizer of non-premixed systems due to the locality of both flows and the increased mixing at the interface. An advantage of the non-premixed burners is that the fuel and oxidizer cannot react upstream of the injector tip. Non-premixed configurations rely on mixing to burn, so velocity mismatches are used in the annular and core flows due to the formation of vortices that increase mixing. The fluid dynamics of the interface between the two fluids and the eddies that are created were examined and modeled. Equations used were mass continuity, conservation of momentum, and scalar transport:

$$\rho_{,t} + (\rho u_j)_{,j} = 0, \quad (36)$$

$$(\rho u_i)_{,t} + (\rho u_i u_j)_{,j} = -p_{,i} + (2\mu S_{ij})_{,j} + t_{ij,j}, \text{ and} \quad (37)$$

$$S_{ij} = \frac{1}{2}(u_{i,j} + u_{j,i}) - \frac{1}{3}\delta_{ij}u_{k,k}. \quad (38)$$

where ρ is the density of the fluid, u is the velocity of the fluid, p is pressure, S_{ij} is the stress tensor, t is time, and δ_{ij} is the Kronecker Delta function.

Dahm et al.⁴² ran experimental testing of a coaxial jet and varied both the velocity ratio of the outer-to-inner flow and the magnitude of the flows. At the exit of the injector, the boundary of both flows creates a shear region resulting in vorticity and thus mixing. u_2 is defined as the velocity of the outer annular flow and u_1 is the velocity of the core flow.

In the $u_2/u_1 = 0.71$ case, axisymmetric vortices form in the outer flow. When $u_2/u_1 = 1$, wakes form, but are dominated by the outer flow. $u_2/u_1 = 2.56$ shows a shift as the inner flow starts to develop well defined vortices. Dahm et al.⁴² displayed that coaxial injectors cannot simply be modeled by two separate jets. The boundary between the two flows is complicated and significantly changes with speed. This must be taken into account when a

diffusion flame is present, as is the case with aluminum combustion. The rate of mixing, and thus the ratio of these two flows, is a large part of the time scale needed for the particles to burn.

Pierce and Moin⁴³ investigated coaxial jets for combustion by including heat release. They used LES (Large Eddy Simulation) to model the flows and thermal reaction of the coaxial jet. It can be seen that swirling significantly affects the area one-to-two diameters downstream of the jet. More mixing occurs and a wider flame/stream develops due to the radial component added.

Chapter 3

Equipment List

Various equipment was used to achieve a plasma, deliver appropriate gases and aluminum particles to the burner and data acquisition tools. Figure 3-1 provides an overview of the major components in the experiment that are covered in Chapter 3.

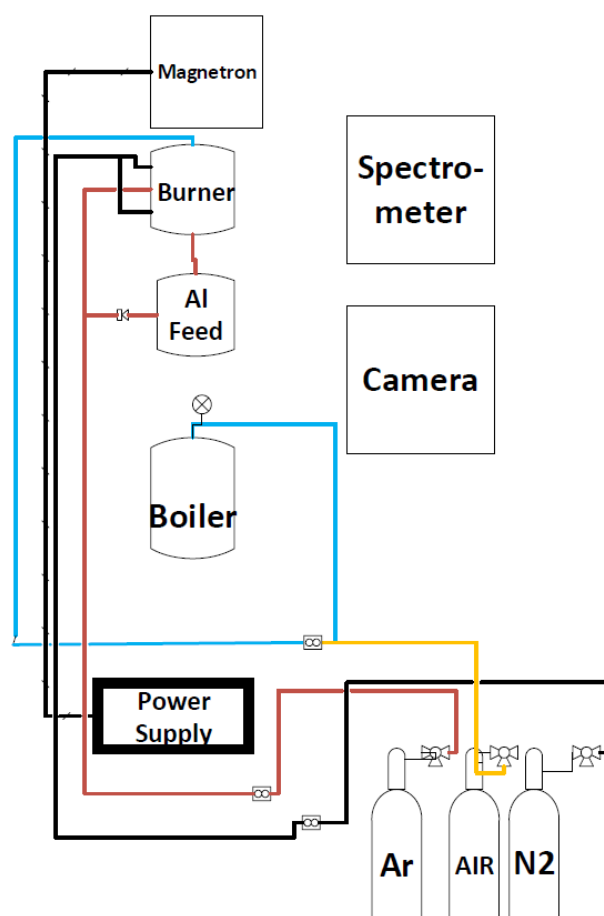


Figure 3-1. Overall Schematic of Major Experimental Components. The high voltage power supply powered the magnetron, which was used to produce microwaves, which was connected to the burner through a waveguide. Argon, air and nitrogen were sourced from industrial bottles and metered with mass flow controller. Each gas traveled to the burner through tubing. If steam is used for the oxidizer, a boiler is used to generate saturated steam. The steam then is flowed through a mass flow controller and through a heated section of tubing. The aluminum feeder uses argon gas to match that used to create the plasma, and travels to the burner. Various data acquisition like a spectrometer and high speed camera are used to capture data from the burner.

Microwave Generation

The following components are part of the experimental setup that was used to provide a microwave power source at 2.45 GHz to create a plasma.

A SGP-15AC DC high-voltage module, seen in Figure 3-2, directly powers the magnetron with between 100–1500 W of power. Accuracy and controllability are reduced below 100 W. The supply has feedback controls connected to the magnetron and can measure the forward and reflected power. The power supply uses 200 V and <15 A. On the front panel of the power supply are indicators of various alarms, power output, and a manual control knob. The remote pinout on the back of the supply (Table 3-1) was configured to perform in external mode through the use of LabVIEW, making adjustments to the power possible from the safety of outside the test cell.



Figure 3-2. SGP-15AC DC High-Voltage Module Used to Provide Power to the Daihen SGM-15A Magnetron. The high-voltage supply was the source for powering the microwave generation. Various interlocks are designed into the system to prevent misuses. The high-voltage supply control is integrated into a LabVIEW program that uses an analog output voltage to control the power. The power output from this supply is proportional to the electric field created from the magnetron.

Table 3-1. Remote Pinout of SGP-15 AC DC High-Voltage Module. The pinouts were used to operate the high-voltage module remotely through a LabVIEW program. Specifically, the microwave ON/OFF, interlock and voltage input to meter the power.

Pin No.	Contents
1	Pf setting input (+side)
13	Pf seyying input (-side)
2	+5V~+24V input
14	+5V~+24V input
3	Microwave output ON/OFF signal input
15	RESET signal input
4	INTERLOCK signal input
16	NC
5	NC
17	NC
6	Microwave output ON state signal
18	NORMAL signal
7	Firament power supply ON state signal
19	NC
8	NC
20	NC
9	Open collector output emitter side
21	Open collector output emitter side
10	Pf monitor output (+side)
22	Pf monitor output (-side)
11	Pr monitor output (+side)
23	Pr monitor output (-side)
12	NC
24	NC

The Daihen SGM-15A magnetron is connected to the SGP-15AC DC voltage module by a power cable, a filament control cable, and an AC filament cable. The magnetron converts the input DC power from the high power supply and converts it into 2.45-GHz microwave power.

The Daihen CMC-10 tuner automatically changes the impedance between the load and source to minimize the reflected power to the magnetron. The tuner could be observed working by watching the reflected power during the plasma generation. As soon as the microwave power was turned, on the reflected power would be very low. When the plasma appeared, the impedance

would change and the reflected power would spike for approximately one second, then fall back to zero once the tuner adjusted.

Reducing waveguides were used to attach the burner to the magnetron. At the end of the waveguide, a tunable short was placed to adjust the position of the wavelength peaks.

Burner and Injector

The burner is the main experimental piece of equipment. It provides the area where all feeds (aluminum, oxidizer, argon, and microwave power) mix. Attached directly to the waveguide, the burner is configured to optimize electrical coupling between the components to achieve a plasma. A coaxial design is used for introducing the needed flows. A cross sectional view of the components in the burner is shown in Figure 3-3.

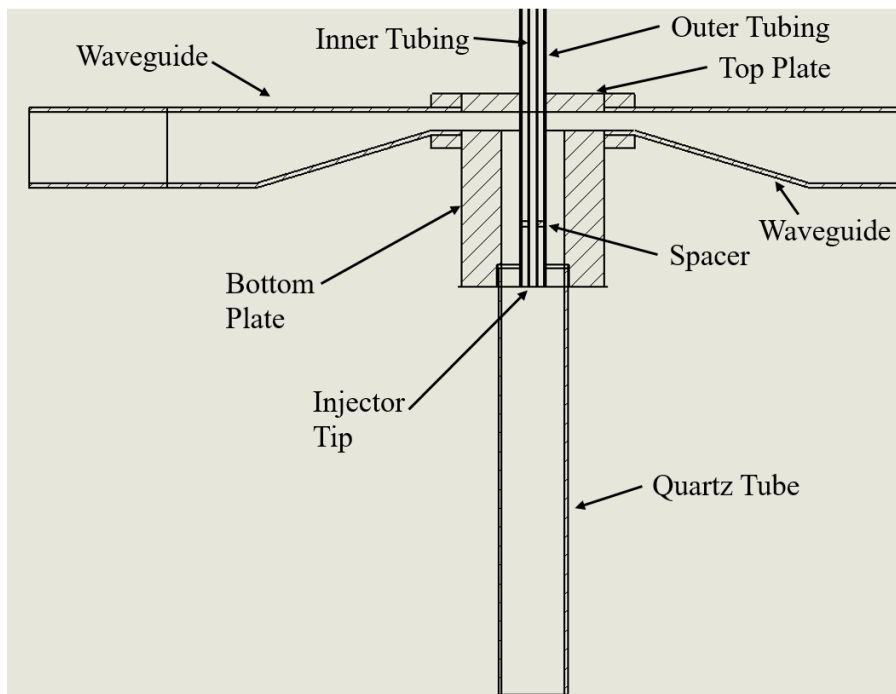


Figure 3-3. Major Components of Burner Attached to the Waveguide. The burner consists on a coaxial injector that is attached to a waveguide to couple microwave power. The coaxial injector is made up of an inner tube and outer tube that are used to carry gas for a plasma, fuel and oxidizer. The top plate and bottom plate attach the injector to the waveguide and form a seal securing the electromagnetic radiation. The waveguide allows for directing electromagnetic radiation from where it is generated to the injector. A spacer is used as one of the adjustable tuners that can be moved to optimize coupling, and in this case for a resonating cavity

In the final configuration (Figure 3-4), oxidizer enters and travels through the annulus of the design. The mixture of argon gas with entrained aluminum particles travels through the center tube.



Figure 3-4. Aluminum Burner Connected to the Waveguide. The actual burner configuration can be seen. Specifically, the side ports for the nitrogen purge flow can be seen on the bottom plate. Also, the supporter for the quartz tube can also be seen.

The top plate secures the burner to the top of the WR-284 waveguide applicator and creates a seal in the waveguide. Additionally, the clamp is bolted into the top plate to secure the tubing from sliding. The bottom plate serves as both a seal to the waveguide applicator and the upper resting region of the quartz tube. Swirl ports are machined into the side of the bottom plate.

The outer tubing is a $0.5'' \times 0.43'' \times 6''$ molybdenum tube. The outer tubing was designed to be the location of the maximum microwave coupling. This tubing also provided the path for the oxidizer to flow to the end of the burner. Molybdenum was chosen for its favorable thermal and electrical properties. The inner tubing is a $0.1875'' \times 0.1475'' \times 10''$ molybdenum tube. The

tubing is used to pass the mixed aluminum and argon mixture into the plasma region created at the end of the inner tubing. Both the ends of the inner and outer tubing are coplanar, which help in mixing and electrical conductivity. The top end of the inner tube connects to a tee mixing union, which combines the argon flow with aluminum.

During testing, both stainless steel and molybdenum were tested. Stainless steel was prone to damage caused by the argon plasma filaments. If the plasma became stagnant at any point, the tubing would begin to melt and thus be damaged. To prevent further damage, and to move towards a more robust system, molybdenum tubing was used. Molybdenum has higher thermal and electrical conductivities. Hot spots from the plasma are distributed throughout the tube more readily, as well as microwave coupling is improved with the use of molybdenum. No structural damage was seen on the molybdenum even after dozens of tests. The molybdenum inner tube and adapter unions are shown in Figure 3-5.



Figure 3-5. Inner Tubing with Upper Adapting Unions. The inner tube is attached to the Swagelok tee and is sealed using various fittings. This allows for fluid entering the annulus of the coaxial injector to be forced to flow down and not leak out the top of the tee.

The spacer is a piece of stainless steel that is press fit into the outer tubing (Figure 3-3). There is a hole for the inner tubing to pass through. In the spacer, there are several holes cut at a 10° angle to promote a slight swirl to the oxidizer in the annulus. This creates better mixing after

injection and promotes better oscillation of the plasma filament. Stagnant filaments damage the tube and are not favorable for combustion. The spacer also acts to promote the resonance of microwaves to the tip of the injector (Figure 3-6).

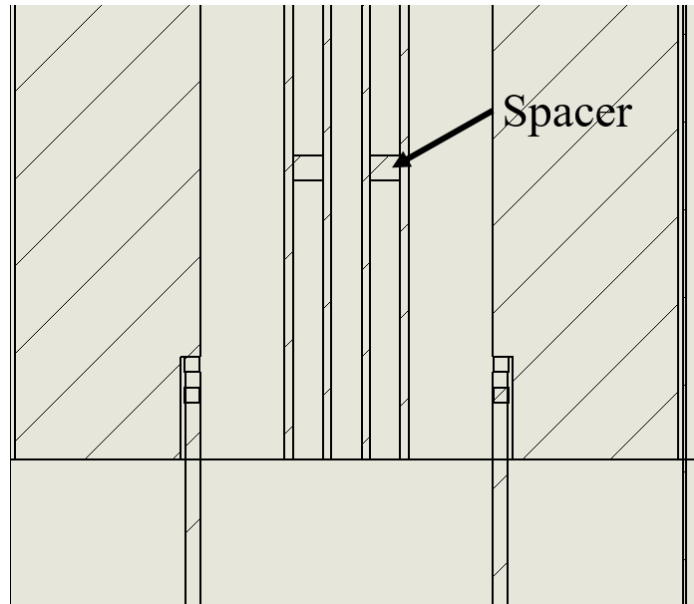


Figure 3-6. Location of Spacer and Resonant Cavity. The spacer is located in the annulus of the coaxial injector and provides a resonant cavity to amplify the microwave coupling. The depth of the spacer is critical in maximizing this coupling. Holes are placed in the spacer to allow fluids to pass through. Additionally, the holes are placed at 10° angle to add a swirl element to the fluid to increase mixing.

The clamp secures the outer tube of the coaxial system to the top plate. Two screws are used, one to tighten radially and one to connect vertically into the top plate. The clamp eases the alignment of the injector tip to the edge of the bottom plate, for maximum microwave coupling. The outer tubing, top plate and clamp are shown in Figure 3-7 and Figure 3-8.

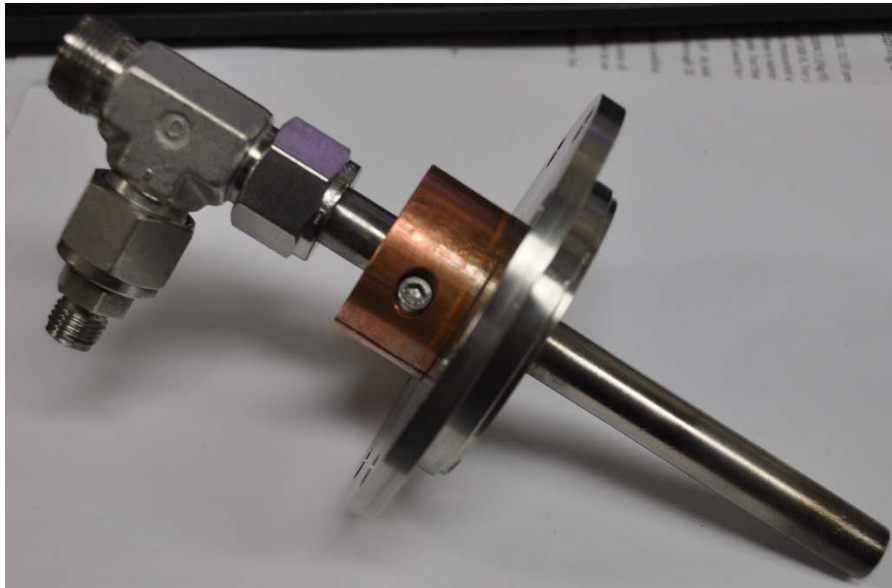


Figure 3-7. Outer Tubing, Top Plate, Clamp, and 0.5" Swagelok Tee. The Swagelok tee is important to introducing flow for the annulus region of the coaxial injector. The copper clamp shown secures the axial location of the injector to the top plate, which is secured to the waveguide. The axial distance is important to be in the correct location since it effects the coupling.

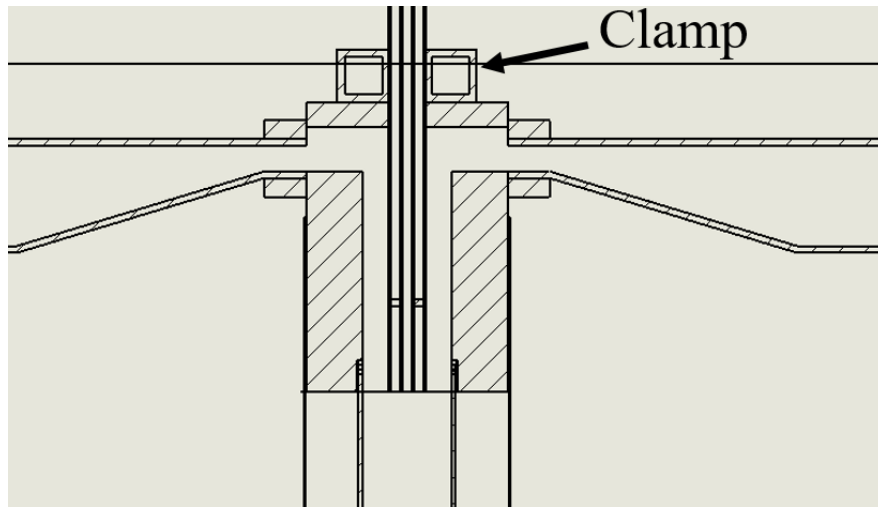


Figure 3-8. Section View of Outer Tubing, Top Plate, Clamp and Inner Tubing. The section view of the burner provides a view of the region of the bottom plate and how it connects to the waveguide. The clamp sits on the top plate and secures the injector axially.

The $1.5'' \times 10'' \times 0.25''$ cylindrical quartz tube provides a containment method to ensure that the system is purged of atmospheric air during an experiment and to provide a path for hot

product species to controllably follow. Quartz itself allows for optical data to be observed since it has relatively high transmission among relevant wavelengths. The quartz tube is supported by a collar connected by two pieces of all thread to the bottom plate. The collar uses a thin piece of aluminum oxide to allow for thermal expansion. The collar holds the bottom of the quartz in place, while nuts are used to secure the collar. There are various fittings toward the top of the injector. At the top of the outer tubing, a 0.5" Swagelok tee provides an inlet to the annulus region. The inner tubing passes through the entire tee and is fed through a reducer at the top creating a seal. On the side port, the oxidizer enters and can flow downward in the annulus. After the tee, the inner tubing was connected to a couple of unions to the mixing tee. The mixing tee union is where the argon plasma gas and aluminum powder are mixed before heading to the inner tubing. The mixing tee is shown in Figure 3-9.

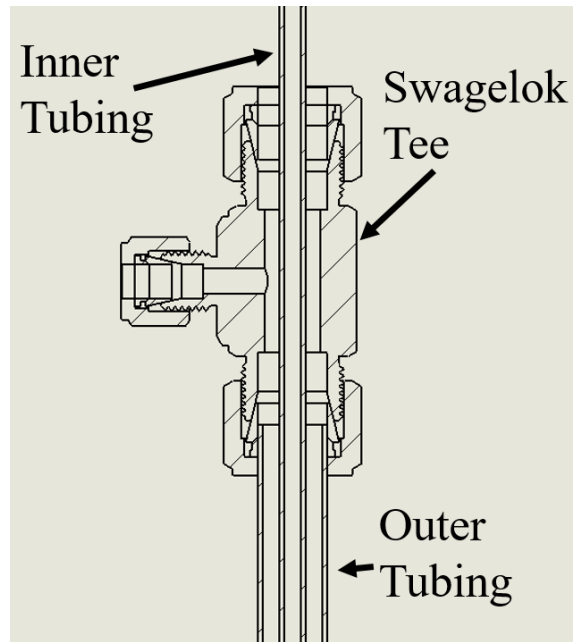


Figure 3-9. Section View of Mixing Tee and Inner and Outer Tubing. The mixing tee provides entry for the annular flow to enter between the outer tubing and the inner tubing. The inner tubing passes straight through and is securely fastened at the top to force the annular flow down the injector.

Fluid Flows

There are four main flows in system: the oxidizer flow, the argon plasma, the argon aluminum powder flow, and nitrogen swirl flow.

The oxidizer flows for this experiment were steam, air, and carbon dioxide. Steam was produced onsite, whereas air and carbon dioxide were sourced from industrial bottles.

Saturated steam is generated in the boiler at a set pressure. A mass flow controller then limits the rate of flow, which is then followed by heated sections of tubing traveling to the burner. The heated sections help limit heat losses. Once at the burner, the steam enters through the side port and can travel in the annulus of the coaxial tubing design. The spacer provides a slight swirl to the steam.

For the experiment when steam was used as an oxidizer, deionized water was chosen to be used for consistency in results. The water was then filled into the boiler (Figure 3-10), which is a cylindrical tube approximately 5 feet long \times 12 inches in diameter. The boiler holds approximately 5 gallons of water. On the bottom of the cylinder is a flange for connecting the heating element. In the top of the boiler was various tubes running through for a pre-heat section used in a previous experiment. This top portion was not used in this work. The boiler is rated for 600 psi, but was usually kept at approximately 350 psi.



Figure 3-10. Boiler. The boiler is used to generate saturated steam to provide an oxidizer to the burner. A 15 kW flange heater is used to boil the water. The boiler itself is sealed and capable of reaching pressures of 600 psi. The pressure can be set remotely and is controlled by a PID controller. Deionized water is used to provide consistent quality of steam.

The flanged heater was powered off of three-phase 208 V and produced 15 kW through its three resistive heating elements covered in Inconel 600. A three-inch pipe flange connected the element to the bottom of the boiler. The heater was connected to the control system, which was outside the test cell. The power for the heater was connected to an electrical relay. A

proportional–integral–derivative (PID) controller was then used to follow the pressure of the boiler.

From the boiler, there is a mechanical hand valve that is closed when heating. Once at the desired pressure, the valve is opened and steam fills the rest of the tubing up to the mass flow controller. There was an additional tubing in parallel to the mass flow controller that had a pressure relief valve set to 500 psi. If the boiler accidentally reached an unwanted pressure, the valve would open preventing failure.

For steam, the mass flow controller is a Rosemount 3095 Mass Flowmeter. The controller has several sized orifices to select for different ranges of flows. The one chosen could generate approximately 1 g/s of steam. The flowmeter contains a pressure differential meter to calculate the pressure drop across the orifice, which corresponds to a given mass flow rate. After the mass flow controller, the steam would travel 20 feet through 0.25" stainless steel tubing to the burner. The tubing was heated with heating tape for 10 feet of the tubing. The components of steam production are shown in Figure 3-11.

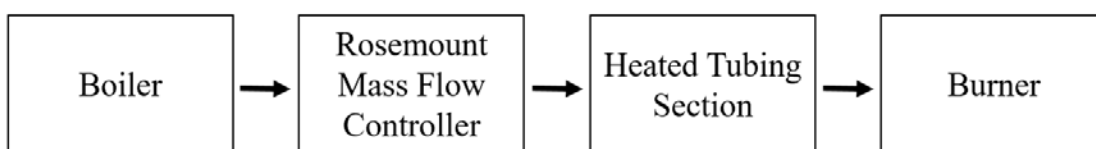


Figure 3-11. Path of Steam Generation. Water is boiled in the boiler at a set pressure. Saturated steam is tapped from the boiler and flows to the Rosemount mass flow controller. This controller works by using a known orifice size and a pressure differential meter. After the mass flow controller, the steam flows through a heated section to minimize losses to the environment. The tubing then connects to the burner at the Swagelok mixing tee.

For non-steam oxidizers, the gas is sourced from an industrial bottle size 200 to a pressure regulator and a MKS 1179 mass flow controller. 0.25" plastic tubing was routed to the burner inlet. No pre-heating section was needed.

Argon plasma flow: The plasma gas originates from an industrial bottles of ultra-high purity argon. A regulator decreases the pressure from ≈ 2000 psi for compatibility with the tubing and mass flow controller downstream. The mass flow controller is an MKS 1179. The MKS mass flow controller is connected to the MKS 647B mass flow programmer. The mass flow programmer allows for a simplified user interface and control of the set point and gas type. The flow desired is set and then mixes with the entrained aluminum. The mixture then proceeds down to the inner tubing of the coaxial tubing. Before aluminum is entrained, the plasma gas itself is used to create a plasma. Argon is a typical gas used in microwave torches due to extensive information on its use in the literature and relative low power requirements to form a plasma.

Argon aluminum powder flow: Argon gas also was used in the low velocity aluminum feeder to provide the pressure differential and carrier gas for entraining aluminum powder. A separate bottle of argon is connected to a regulator, without a mass flow controller. The regulator can be set as an inlet pressure to the low velocity aluminum feeder, which corresponds to an output aluminum mass flow rate. The argon line is routed to a ball valve controlled by a pneumatic solenoid. After the argon reaches the feed system and entrains the aluminum, it is routed to the tee mixing union where it mixes with the plasma gas. This mixture with the argon plasma gas flows to the inner tube of the coaxial setup. Argon was chosen for the powder flow to match that of the plasma gas in an attempt to minimize the effect on the plasma structure when introduced.

Nitrogen swirl flow: Nitrogen was used to provide a shield gas for the quartz tubing to prevent it from accumulating particles and preventing data from being collected. A size 200 industrial bottle of nitrogen is connected to a pressure regulator and then an MKS 1197 mass flow controller. The nitrogen flows through 0.25" plastic tubing to the bottom plate where it is attached to the two swirl ports.

High Velocity Aluminum Feeder and Shearing Device

Two separate aluminum feeders were used during experimentation. In the high velocity aluminum feeder, the aluminum was fed using an IDC N2 electrical cylinder to extend a piston through a quartz cartridge filled with aluminum. The electric cylinder was mounted on a vertical stand, shown in Figure 3-13. As the aluminum was pushed up through the top of the cartridge, it reached the shearing device. The shearing device (Figure 3-12) worked by passing inert gas through a slit that was 70 microns wide. This created a strong shear force for the top of the aluminum powder and entrained it in the gas. The mass flow rate was adjusted by changing the linear velocity of the electric cylinder. A schematic of the aluminum feeder and shearing device is shown in Figure 3-14.

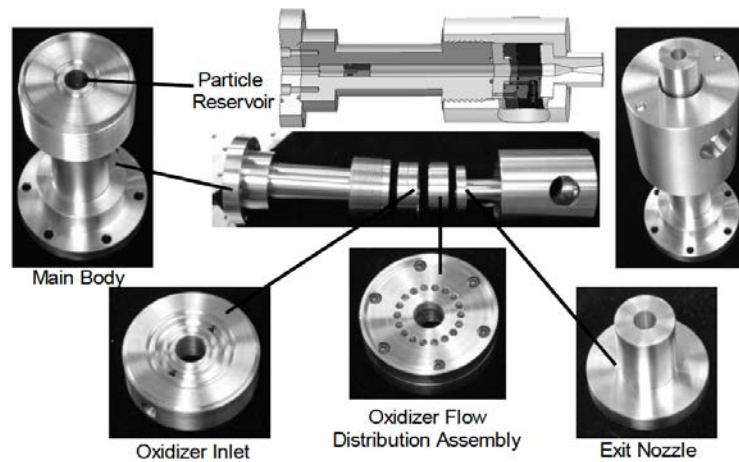


Figure 3-12. Shearing Device Components for High Velocity Aluminum Feeder.⁴⁴ The shearing device works by passing fluid through a small slit, which reaches high velocities and creates a strong shear force. As powder is fed into the particle reservoir, the top layer is sheared off and becomes aerosolized with the gas used. A linear actuator is used to consistently feed particles into the particle reservoir.



Figure 3-13. Electric Cylinder and Aluminum Cartridge Without Shearing Device. The electric cylinder shown was attached to a stand to mount the shearing device on. One the end of the cylinder was a piston that was pushed through an aluminum cartridge. The rate of the electric cylinder pushing the piston controlled the aluminum loading density. The linear velocity was controlled through the LabVIEW program.

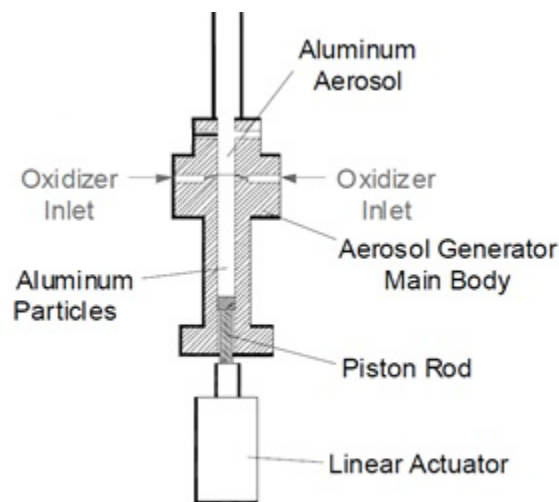


Figure 3-14. Schematic of High Velocity Aluminum Feeder and Shearing Device.⁴⁴ With the cross section view of the shearing device shows how the linear actuator moves particles to the shearing section and then leaves as an aerosol.

Calibration of High Velocity Feeder

To change the mass flow rate of aluminum in this configuration, the linear velocity of the actuator was changed. Changing the aluminum mass flow rate allowed for different fuel to oxidizer ratios to be examined. The mass flow was found empirically, due to losses through the tubing and the complicated entrainment method. The aluminum was fed into a container of water. This method was chosen since the high flow rate with micron-sized particles quickly became aerosolized and it was difficult to find a filter that was both small enough to catch the particles and strong enough to withstand the pressure. Once the aluminum touched the water, it clumped together and would float to the top. The mass of the water was weighed before and after a test, and the time between when the aluminum was first seen entering the water to the end was recorded. This provided an average mass flow rate per actuator linear rate. The results from calibration are shown in Figure 3-15.

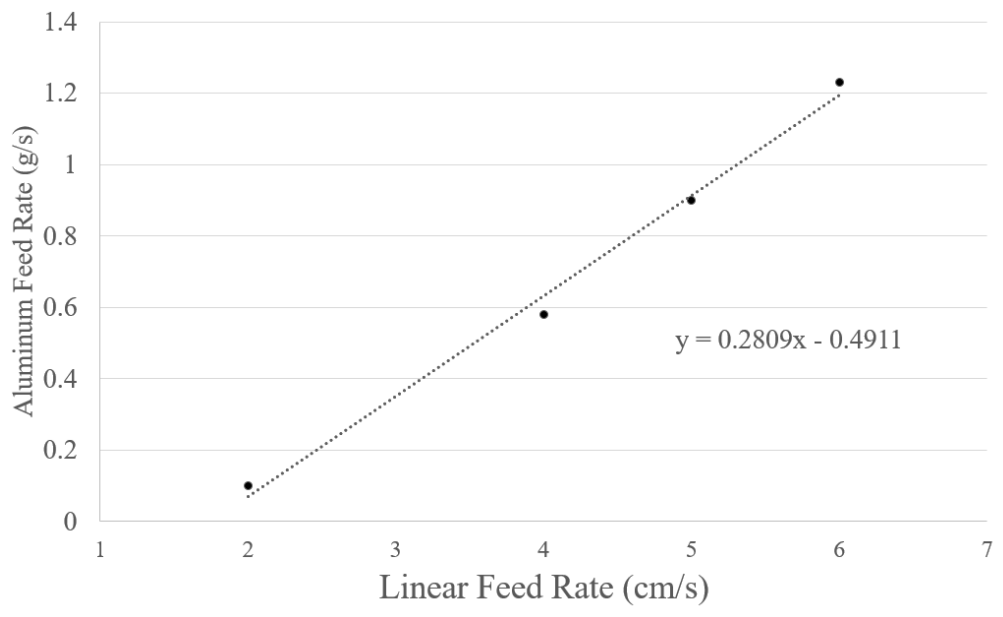


Figure 3-15. Calibration of Aluminum Mass Flow Rate for High Velocity Aluminum Feeder. A linear trend was found between the linear feed rate of the actuator and the amount of aluminum entrained. Calibration was performed by collecting the aluminum in a water container and weighing the container before and after and taking the time average.

Low Velocity Aluminum Feeder

The other aluminum powder feeder is a low velocity pressure based system. Aluminum powder was fed by using a pressure driven 2-inch-diameter cylinder shown in Figure 3-16. Aluminum powder is held in the cylinder compartment, which then leads down to a mesh screen for sifting followed by a 0.017-inch orifice. The mass flow is controlled by the pressure differential across the orifice. The top of the cylinder before the orifice is pressurized with argon, which is connected by 0.25" tubing from an industrial gas bottle. Argon was chosen as it mixes with the argon plasma gas downstream. After the orifice, the entrained aluminum is carried through 1/8" tubing until it reaches the 3/16" inner tubing.

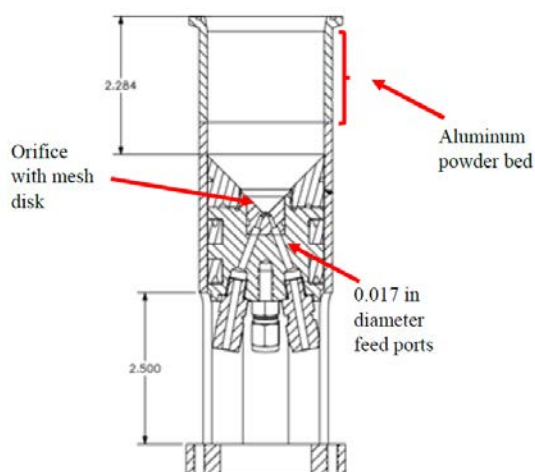


Figure 3-16. Low Velocity Aluminum Feeder Cross Section. This particle feeder works using a pressure differential over a small orifice to control the mass flow rate. It was found that consistent particle flow only occurred over 20 psig, which resulted in a 0.92 g/s mass flow rate. Since that mass flow rate approached the desired value, when using this particle feeder, the mass flow was kept constant and the oxidizer flow was changed.

Leading to the aluminum feed system, the argon flow was controlled by a solenoid valve, which allowed for remote starting and stopping of the aluminum flow. The solenoid worked when fed more than 60 psi of shop air. An electrical trigger was setup to pass the shop air when a 5-V signal was applied from LabVIEW.

It was determined through calibration that the minimum accurate mass flow that could be achieved was 0.92 g/s of aluminum at 20 psi. Pressures below 20 psi resulted in inconsistent particle delivery.

Cameras

Three types of cameras were used throughout the project: a Nikon D90 DSLR, Phantom v7.3 high speed camera, and a USB 3 camera.

The Nikon D90 DSLR was used to take various pictures of equipment and other pictures shown in this work. It also added as an additional colored view of some tests.

The Phantom v7.3 (Figure 3-17) was the main camera used for collecting visual data from experiments. The increased frame rate and ability to select short exposure times allowed for an understanding of the structure of a flame that could not be seen with other cameras. This was important since the reaction to the naked eye was an intense bright white light. At a resolution of 512×256 pixels, the camera could reach 22,000 FPS. For certain tests, the maximum framerate was not used to increase the length of time of a video. In addition, the EDR (extended dynamic range) feature was used to observe detail of the flame better without saturation.



Figure 3-17. Phantom v7.3 Camera. This high speed camera allowed for up to 22,000 FPS to be recorded. Another advantage of this camera is that the exposure rate could be set at one microsecond. The extended dynamic range also assisted in preventing saturation from the aluminum combustion, which was bright.

The USB 3 camera was used during the development of the system. This provided approximately 200 FPS and was easy to use. Problems arose when the camera was exposed to the microwave radiation environment (i.e., electromagnetic interference) and began to disconnect from the computer when the microwave power was greater than 300 W.

Spectroscopy

An Ocean Optics HR4000 spectrometer (Figure 3-18) was used to observe both plasma and thermal emissions. The spectrometer is responsive between 200–1100 nm. A fiber optic cable connected the spectrometer to a 5-mm collimating lens, which was used to collect light from a specific area of the plasma or flame (Figure 3-20). The spectrometer was connected to a laptop outside the test cell where the Ocean Optics software (Figure 3-19) was operated. The software allowed for setting of the scan time, number of scans and to be able to be triggered externally by LabVIEW.



Figure 3-18. HR 4000 Spectrometer. The spectrometer was used to capture emission from both the plasmas and combustion experiments. The HR 4000 had a large range from 200-1100 nm. The spectrometer allowed for both identification of ionized species, as well as temperature fitting aluminum particles using Planck's Law.

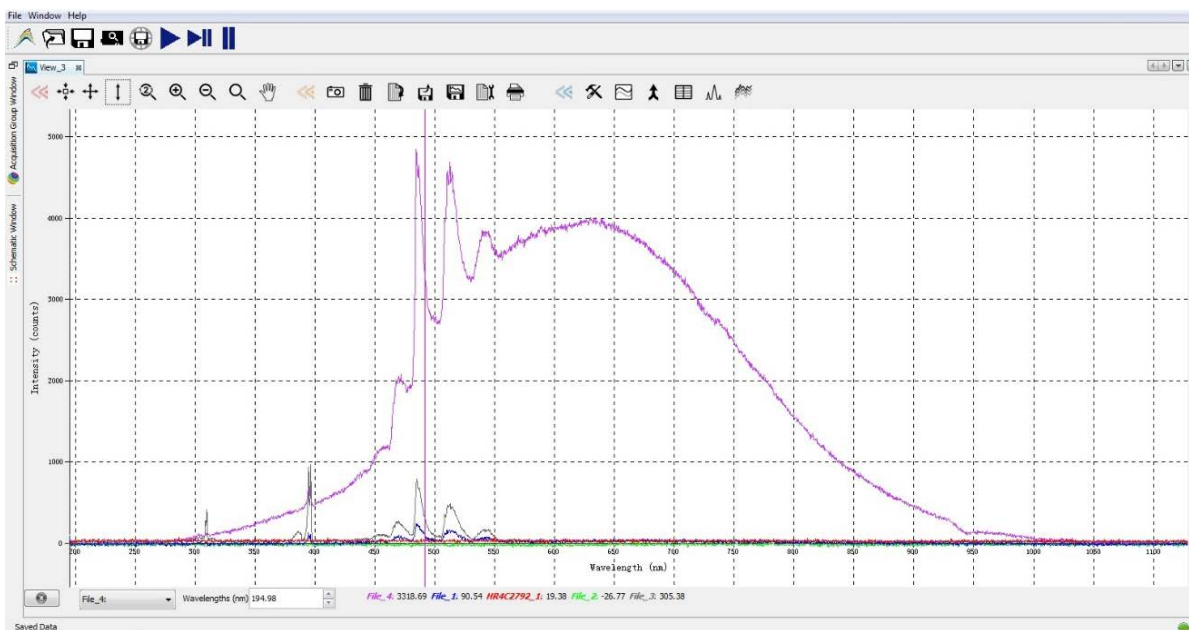


Figure 3-19. Example of Ocean Optics Computer Interface with Combustion Spectra Collected from HR 4000. Ocean Optics allowed for selection of parameters like integration time, as well as saving multiple spectra that were triggered externally through LabVIEW.

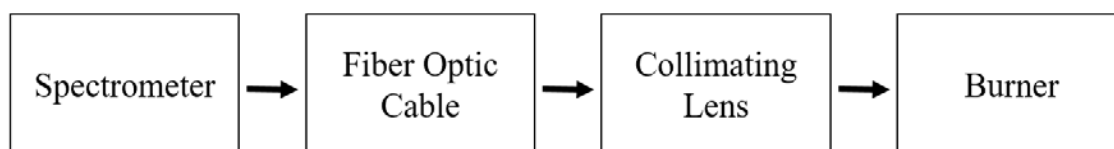


Figure 3-20. Spectrometer Component Layout. To accurately collect information from the burner, a fiber optic cable was connected to the spectrometer. The collimating lens was attached to the collimating lens and oriented at the burner. A laser pointer was used to accurately align the desired measuring location.

Ventilation

The products of combustion contained extremely hot particles. A ventilation system was set up to prevent damage from the hot products and collect the fine particulates. A shop-vac was used to collect the combusted particles. To prevent damage to the plastic tubing of the shop-vac, a bucket of water was placed under the end of the quartz tube. The water would provide a heat sink for the hot particles. The shop-vac was then positioned to collect any excess particles that were not collected by the water. The ventilation system is shown in Figure 3-21.



Figure 3-21. Water Bucket and Ventilation System. A bucket of water was placed under the burner to collect hot aluminum particles after they were burnt. A shop-vac was set up facing the top of the bucket to collect the small particulates that were not quenched by the water.

LabVIEW

LabVIEW was used as the central command of the necessary flow commands (Figure 3-22). The goal was to provide the user with a central point where all main controls could be quickly switched off if necessary, and to trigger the appropriate DAQ from the same external location. The features of the LabVIEW code, shown in Figure 3-23, include setting the microwave power, observing the actual forward and reflected power, interlock for power supply, and a switch for the solenoid to control aluminum flow. In addition, an input was included for triggering both the Phantom camera and HR4000 Spectrometer. When steam was being used, a LabVIEW code was used that contained a set point for the steam mass flow. The actual mass flow feedback was also read out in grams per second. This value was used when recording values.

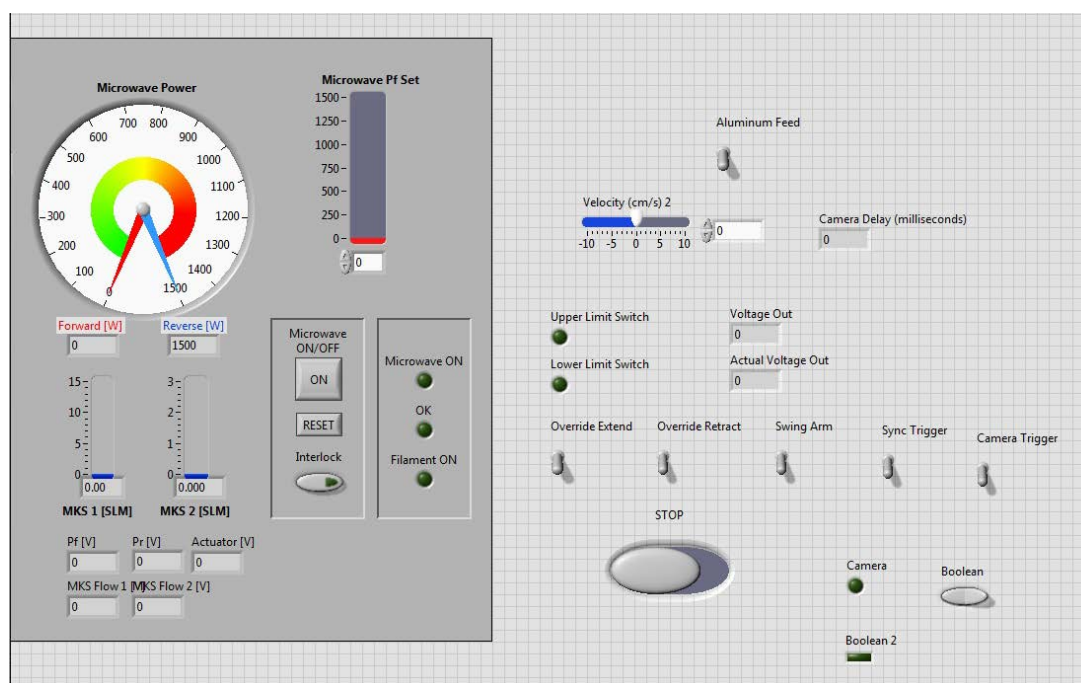


Figure 3-22. LabVIEW Graphical User Interface for Microwave Power and Aluminum Feed Control. One of the main controls on the LabVIEW program is the microwave power set, which allowed the forward power to be set on the high voltage supply. The actual forward and reflected power is read from the magnetron. Additionally, there is an interlock and microwave ON/OFF switch which toggle the power supply. The aluminum feed solenoid is controlled with a toggle switch. The camera and spectrometer are both trigger simultaneously to accurately match data temporally.

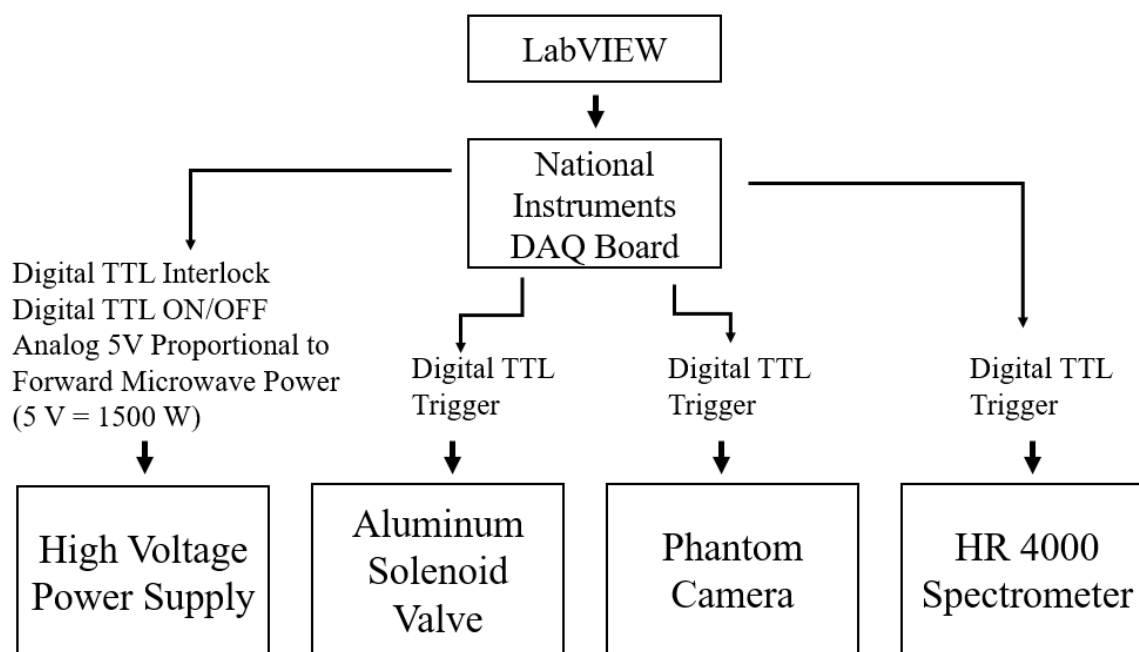


Figure 3-23. Main Components of LabVIEW Code. LabVIEW communicates with a National Instruments DAQ board, which is connected to various equipment. The high voltage supply has digital switches for the interlock and microwave ON/OFF switch. An analog output is used to control the forward microwave power. Digital triggers are also used on the solenoid valve, camera and spectrometer.

Addressing Safety

Various risks are taken when working with energetic materials and electromagnetic fields. To minimize risks, a hazard analysis was created to address and determine what precautions needed to be taken. Particulates from handling the raw aluminum powder and the product species should not be inhaled. A respirator and appropriate training was provided by ARL. The products of combustion were quenched in water, and then collected with a shop-vac during testing. A NARDA meter was used to ensure that microwaves stayed below the 10 mW/cm^2 limit recommended by OSHA. A hydrogen meter and carbon monoxide alarms were installed to protect from dangerous gas buildup. Ventilation fans were used to clear out the room

and prevent asphyxiation from inert gas buildup. The NARDA meter and respirator are shown in Figure 3-24.



Figure 3-24. NARDA meter and Particle Respirator. The NARDA meter was used to measure for electromagnetic radiation leaks and ensure that the room was safe to enter. The respirator was used to prevent breathing in aluminum particles.

Chapter 4

Experimental Development

This chapter explains the iterations of the injector design for the fuel, oxidizer, and plasma flows. Work began with a single tube injector which was used to form an argon plasma and understand the effects of different powers and volumetric flowrates. Additionally, a steam plasma was formed and compared to the argon plasma. The injector was then switched over to a coaxial injector. An argon plasma was formed and characterized over various flowrates and powers to observe structural changes. Spectroscopy was used to compare an argon plasma to an argon plasma entrained with steam. Additionally, the interaction between an argon plasma and aluminum powder was investigated. Finally, aluminum–steam combustion tests were performed using the high velocity aluminum feeder. Aluminum mass flow rates and microwave power was varied over the course of different tests.

Single Tube Injector

Originally, a single tube system was used to verify that a plasma discharge could be achieved and that the magnetron was working correctly. The 3/16" tubing was oriented upward as shown below. A Faraday cage was used to contain the microwaves for the safety of personnel and equipment. The Faraday cage was made out of stainless steel mesh (with 0.25" spacing) that was spot welded together to create a cylinder. In the single tube injector setup, there was not an adjustable tuner as suggested in the coaxial configuration in the literature review. The tube itself was moved to adjust the coupling. Ignition of an argon plasma typically occurred between 250–300 W when flowing 1 SLM of argon. The power could then be turned down once ignition was achieved. The plasma consisted of a single filament that rotated around the edge of the tube

consistently. The plasma appears cone-like in Figure 4-1 due to the exposure time of the camera. The picture captures similar to what the human eye saw. The results match those that have been reported in the literature for microwave-based torch plasma ignitions. Once the flow rates were increased to around 3 SLM, the filament became stagnant, which was avoided due to large thermal concentrations that could damage the tubing.

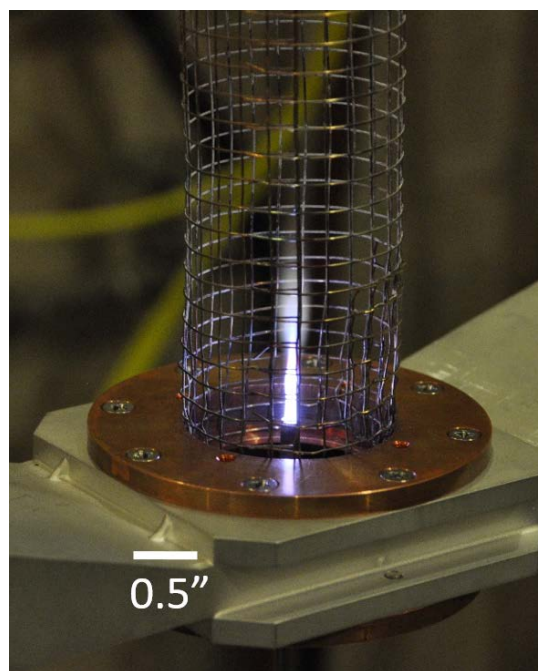


Figure 4-1. Upright Atmospheric Argon Plasma: 1 SLM Argon, 200 W of Microwave Power. An upright argon plasma was achieved to ensure that the equipment was all working correctly. At low volumetric flow rates (<3 SLM), the filament oscillated consistently. Once the flowrate was increased, the filament became stagnant.

The system was then inverted (Figure 4-2) to better replicate other burner designs and ease the future collection of combustion products. After inverting the single tube configuration, it was noticed that buoyancy forces were significant to the shape, specifically the recombination zone, of the plasma. In the upright case, the recombination zone is thin and looks like an extension of the plasma itself. In the upside-down configuration shown in Figure 4-3, the

recombination zone mushrooms outward and forms a ball that is several diameters bigger than the plasma.

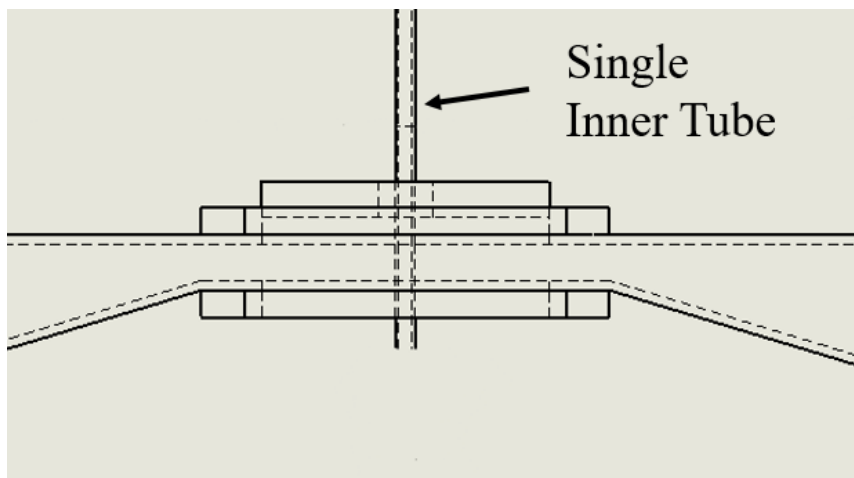


Figure 4-2. Inverted Single Tube Plasma Torch. The single tube configuration was similar to the other coaxial injector designs discussed previously, however there was only one tube to couple microwaves. There was not a spacer since there was only one tube. The axial location of the injector tip more sensitive in the single tube configuration.

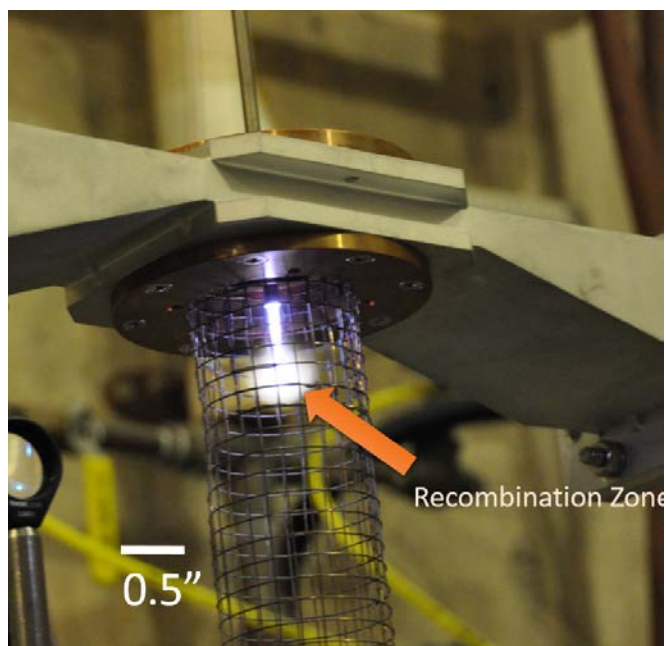


Figure 4-3. Inverted Argon Plasma with Noticeable Recombination Zone. When an argon plasma was formed in the atmosphere, the nitrogen would react with the plasma and cause a plume where the radicals were recombining. This led to the movement towards a quartz tube that would separate the experiment from the surround atmospheric air.

Once a plasma formed, the microwave power was increased to observe the effect on the plasma structure. The recombination zone was seen to be a function of microwave power. Around 500 W, the recombination zone reached the Faraday cage due to buoyancy forces. The yellowish hue is likely the interaction of the excited species with the surrounding nitrogen and oxygen. An argon plasma at different power levels is shown in Figure 4-4.

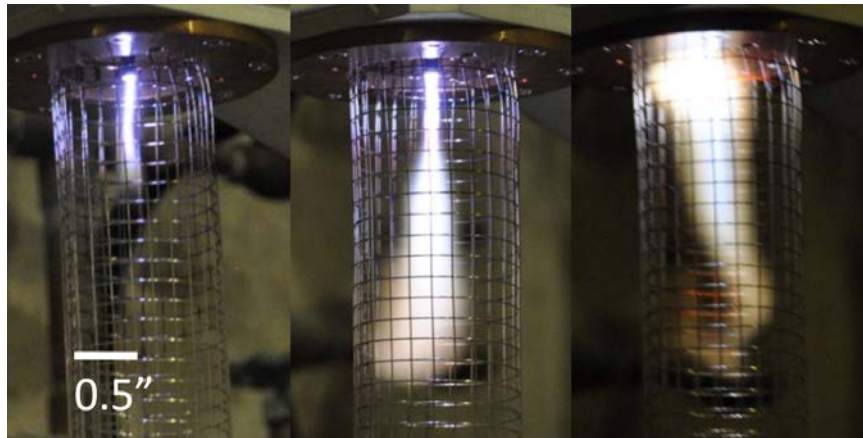


Figure 4-4. Argon Plasma: 2 SLM; Power = 100 W, 300 W, and 500 W (from left to right). As the power increased to an argon plasma, the plasma recombination zone grew significantly. Surprisingly, the plasma filaments only became slightly larger. The filaments have a limit of the amount of power than can be absorbed. After a certain point, the power is transferred to the surround, not the argon gas.

It was discussed that using a steam plasma instead of an argon plasma would be favorable since it could eliminate a diluent, argon. A plasma with steam alone was created in the single tube injector. The plasma consisted of a single filament that did not oscillate as consistently as the argon plasma. The steam required about double the microwave power (≈ 500 W) to achieve plasma ignition (Figure 4-5 and Figure 4-6). Due to the heat of the steam, condensation, and slight variability in flow, the steam plasma structure varied and frequently extinguished.

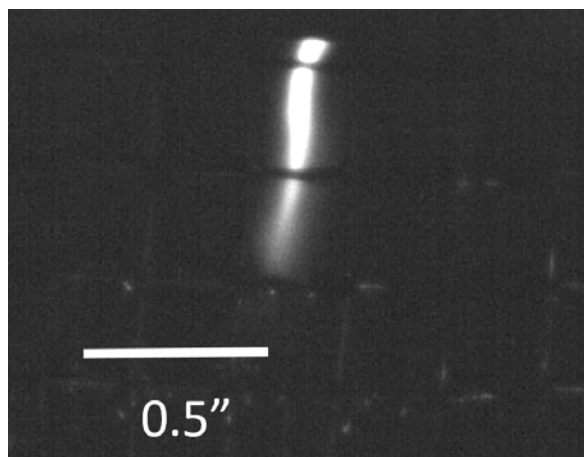


Figure 4-5. Steam Plasma Filament: 1 g/s, 500 W of Microwave Power. A steam plasma was formed, however it was difficult to achieve stability. The plasma would extinguish when liquid condensation would become entrained. Argon proved to be a better gas for forming a plasma.

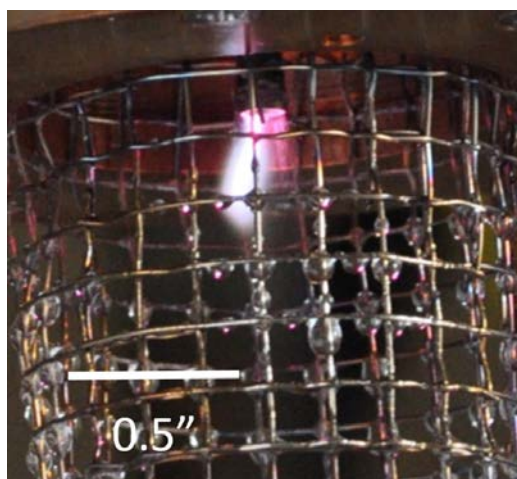


Figure 4-6. Steam Plasma Filament: 1 g/s, 500 W of Microwave Power (colorized). A steam plasma was formed, however it was difficult to achieve stability. The plasma would extinguish when liquid condensation would become entrained. Argon proved to be a better gas for forming a plasma.

Water is a polar, covalently bonded molecule, thus it is more difficult to excite than the monoatomic argon gas. This explains why it required much more energy to excite the steam as compared to argon. As will be seen in the next iterations of the design, when argon and steam were mixed together, the formation of an argon plasma would always occur before that of a steam plasma.

Coaxial Injector

One of the goals of the injector was to include the fuel, oxidizer, and plasma flows all in one device. To achieve this, a coaxial injector system was designed. Additionally, it was thought that a premixed flow would perform better due to the nature of diffusion flames. In the annulus of the system, argon would flow for the plasma. The inner tube carried a mixture of aluminum powder, argon carrier gas, and steam. A spacer was placed inside the outer tubing to hold constant the spacing between the two tubes and to aid in microwave coupling. The new configuration included the desired premixed fuel and oxidizer and the plasma would occur on the outside of the outer tube of the injector. Once the coaxial configuration was determined, additional characterization of the plasma was done for the new setup.

The original coaxial configuration had a premixed configuration with aluminum, argon carrier gas, and steam in the core flow; argon plasma gas in the annulus; and nitrogen as the surrounding shield gas as seen in Figure 4-7.

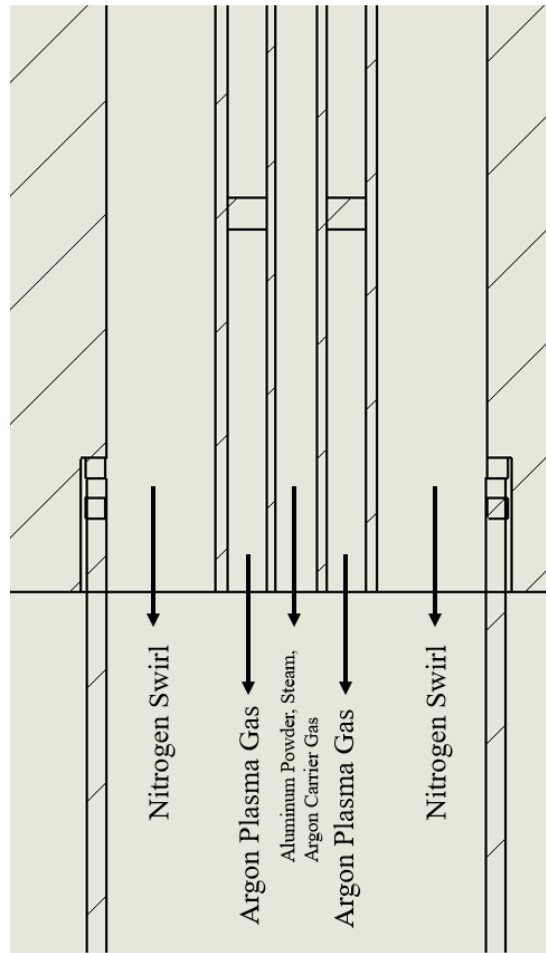


Figure 4-7. Premixed Coaxial Injector Flows. For the premixed configuration of the coaxial injector, nitrogen shield gas was flowed around the quartz tube. The annulus contained the argon plasma gas for creating a plasma on the outer tubing. The core flow contained the aluminum powder, argon carrier gas and steam. The argon carrier gas needed to be sufficient to counter the pressure from the steam line.

Figure 4-8 shows a simulation performed by Palomino using ANSYS HSFF. The model was able to determine the best position of the spacer located in the injector to maximize the electrical field. The region right at the tip was desired to have a strong electrical field to form a plasma.

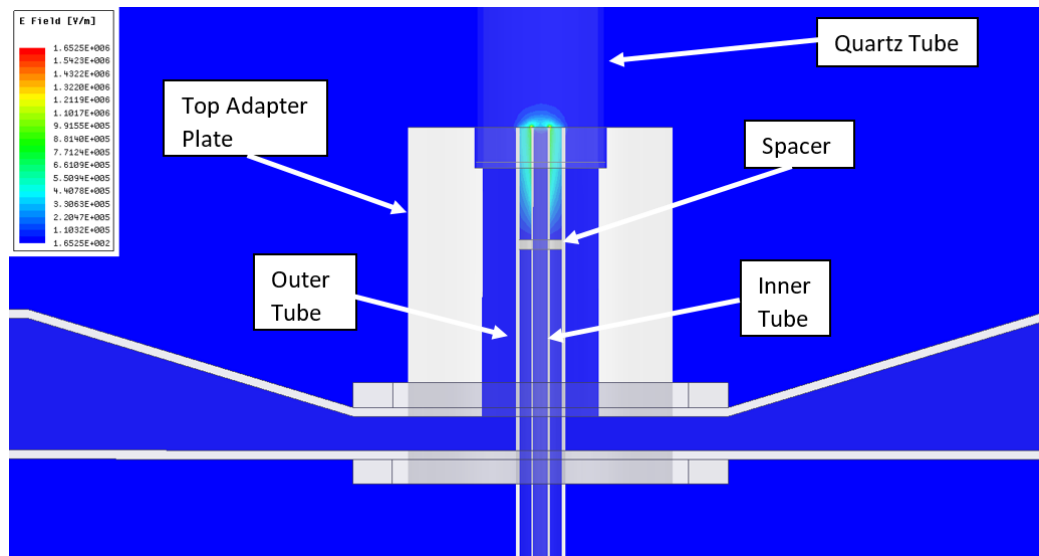


Figure 4-8. Electromagnetic Simulation Performed by Palomino at the Applied Research Lab for the Coaxial Injector. ANSYS HFSS models electromagnetic fields and is used to determine the strength of the electric field created on a specific geometry. The software could not determine if a plasma itself would form, however it is helpful in determining optimized coupling positions of the spacer and the tuner on the waveguide.

Plasma

Originally, only the argon plasma gas was flowed to the annulus of the coaxial tubing to compare the configuration to the single tube system (Figure 4-9). The plasma filaments attached to the outside of the outer tubing, which was expected. Multiple filaments formed compared to the single filament in the single tube design. Geometrically, the filaments were much longer than the single tube system due to the fact that it was possible to greatly increase the flowrates with the increased area. A plasma was achieved over the range of 5–30 SLM of argon. The additional filaments likely occurred due to better coupling in the new coaxial design. Only so much power can physically form one filament before it is split between multiple filaments.

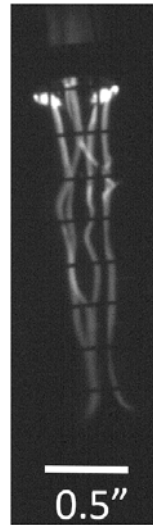


Figure 4-9. Coaxial Injector Argon Plasma Displaying Multiple Filaments: 10 SLM of Argon Through Annulus, 300 W Microwave Power. An argon plasma was formed in the coaxial injector with argon in the annulus. Unlike the single tube injector, multiple filaments formed and were significantly longer. Also, the volumetric flow rate was no longer an issue with stagnation.

Spectroscopy was used to analyze an argon plasma. A 5-mm collimating lens and a fiber optic cable was focused on the base of the injector. Using a collimating lens spatially integrates the measurement. As seen in Figure 4-10, the intensity of measurements increased as the microwave power was increased, with 600 W being the largest intensities.

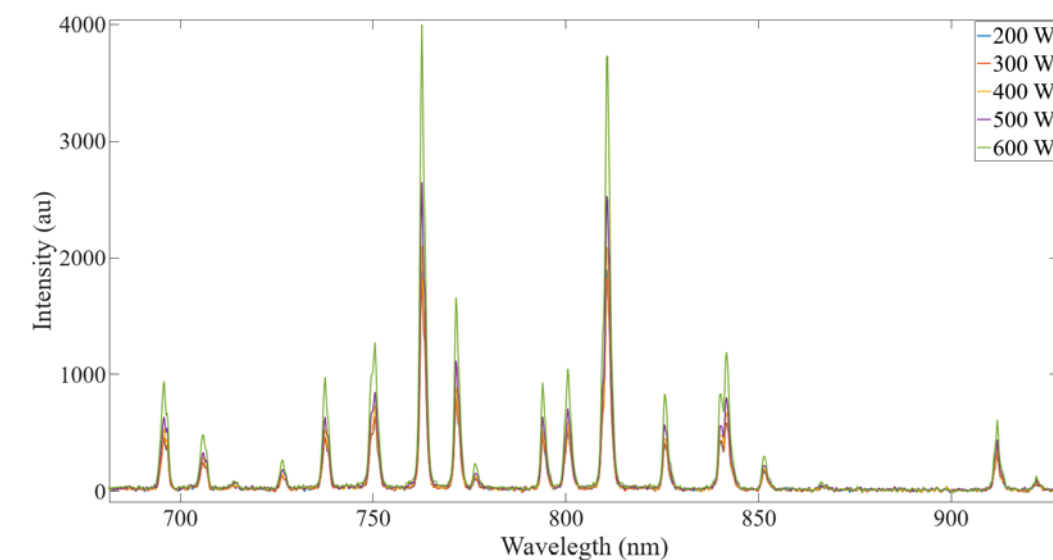


Figure 4-10. Increased Intensity Varying Microwave Power for an Argon Plasma: 10 SLM — 200 W (blue), 300 W (red), 400 W (yellow), 500 W (purple), 600 W (green). Spectra was recorded at various power levels. The intensity of the argon lines shown increased as microwave power increased.

Steam was then added through the center tube to examine the effect on the plasma structure. When added, the filaments significantly shrunk in size (Figure 4-11 and Figure 4-12). With only argon plasma gas and steam, a single longer filament would appear. The longer filament was around three times longer than the other filaments. Filament length of only argon was seen to be a function of both power and flow rate. The addition of steam acted as a power sink and lessened the significant changes observed to filament lengths with only argon. As the power increased, the steam transitioned into completely superheated steam. At low powers, condensation could be seen in the quartz tube, but transitioned to superheated steam around 800 W. This was evidence that a large portion of the microwave power was being absorbed by the steam instead of the argon filaments.



Figure 4-11. Argon Plasma with Entrained Steam: 10 SLM of Argon in the Annulus, 1 g/s Steam, 750 W. The plasma filaments significantly shortened after the introduction of steam. The steam absorbed power, so less was present in the plasma. Therefore, less power means less and shorter filaments. The plasma is no longer oversaturated.

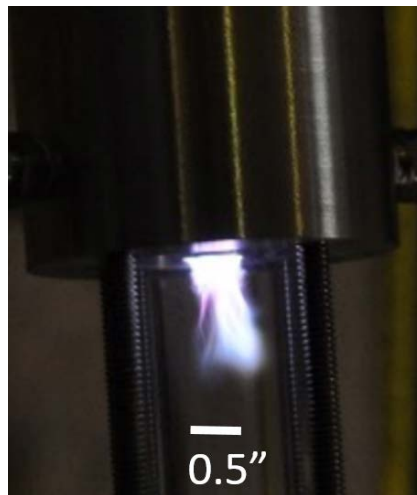


Figure 4-12. Argon Plasma with Entrained Steam: 10 SLM of Argon in the Annulus, 1 g/s Steam, 750 W (colorized). The plasma filaments significantly shortened after the introduction of steam. The steam absorbed power, so less was present in the plasma. Therefore, less power means less and shorter filaments. The plasma is no longer oversaturated.

The effect of the addition of the argon carrier gas core flow on the argon plasma gas in the annulus was observed for several conditions. When reaching the amount of carrier gas to successfully entrain aluminum in the core flow (30 SLM), the plasma observed was a long narrow

conical shape seen below. More filaments occurred than in the previous condition without the carrier gas (Figure 4-13).

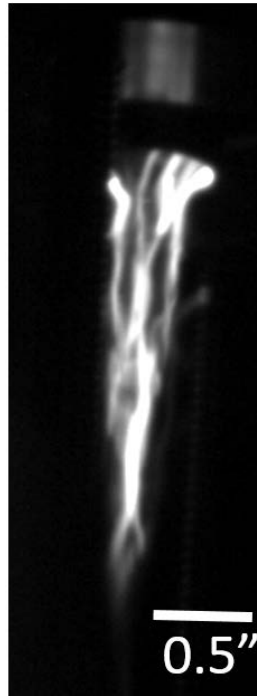


Figure 4-13. Argon Plasma with Carrier Gas: 10 SLM of Argon in the Annulus, 30 SLM Argon Carrier Gas in the Core Flow, 300 W of Microwave Power. Once the argon carrier gas was added to the standard plasma, the filaments grew to significantly long filaments.

Achieving a plasma with argon plasma flow, steam, and the argon carrier gas was difficult due to the amount of diluent and the tendency of water to condense. The first attempt was to achieve an argon plasma with the plasma flow and the carrier gas, then the steam could be introduced. The addition of steam, specifically the transient stage and water that condensed in the lines, extinguished the plasma. Next, all flows were allowed to flow without the presence of microwave power. The power was steadily increased at intervals of 100 W. Around 1000 W, the plasma formed, but condensation was still present. This was hypothesized to be due to the large amount of argon gas mixed in at $\approx 20^\circ\text{C}$. Heating tape was added on the argon lines to increase the argon temperature and limited the condensation seen around the plasma. Once the plasma was

formed, it was allowed to reach a steady state and all water to be evaporated from the walls of the quartz tube. The progression of the filament is shown in Figure 4-14.

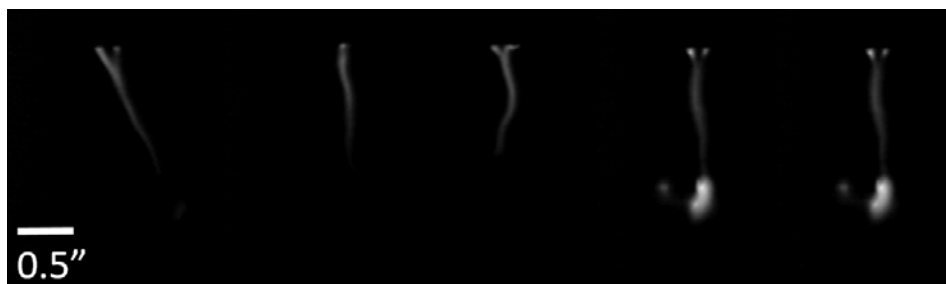


Figure 4-14. Progression of a Plasma: 10 SLM of Argon Annular Flow, 1 g/s of Steam and 800 W Microwave Power — 2 ms Between Frames. The high speed camera allows for the progression of the argon-steam filament to be captured. It was important to note that the filament did not oscillate in set pattern. The plasma moved frequently, but seemed random.

The plasma that formed in this configuration consisted of primarily one filament. Spectral data were compared between a 300-W argon plasma and an 800-W steam plasma (Figure 4-15).

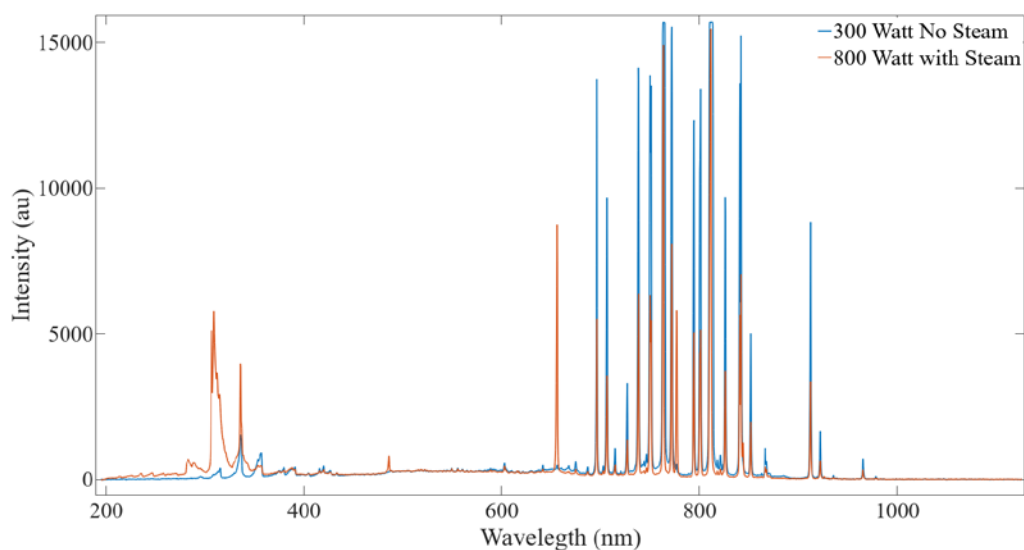


Figure 4-15. Comparison of Argon Plasma Spectra with and without Entrained Steam — No Steam (blue), With Steam (orange). Overall, both plasmas contained the same argon emission lines. When steam was added, OH, H and O radicals were present in significant amounts. The steam was interacting with the plasma and becoming excited.

The argon lines between 750–850 nm all appeared in both cases. When the steam was present, some significant radicals appeared. The radicals from steam include OH (Figure 4-16),

which occurs as a large band from 280–320 nm, H_{β} at 486 nm, H_{α} at 656 nm (Figure 4-17), and O I at 777 nm (Figure 4-18). These emissions are consistent with those found in research on water microwave discharges. This is also important since the more radicals present when the aluminum particles vaporize, the quicker the reaction can take place.

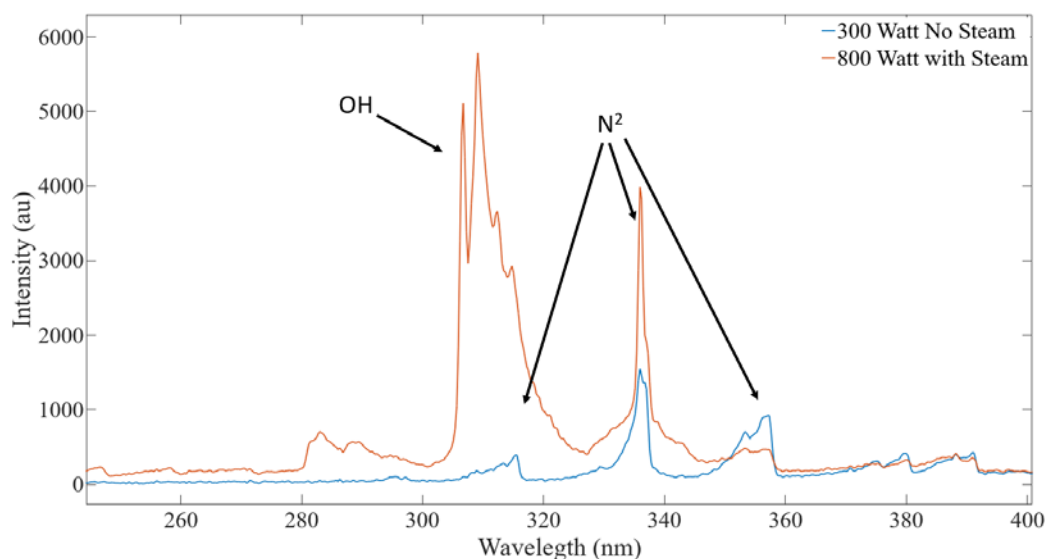


Figure 4-16. OH Radical Increase in Intensity When Steam Is Entrained — No Steam (blue), With Steam (orange). OH radicals are much stronger intensity in the case with steam entrained. Potentially, some water vapor could have been introduced from impurities in the industrial gas, indicating small OH emissions in blue. The steam itself is interacting with the plasma and creating radicals. These radicals are important in continuing reactions after combustion has begun.

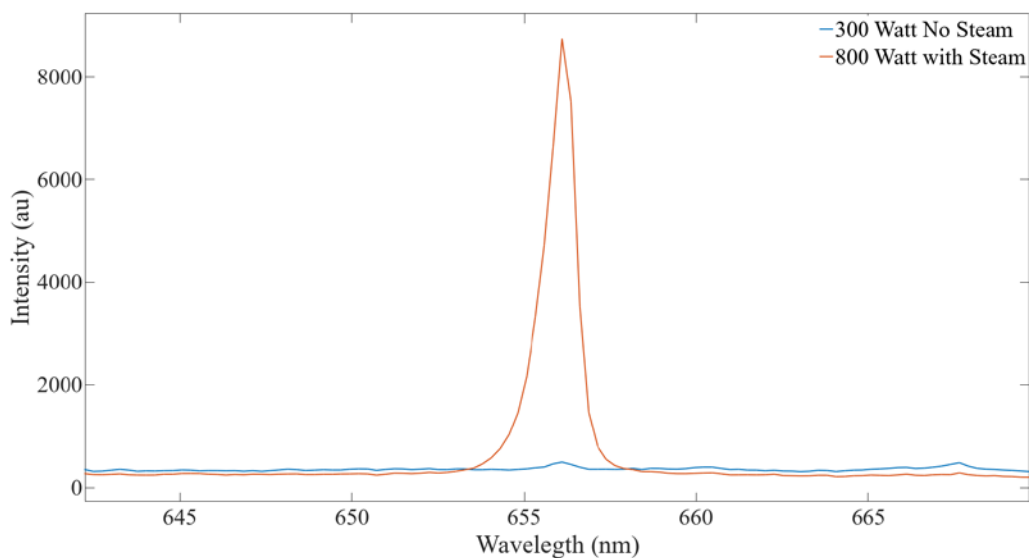


Figure 4-17. H-Alpha Emission Present When Steam Is Entrained — No Steam (blue), With Steam (orange). Hydrogen alpha was also seen when steam was entrained. This radical provides significant improvement to combustion.

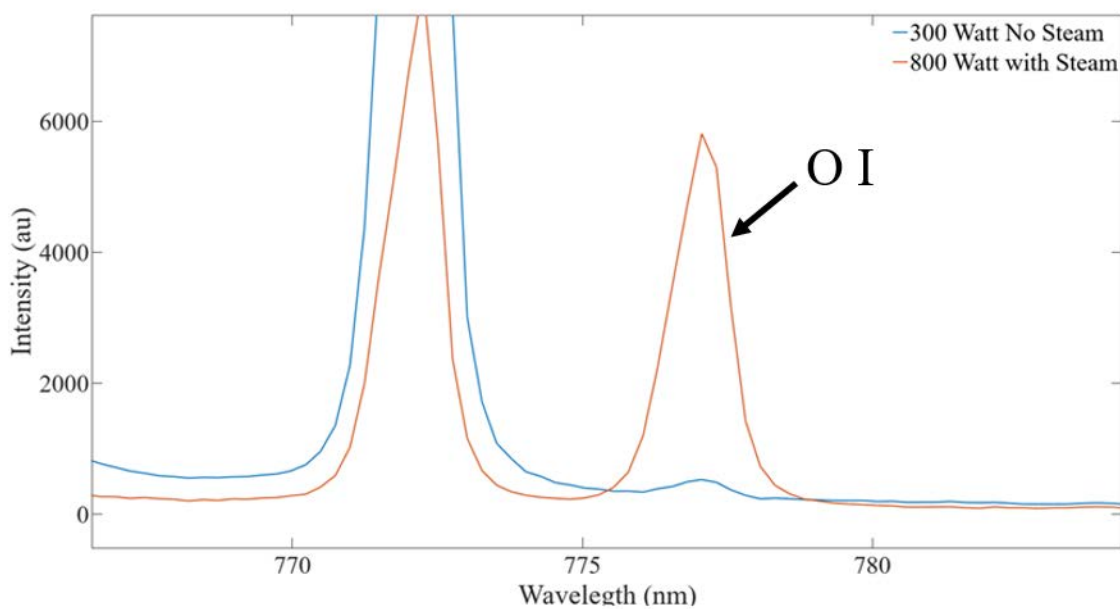


Figure 4-18. Oxygen Radical Emission Present When Steam Is Entrained — No Steam (blue), With Steam (orange). Along with OH and H, O is present in the entrained steam plasma. The plasma interaction with the oxidizer is more than just thermal heating.

Aluminum Through an Argon Plasma

One of the major investigations for this work is to determine the effect of the plasma on aluminum particles. Aluminum particles were passed through an argon plasma to observe the effect of the plasma without oxidizer, thus isolating the direct effect of the plasma. The following flow conditions were used: 7.5 SLM argon plasma gas, 30 SLM argon carrier gas, 1.92 SLM nitrogen swirl, and 0.1 g/s of aluminum. 300 W of microwave power was used to achieve the plasma structure. Visually, when aluminum passed through the plasma, both a blue light and a strong white light were given off, which can be seen in Figure 4-19.

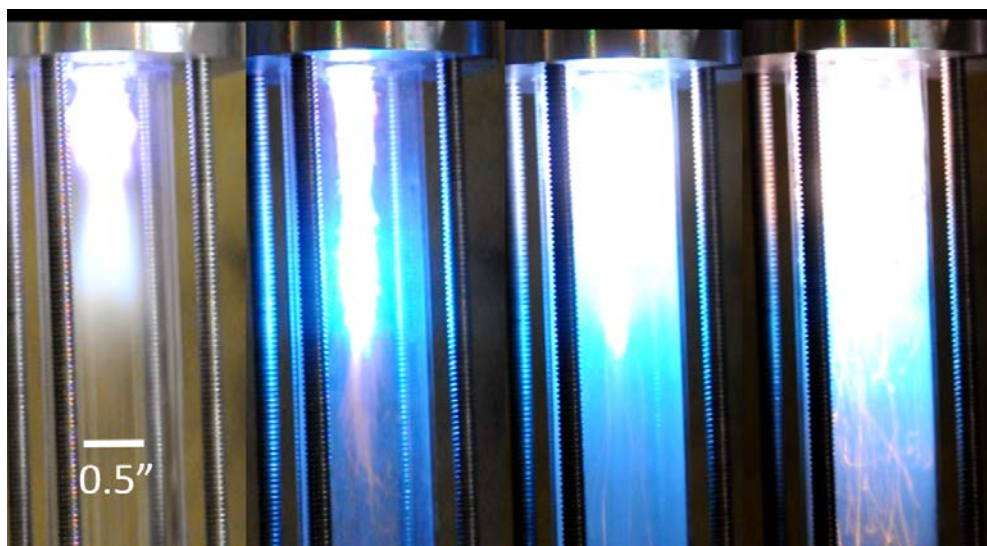


Figure 4-19. Aluminum Powder Passing Through an Argon Plasma — 300 W and 0.1 g/s of Aluminum. While aluminum was flowed through an argon plasma, significant light and audible sounds were observed. In addition, reaction of the particle can be seen at the end of the particle with the yellow-orange color. Even without oxidizer, the plasma is effecting the aluminum particles.

The emissions for both the baseline plasma and that collected during the entrainment of aluminum were recorded (Figure 4-20). The results of the spectra with aluminum entrained differed significantly from the baseline of pure argon plasma at the same conditions. 396.1 nm is an Al I line and appears predominantly when the aluminum is entrained (Figure 4-21), but not in

the baseline plasma. The next difference is the addition of peaks ranging from 440–540 nm, which are the peaks for AlO that match those shown for laser ablation.²⁵ Since the chamber was purged with inert gas, there is no oxygen present in the experiment. This AlO emission must be coming from vaporization of the Al_2O_3 on the surface of the particles.

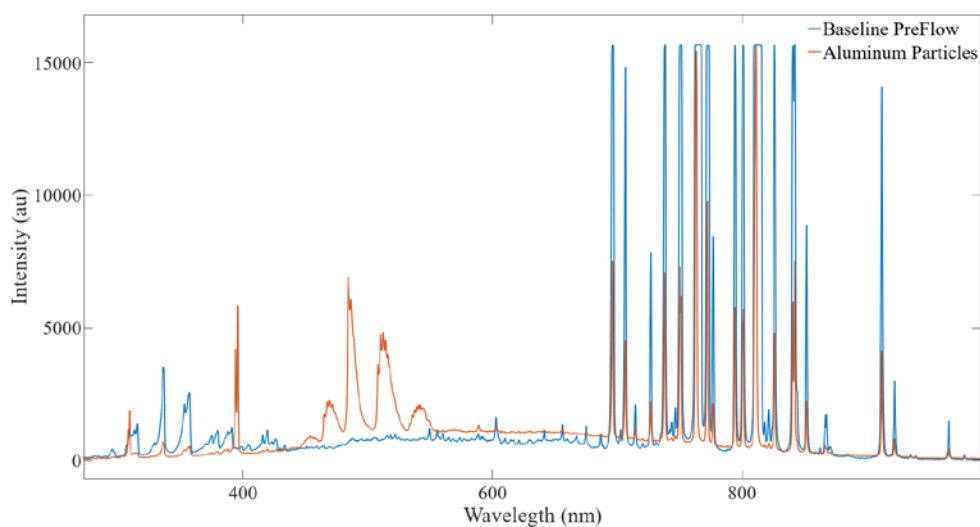


Figure 4-20. Comparison of Argon Plasma (Blue) and Aluminum Passing Through an Argon Plasma (Orange): 7.5 SLM of Argon Plasma Gas, 1.9 SLM Nitrogen Swirl, 0.1 g/s of Aluminum, 30 SLM Argon Carrier Gas, and 300 W of Microwave Power. The overview of the spectra comparing an argon plasma to the argon plasma with aluminum shows the main different occurs in the lower wavelengths.

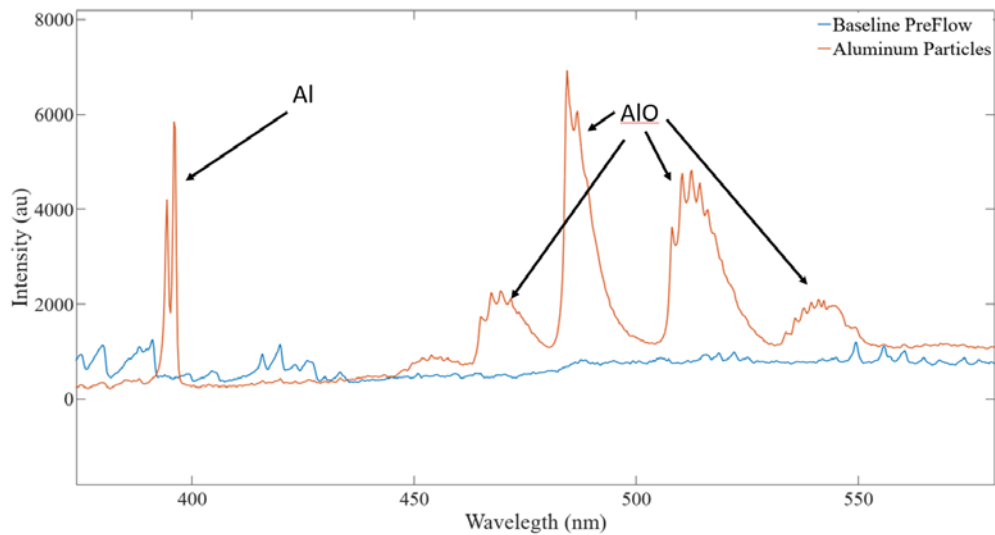


Figure 4-21. Aluminum and Aluminum Oxide Spectra: 7.5 SLM of Argon Plasma Gas, 1.9 SLM Nitrogen Swirl, 0.1 g/s of Aluminum, 30 SLM Argon Carrier Gas, and 300 W of Microwave Power. AlO and Al emission lines were clearly visible in the spectra. The since there was not oxidizer in the experiment, AlO must have come from the dissociation of Al_2O_3 . This means that the oxide shell was melted and vaporized.

Another test, shown in Figure 4-22, was performed with a larger mass flow of aluminum and recorded with the monochrome USB 3 camera. The results show what looks like the bursting of some particles when they interact with the filament of the plasma. This makes sense since AlO is observed in the spectra, which would correspond to the glowing oxide shell shown in the video. The particles are also seen breaking into even smaller pieces. This vaporization of the pure aluminum inside the particle is also seen in the spectra.

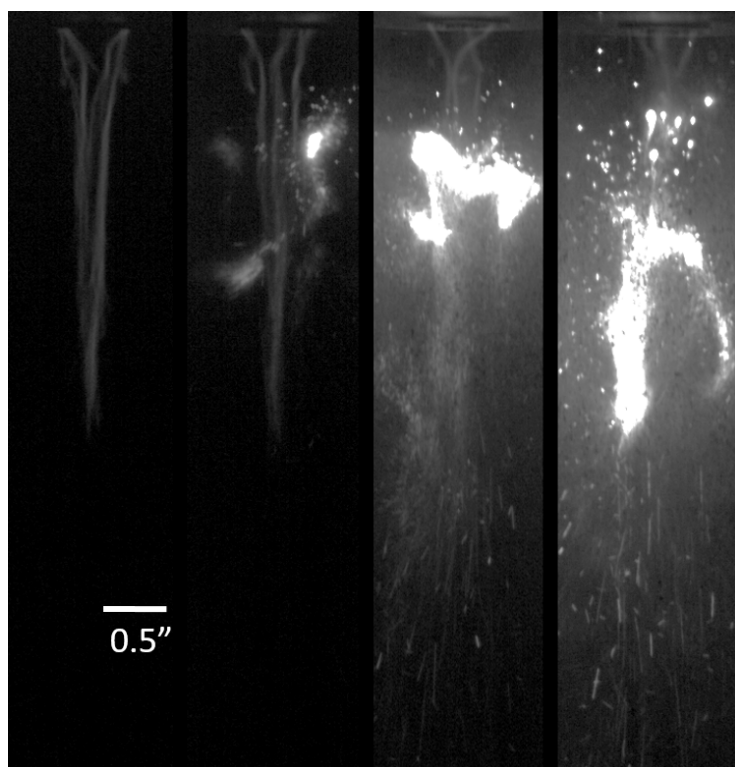


Figure 4-22. Aluminum Passing Through Aluminum Plasma (Monochrome). The frames from the video show that particle seem to explode when they encounter the plasma filament. Small hot particles can be seen being spray in the final two frames.

Aluminum post plasma was collected from the walls of the quartz tube and observed with a scanning electron microscope (SEM). The size distribution was visually seen to change. With the SEM it was confirmed that there were large agglomerations about a 100 times the size of the base particles (Figure 4-23 and Figure 4-24). Some of the particles looked to be fused to the surface, while other looked like they actually melted and merged. On the smaller individual particles (Figure 4-25), there was much less bayerite (aluminum hydroxide). Bayerite forms on particles that have been stored for a significant amount of time and have slowly interacted with the gases in the air. Additionally, some of the particles developed a “fuzzy” outer shell. The plasma interaction altered the surface of the particles even if they did not vaporize. The particles that are vaporized should be able to react easier with the other particles that began to have surface reactions.

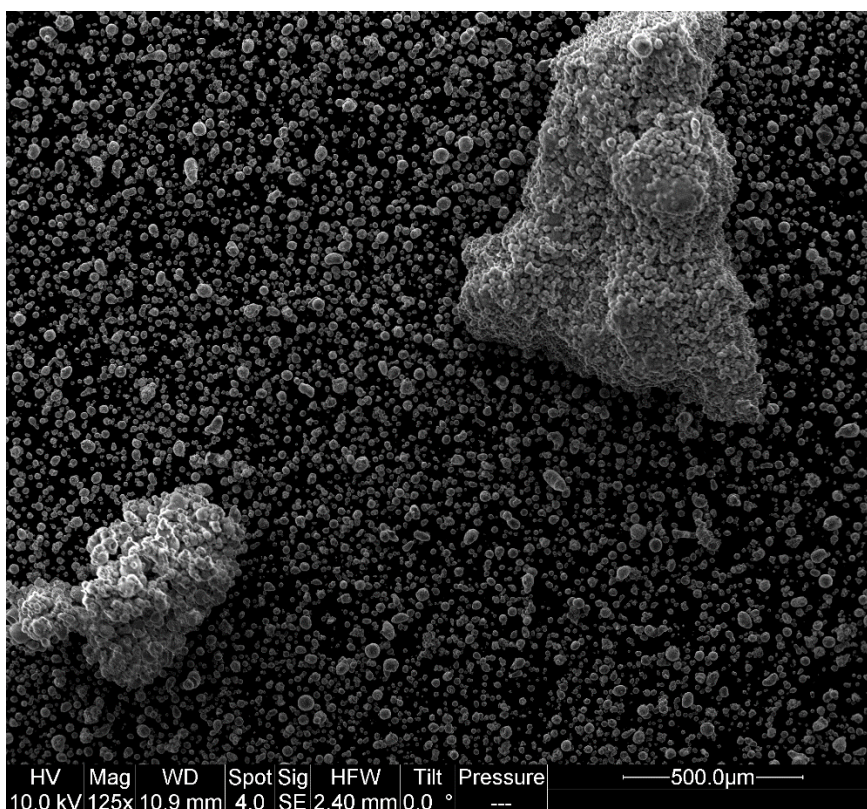


Figure 4-23. Large Agglomerations of Aluminum Collected After the Plasma 125× Magnification. After the aluminum was flowed through the argon plasma, the products were collected and examined with a SEM. Large agglomerations indicate that the particles were melting and collecting together before they cooled. These particle had the oxide shell either partially melted or completely vaporized. Either indicate combustion is possible.

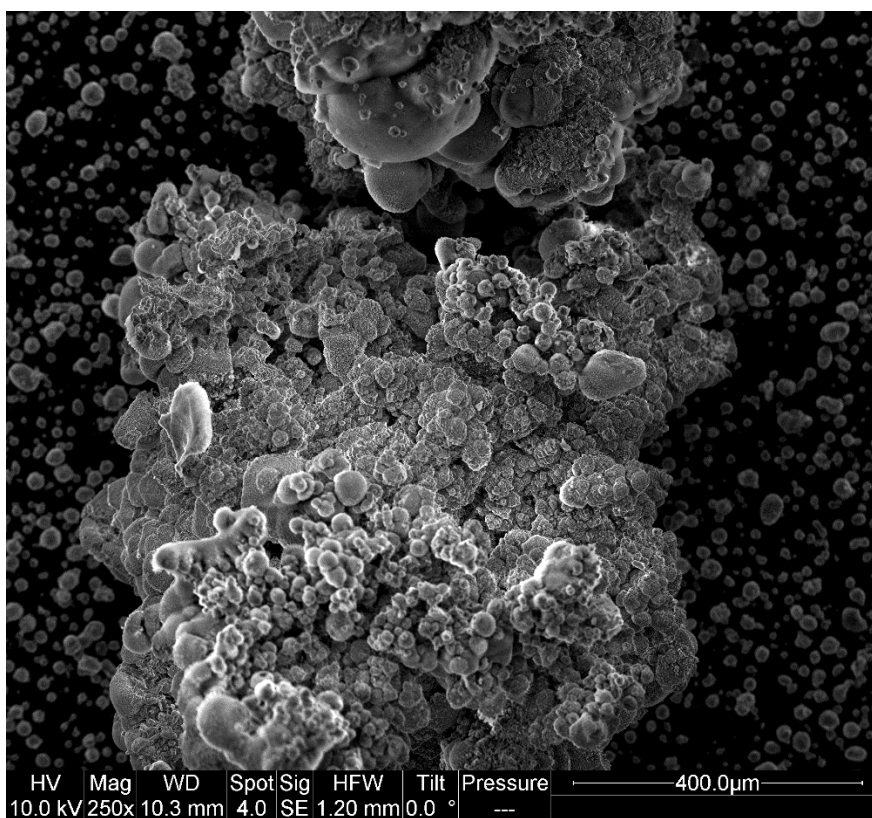


Figure 4-24. Large Agglomerations of Aluminum Collected After the Plasma 250× Magnification. A closer look confirms that some particles look melted together completely, while some particles were partially fused.

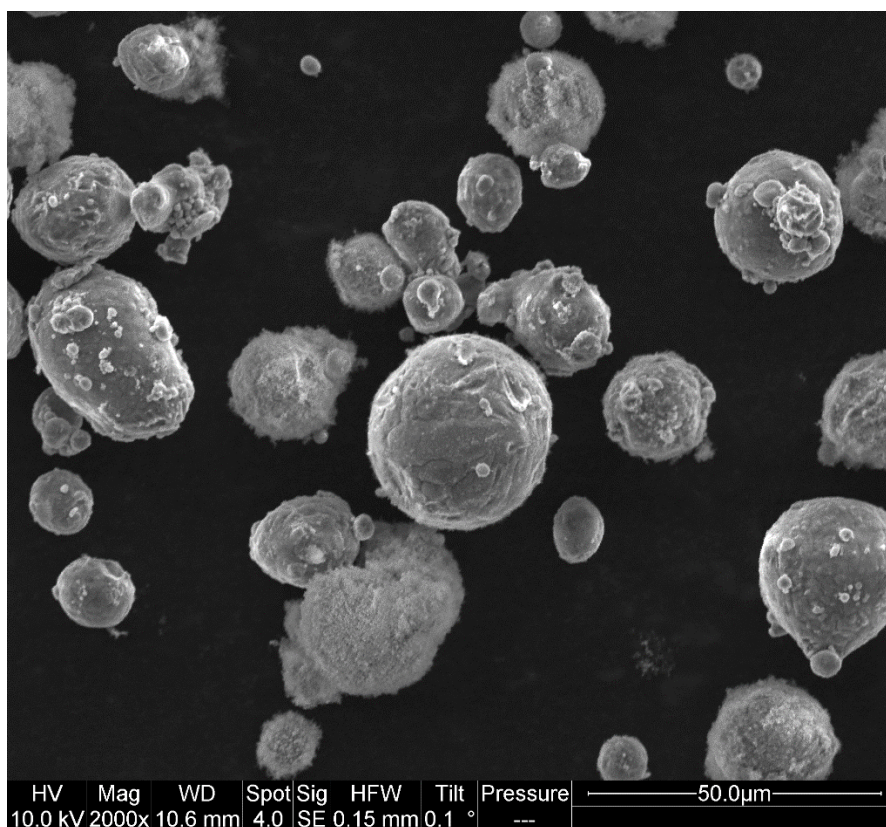


Figure 4-25. Close-up of Small Aluminum Particles Surface After Plasma 2000× Magnification.

The smaller single particles seemed to have a slightly different surface than the original aluminum powder. The plasma is effecting the particles even if they are not completely melted.

High Velocity Feed System Combustion Tests

Once the argon plasma, argon plasma entrained with steam, and plasma and aluminum particle interaction were understood, a full combustion test was attempted. There were no changes to the flow fields, since the carrier gas without particles was already used in the previous section. The particles reacted significantly more than previously when no oxidizer was present. Due to the nature of the formation and mass control, the pressure in the steam flow was high. When mixing, the aluminum carrier gas needed to be large enough to overcome this pressure. Tests were done to lower the carrier gas to reduce turbulence; however, the steam would backflow through the tubing and shear device if the flow was too small. Table 4-1 shows the combustion experiment parameters tested with the high velocity feeder. Experiments were performed by altering the microwave power and the aluminum mass flow. The goal of these tests was to understand how microwave power and aluminum mass flow react compared to each other.

Table 4-1. High Speed Feeder Combustion Tests

Combustion Test Number	Microwave Power (W)	Steam Mass Flow (g/s)	Aluminum Mass Flow (g/s)	Argon Plasma Flow (SLM)	Carrier Argon Gas (SLM)	Nitrogen Swirl (SLM)	Nitrogen Ejector Flow (SLM)	Boiler Pressure (psi)	Comments
2	1200	1.0	0.58	7.5	30	1.92	0	250	
3	500	1.0	0.58	7.5	30	1.92	0	300	
4	800	1.0	0.58	7.5	30	1.92	0	300	
5	600	1.0	0.58	7.5	30	1.92	0	300	
6	700	1.0	0.58	7.5	30	1.92	0	300	
7	600	1.0	0.58	7.5	30	1.92	0	300	
8	300	1.0	1.23	7.5	30	1.92	35	300	
9	400	1.0	1.23	7.5	30	1.92	0	300	
10	400	1.0	0.9	7.5	30	1.92	0	300	
11	—	—	—	—	—	—	—	—	Failed Test
12	400	1.0	0.9	7.5	30	1.92	0	300	
13	1100	1.0	0.58	7.5	30	1.92	0	300	
14	1100	1.0	0.58	7.5	30	1.92	0	350	
15	700	1.0	0.58	7.5	30	1.92	0	350	
16	1100	1.0	1.23	7.5	30	1.92	0	350	
17	1100	1.0	0.1	7.5	30	1.92	0	350	
18	700	1.0	1.23	7.5	30	1.92	0	350	
19	700	1.0	0.58	7.5	30	1.92	0	350	
20	700	1.0	0.1	7.5	30	1.92	0	350	
21	400	1.0	1.23	7.5	30	1.92	0	350	
22	400	1.0	0.58	7.5	30	1.92	0	350	
23	400	1.0	0.1	7.5	30	1.92	0	350	
24	400	1.0	0.58	7.5	30	1.92	0	350	
25	400	1.0	0.58	7.5	30	1.92	0	350	
26	400	1.0	0.9	7.5	30	1.92	0	350	
27	400	0.9	0.1	7.5	18	1.92	0	350	No Al flow
28	400	0.8	1.23	7.5	30	1.92	0	350	

In the beginning of the matrix, the system was being explored to find a stable working condition. Various power levels were tried to see the effect with all other properties constant.

Combustion Test 4 seen in Figure 4-26 demonstrates the reactivity of the aluminum–steam tests captured by the USB 3 camera. An H-Alpha filter (562–568 nm) was used to limit the amount of light captured by the camera. In the first frames, the plasma can be seen as well as the interaction with the first aluminum particles fed. In the 6th and 7th frames, a flame structure can be seen. The flame does not continue as it shifts to individual hot particles as seen in the last two frames.

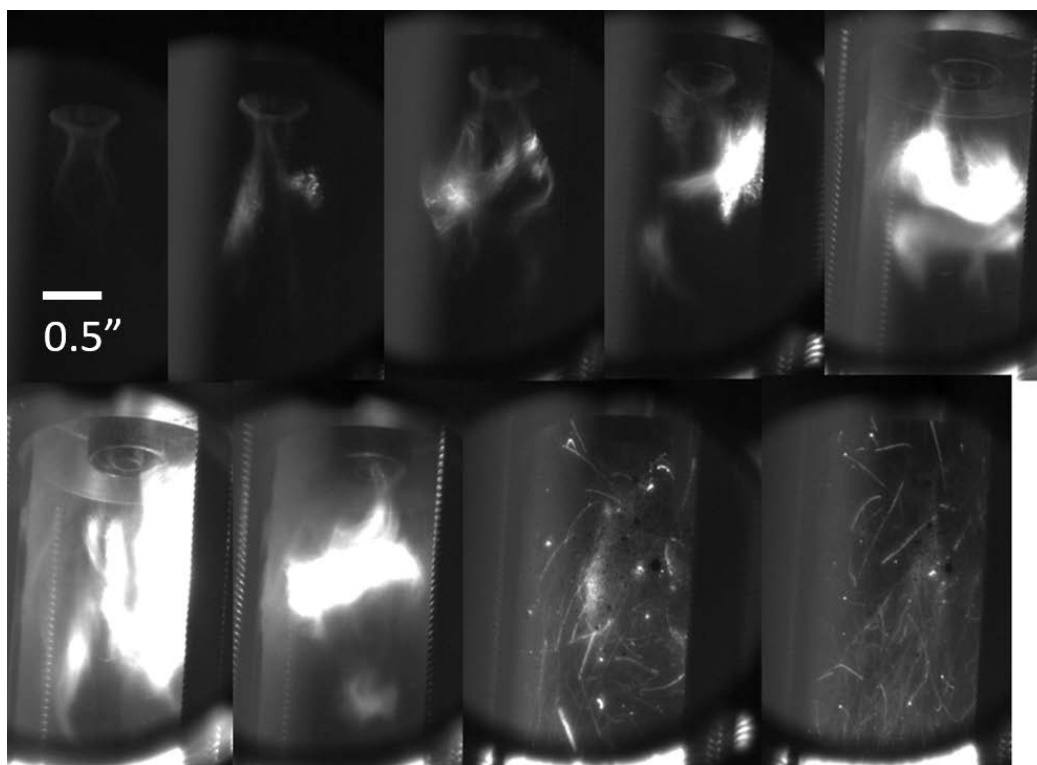


Figure 4-26. Combustion Test 4—H-Alpha Filter. The base plasma can be seen in the first frame. In the following frames, a flame can be seen to develop. In the last two frames, the flame disappears to a region of hot reacting particles. The test did not develop a consistent flame.

During Combustion Test 8, a pressure based ejector was used to try and divert some of the flow to slow down the main aluminum flow. While the flow was slowed, the pressure difference became too great and the steam began flowing back through the shearing device. Later in Combustion Test 27, the carrier gas flow was also decreased to observe the effect. The same steam backflow occurred and prevented aluminum flow. As tests went on, it was realized that the steam was coming in condensed and was absorbing a large amount of the microwave power. The

boiler pressure was increased from 200 psi to eventually 350 psi. 350 psi kept the steam in a reasonable quality range and fell safely within the boiler limits.

Once the system was determined to have a minimum carrier gas to balance the steam pressure and the boiler was increased to produce better quality steam, the tests were fairly consistent. A matrix was set up between Combustion Test 14 to Combustion Test 23, which varied power and the actuator feed. A 3×3 matrix was formed with 400 W, 700 W, and 1100 W tested at 0.1, 0.58, and 1.23 g/s feed rates. This allowed for an understanding of both varying power and change in system level equivalence ratio.

Sequences from two of the tests, Combustion Test 22 and Combustion Test 23, are shown respectively in Figure 4-27 and Figure 4-28. In Figure 4-27, the propagation of the aluminum–steam flame can be seen. The flame does not appear to have a specific direction as the turbulence and recirculation of the fluid flows dominate the mixing. Figure 4-28 also shows a flame propagation. It was observed in both figures that the reaction is transient and the flame does not always form at the injector tip.

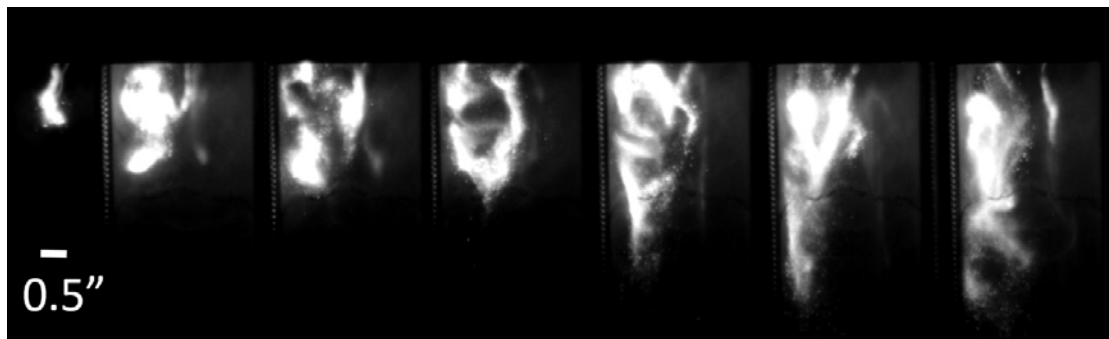


Figure 4-27. Combustion Test 22 Propagation of Aluminum–Steam Flame — 2.5 ms Between Each Frame. The progression of the flame region shows that the flame does not follow a specified constant location. The fluid flows are too high to generate a stable flame. Meaningful measurements were difficult to make with this configuration. To solve this, the low velocity pressure feeder was introduced.

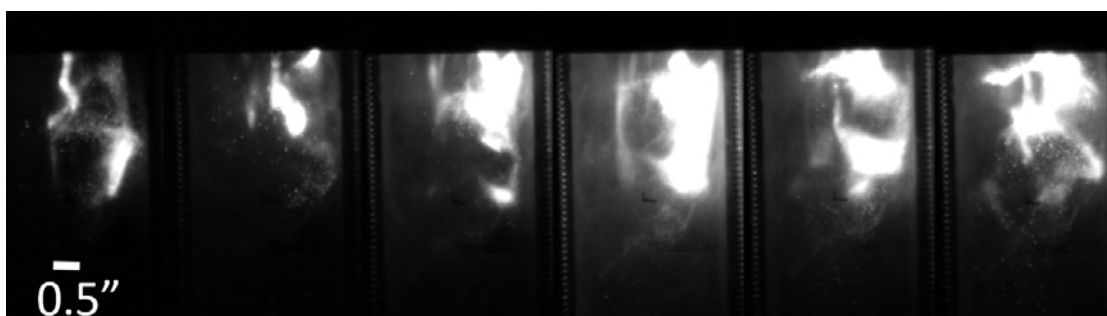


Figure 4-28. Combustion Test 23 Propagation of Aluminum–Steam Flame — 2.5 ms Between Each Frame. Another example of the inconsistent flame structure that prevented repeatable measurements from being made.

Although ignition of aluminum was achieved during these tests, it was very difficult to compare results from one test to the next due to the lack of a spatially consistent flame structure. Much of the combustion that was observed resulted from a buildup of aluminum and steam in the quartz tube igniting from the plasma filament. Mixing of the fuel and oxidizer before reaching the injector tip is typically favorable in most combustion systems; however, with the plasma, the frequency of aluminum particle and plasma filament collision was not as frequent as needed to ignite a majority of the aluminum. In this configuration, the plasma filaments formed on the outer tubing which did not intersect with the core flow. Only a few particles on the outer edge of the core flow reached the plasma filaments. Without a significant portion of aluminum particles interacting with the plasma filament, the majority of the power remained unreacted.

Combustion would only happen in waves after a few particles were ignited. Qualitatively, the matrix showed that more reactions occurred as the aluminum mass flow rate increased, which was determined visually by the larger reaction zones and less time in-between reactions. In addition, increasing the microwave power seemed to have little effect on the reaction at constant mass flow rates. For application basis and better data processing, the system was changed to attempt to alter the flame structure to be more spatially consistent by increasing the amount of plasma particle interaction.

Chapter 5

Results — Low Velocity Aluminum Feed

During the high velocity combustion experiments, it was observed that fluid dynamics in the quartz tube were complicated and hindered examining results. A new aluminum-powder feed system was used that did not rely on shearing, thus eliminating a large amount of argon and allowing for lower overall velocity in the system. The low velocity pressure feed system designed by the Applied Research Laboratory (ARL) was used to achieve lower flows. This system worked by creating a pressure differential across an orifice that regulated the mass flow.

Over the course of the tests, it was observed that the aluminum feed system had a minimum pressure limit needed for consistent aluminum feeding to occur. 20 psig was needed to achieve repeatable results. To calibrate the mass flow, the feeder was turned on and then 30-seconds worth of aluminum was measured in a water container. The difference in mass before and after was then calculated and time averaged. 20 psi was equivalent to approximately 0.92 g/s of aluminum. In the later tests, this mass flow was kept constant and the oxidizer flow was adjusted to change the system oxidizer to fuel ratio.

A non-premixed configuration was used so that the argon plasma would form on the inner tubing so that the filaments would interact with a greater amount of aluminum powder. The locations of the flow and schematic of the injector are shown below in Figure 5.1.

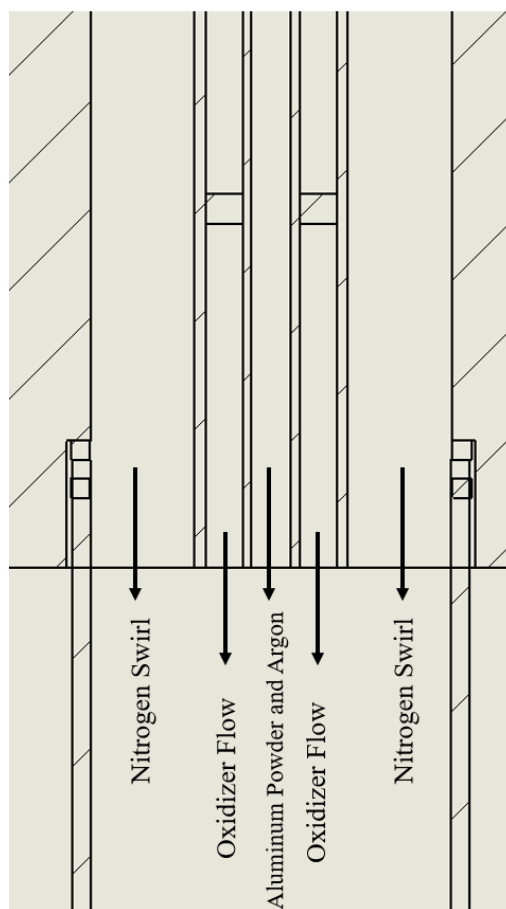


Figure 5-1. Non-premixed Flow Configuration Used with Low Velocity Aluminum Feeder. With the switch to the low velocity particle feeder, the flows were rearranged. The nitrogen flow remained on the wall of the quartz tube. The oxidizer flow was moved to the annulus. The aluminum powder and argon for creating a plasma were in the core flow. Having the plasma on the inner tubing increased the aluminum-plasma collisions.

Table 5-1 shows the experiments performed with the low velocity aluminum feeder in the configuration detailed in Figure 5-1. The table shows the microwave power used, oxidizer flow rates, aluminum and gas flow rates and equivalence ratios for each experiment.

Table 5-1. Low Velocity Feeder Combustion Test Matrix

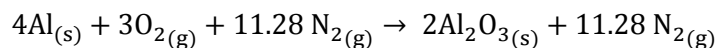
Test Name	Microwave Power (W)	Air (SLM)	Steam Mass Flow Rate (g/s)	CO2 Volumetric Flow Rate (SLM)	Feeder Pressure (psi)	Argon Plasma Flow (SLM)	Nitrogen Swirl (SLM)	Equivalence Ratio
Combustion Test 1	600	0	1	0	20	5	0	0.35
Combustion Test 2	600	0	1.2	0	20	5	0	0.3
Combustion Test 3	500	0	1.3	0	20	1.92	0	0.3
Combustion Test 4	400	10	0	0	20	5	0	3.4
Combustion Test 17	200	21.5	0	0	20	0.71	3	1.7
Combustion Test 18	200	14.3	0	0	20	0.71	3	2.5
Combustion Test 19	200	28.6	0	0	20	0.71	3	1.3
Combustion Test 20	200	35.9	0	0	20	0.71	5	1.0
Combustion Test 21	200	10.77	0	0	20	0.71	5	3.3
Combustion Test 22	200	35.9	0	0	20	0.71	5	1.0
Combustion Test 23	200	14.4	0	0	20	0.71	10	2.5
Combustion Test 24	200	21.5	0	0	20	0.71	10	1.7
Combustion Test 25	200	28.7	0	0	20	0.71	10	1.3
Combustion Test 26	200	35.9	0	0	20	0.71	10	1.0
Premixed 1	250	5	0	0	20	5	0	7.3
Premixed 2	250	25	0	0	20	5	0	1.4
Premixed 3	250	40	0	0	20	5	0	0.9
Combustion Test 27	200	30	0	0	20	1	7	1.2
Combustion Test 28	200	30	0	0	20	0.5	7	1.2
Combustion Test 29	200	40	0	0	20	0.6	7	0.9
Combustion Test 30	200	40	0	0	20	0.6	7	0.9
Combustion Test 31	200	40	0	0	20	0.6	7	0.9
Combustion Test 32	200	40	0	0	20	0.6	7	0.9
Combustion Test 33	200	40	0	0	20	0.6	7	0.9
Combustion Test 34	200	40	0	0	20	0.6	7	0.9
Combustion Test 35	200	40	0	0	20	0.6	7	0.9
Combustion Test 36	300	0	0	20	20	0.6	7	3.4
Combustion Test 37	300	0	0	31	20	0.6	7	2.2
Combustion Test 38	200	60	0	0	20	0.6	7	0.6
Combustion Test 39	200	40	0	0	20	0.6	7	0.9
Combustion Test 40	200	20	0	0	20	0.6	7	1.6
Combustion Test 41	200	60	0	0	20	0.6	7	0.6

The equivalence ratio (ϕ) was calculated by converting both the aluminum and oxidizer flow into moles. An example of Combustion Test 35 is shown below:

$$0.92 \frac{\text{g}}{\text{s}} \text{ of Al} \times \frac{1 \text{ mol}}{27 \text{ g}} \rightarrow 0.034 \frac{\text{mol}}{\text{s}} \text{ of Al}$$

$$40 \frac{\text{L}}{\text{min}} \times \frac{1 \text{ min}}{60 \text{ s}} \times 0.001 \frac{\text{m}^3}{\text{L}} \rightarrow 0.0006 \frac{\text{m}^3}{\text{s}}$$

$$0.0006 \frac{\text{m}^3}{\text{s}} \times 1.225 \frac{\text{kg}}{\text{m}^3} \times 1000 \frac{\text{g}}{\text{kg}} \times \frac{1}{28.97} \frac{\text{mol}}{\text{g}} \rightarrow 0.0282 \frac{\text{mol}}{\text{s}} \text{ of air}$$



$$0.034 \frac{\text{mol}}{\text{s}} \text{ of Al} \div 4 \rightarrow 0.0085$$

$$0.0282 \frac{\text{mol}}{\text{s}} \text{ of air} \div 3 \rightarrow 0.0094$$

$$\phi = \frac{0.0085}{0.0094} \rightarrow 0.9$$

Aluminum Through Argon Plasma — Low Velocity Feeder

In the new low flow configuration, aluminum particles were passed through an argon plasma with no oxidizer to compare to previous configurations. In the previous configuration, the particles would give off a blue light and simply quench due to the high amount of diluent. In the new configuration, the particles remained condensed and reacted with oxygen at the bottom of the quartz tube. The flame would then propagate back up through the tube and ignite particles upstream, shown in Figure 5-2. These results further confirmed that the plasma filament interaction results in cracking of the aluminum oxide shell and exposes the raw aluminum which can react with an oxidizer.

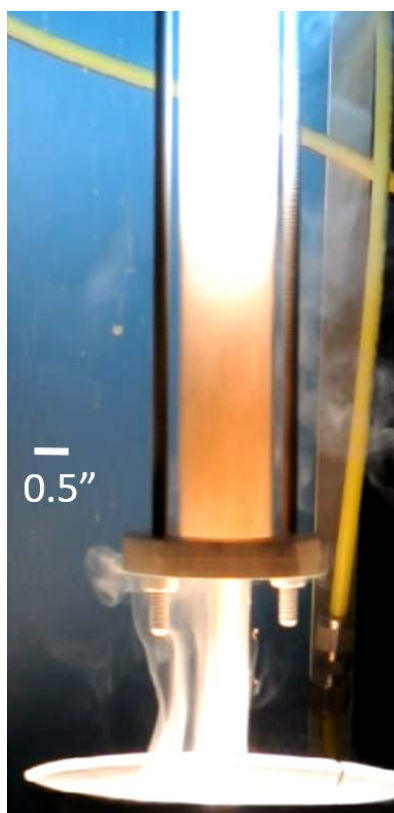


Figure 5-2. Aluminum Passing Through an Argon Plasma and Reacting with Surrounding Air. With the low velocity particle feeder, there was far less diluent. Therefore, the particles could react with the atmospheric air that was in the quartz tube and at the exit. After observing these results, it was suggested to try air as an oxidizer as opposed to steam.

Aluminum—Steam — Low Velocity Feeder

Originally, steam was used as the oxidizer and tests were performed to compare to the previous high velocity carrier gas tests. The flows were altered to have the steam flow through the annulus region and argon plus aluminum powder flowing through the inner tube. To achieve a plasma with this configuration, the steam and argon were turned on and then the microwave power was turned up until argon filaments appeared on the inner tubing.

The first test with steam was successful and produced a continuous flame, shown in Figure 5-3. The plasma filaments can be seen at the injector tip leading to the attached region of

combustion. Reaction continued for approximately 15 seconds before the system was shut down. The following tests attempted to mimic the result from the first test; however, ignition with a large anchored flame only occurred twice out of a dozen tests.

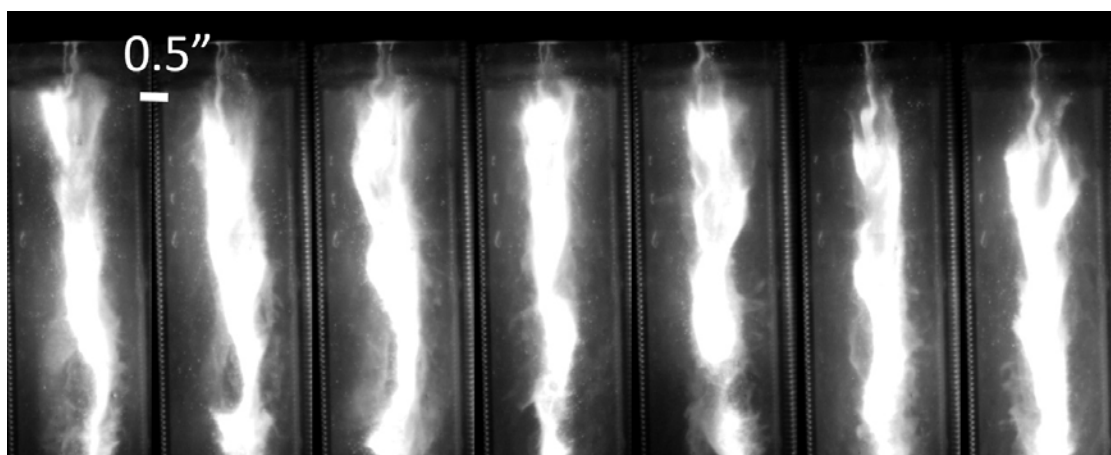


Figure 5-3. Combustion Test 29 — Aluminum—Steam Continuous Flame — 2.5 ms Between Frames. A consisted aluminum-steam flame was achieved. The filaments are visible at the top of the frames. The flame region was fairly consistent throughout this test. These results were not repeatable due to a difference in the structure of the plasma filaments.

While only repeated once, Combustion Test 29 showed that it is possible to ignite aluminum–steam mixtures in the low velocity configuration. It should be noted that the plasma structure is clearly visible at the injector tip in Figure 5-3.

During the testing process, the molybdenum inner tubing was damaged. It was replaced with stainless steel due to availability and convenience. Tests were performed at conditions that mimicked the known working state. The tests resulted in little to no reaction of the aluminum.

Several tests were performed to determine whether the conditions deviated from what was expected, or if there was a hardware issue. It is hypothesized that these steam filaments absorbed a majority of the microwave power. Without this power directed in the aluminum particles, there was not enough energy to initiate the reaction.

The following set of tests, shown in Table 5-2, were an attempt to recreate the aluminum–steam seen in Combustion Test 29. Various powers, aluminum feed rates and steam flows were attempted to test a wide range of conditions to find an operable condition. Changes in the microwave power and aluminum flow were made to alter the plasma structure and the fuel to oxidizer ratio.

Table 5-2- Various Low Velocity Feed Steam Tests

Test Name	Power (W)	Aluminum Feeder Pressure (psi)	Steam Mass Flow (g/s)	Nitrogen Swirl
Combustion Test 5 Attempt 1	500	10	1.3	Off
Combustion Test 5 Attempt 2	500	10	1.3	Off
Combustion Test 5 Attempt 3	700	10	1.3	Off
Combustion Test 5 Attempt 4	700	10	1.3	Off
Combustion Test 5 Attempt 5	700	15	1.3	Off
Combustion Test 5 Attempt 6	700	20	1.3	Off
Combustion Test 6 Attempt 1	600	5	1.3	Off
Combustion Test 6 Attempt 2	600	30	1.5	Off
Combustion Test 6 Attempt 3	1100	30	1.5	Off
Combustion Test 6 Attempt 4	1100	10	1.5	Off
Combustion Test 6 Attempt 5	1100	10	1.5	On
Combustion Test 6 Attempt 6	400	10	1.0	On
Combustion Test 6 Attempt 7	1100	10	1.0	On
Combustion Test 6 Attempt 8	400	10	0	On
Combustion Test 6 Attempt 9	400	10	0	On
Combustion Test 7 Attempt 1	1100	10	1.5	Off
Combustion Test 7 Attempt 2	500	20	1.5	Off
Combustion Test 7 Attempt 3	600	20	2.0	Off
Combustion Test 7 Attempt 4	400	20	0	Off

Most of the steam tests looked like either Figure 5-4 or Figure 5-5. At lower powers (<700 W), the results looked like Combustion Test 5 Attempt 4, in which the aluminum stream simply passed through the plasma with minimal reaction and looked like a jet. At higher powers (>700 W), there was significant reaction at the top of the burner. From looking at the high speed and colored videos, the reaction was not combustion related, rather it was the stainless steel outer

tubing melting and being damaged. Spectroscopy shown in Figure 5-6 confirmed that the stainless steel was reacting by the large amount of ridges caused by the various metallic elements in stainless steel.

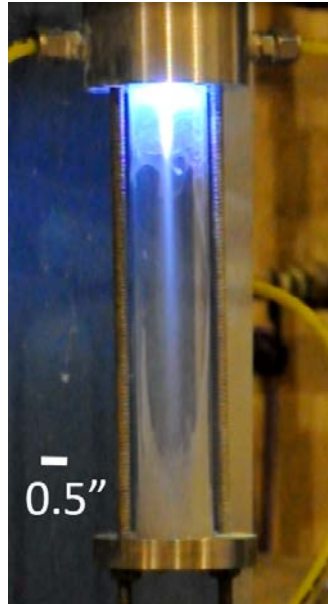


Figure 5-4. Combustion Test 5 Attempt 4. Aluminum passed through the argon-steam plasma with little reaction. Upon further observation, it was seen that the plasma had small steam filaments forming in the annulus. These filaments were taking power from the argon filaments, limiting the reaction that could take place.



Figure 5-5. Combustion Test 6 Attempt 4. Once microwave power was raised to over 700W, the plasma became unstable and began to cut and react with the metal in the injector.

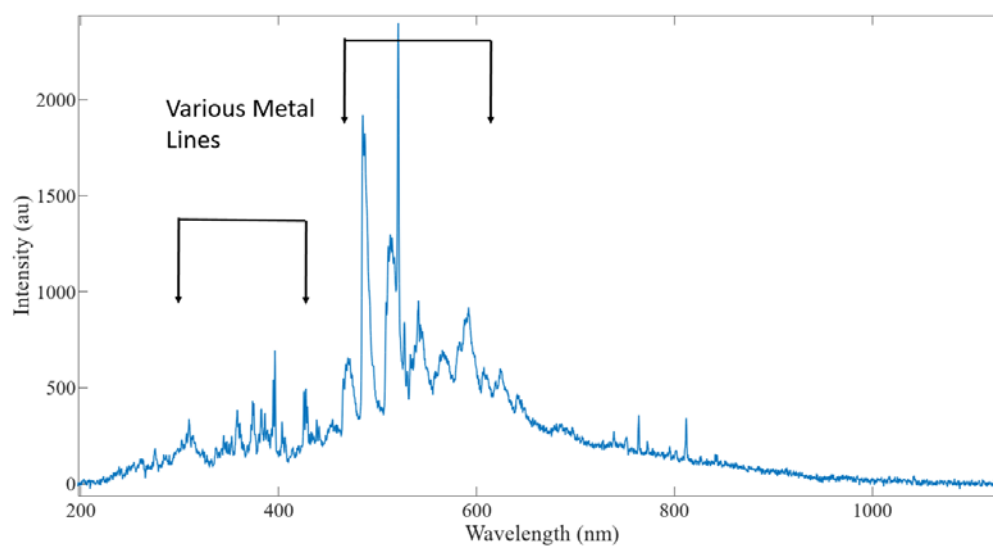


Figure 5-6. Combustion Test 6 Attempt 4 Spectra Showing Tubing Reactions. Spectra was taken during the reaction that was damaging the injector. Various metal lines from the stainless steel were seen.

During these tests, the stainless steel outer tubing was damaged. The next test, the plasma had a different structure. In a non-damaged tube, the filaments occurred on the inner tubing and also had several filaments interact with the steam in the annulus. The damaged edge of the tube altered the microwave coupling and the plasma. With a damaged tubing, shown in Figure 5-7, only argon filaments formed and the small steam filaments in the annulus disappeared. Once the steam filaments were gone, the following test achieved a consistent flame similar to Combustion Test 29. It was difficult to maintain this success as it depended on a specific deformation, and the plasma began to continue to damage the tubing beyond being useful. Although a stable configuration was not achieved, these experimentations showed it was possible to have an aluminum–steam flame structure as well as the importance of the plasma structure in ignition of the particles.



Figure 5-7. Damaged Stainless Steel Tubing from a Stagnant Plasma Filament. Once the injector was damaged, it altered the plasma structure due to the lack of symmetry.

Aluminum–Air Combustion Tests

After observing that the large reaction produced by the aluminum's interaction with the surrounding atmospheric air, it was decided to use air as the oxidizer flow. Air, unlike steam, does not have the problem of condensing at atmospheric conditions. To obtain an argon plasma with air as an oxidizer, the argon plasma gas, air, and nitrogen swirl flows were all turned on. Microwave power was turned up to 400 W, the minimum amount for plasma ignition. At this power level, there is an observed breakdown in the annulus of the nitrogen in the air and an argon plasma on the inner tube. To achieve just an argon plasma, the microwave power is lowered to 200 W. At 200 W, the argon plasma only consists of filaments on the inner tube and did not have any in the annulus region as seen to be a problem with steam.

It was immediately seen from the first tests that the aluminum–air mixture reacted more intensely than aluminum–steam. Combustion Tests 17 and 18 (21.5 SLM and 14.3 SLM of air, respectively) showed ignition, but burned in more of a stream-like fashion. The stream seemed to look like an extension of the plasma filaments at the injector tip, and slowly widened as the particles traveled down the quartz tube. In Combustion Tests 19 and 20, the air flow was increased to 28.6 and 35.9 SLM. Due to what is known about coaxial jets, the increase in oxidizer had a large effect on the mixing of the flows because of the large velocity mismatch caused between the annular flow and core flow. Combustion Tests 21 to 24 were tested with the exit of the quartz tube submerged in the exhaust water to collect the products more effectively. Pressure would build up during these tests and result in a pulsing burning due to aluminum and air building up in the tube and then a flame propagating through. It was found that at least 0.25" must be left from the bottom of the quartz to the collection bucket to achieve constant repeatable results.

Combustion Tests 27–33 increased the air flow to 30 and 40 SLM. During tests with 40 SLM air, a recirculation zone of particles was visible on the high-speed camera. Particles were seen circulating in the region between the injector tip and the bottom of the bottom plate.

During ignition, as seen Figure 5-8, the flame originally looks like an extension of the plasma filaments. Due to velocity differences of the annulus and center flow, large mixing occurs early in the flow allowing the flame to sit just off of the injector tip. Since it is a diffusion flame, the reaction continues as the mixing increases. For two coaxial jets, the width of the stream continues to grow the farther away from the jet source, which results in better mixing. Reaction can be seen to increase at the tip of the reactants as they move downward in Figure 5-9.

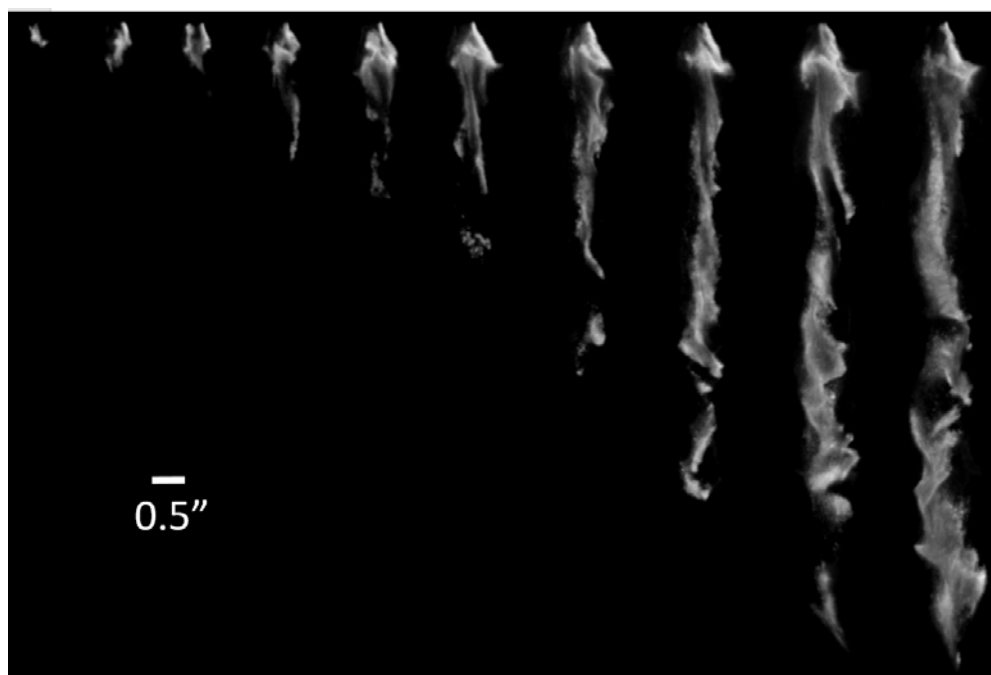


Figure 5-8. Ignition Sequence of Aluminum–Air Flame — Combustion Test 34 — 2.5 ms Between Frames. During ignition of aluminum-air, the flame begins to widen as it travels down the quartz tube due to increases to mixing. The top of the flame near the injector tip reaches steady state quickly, most likely due to the plasma.

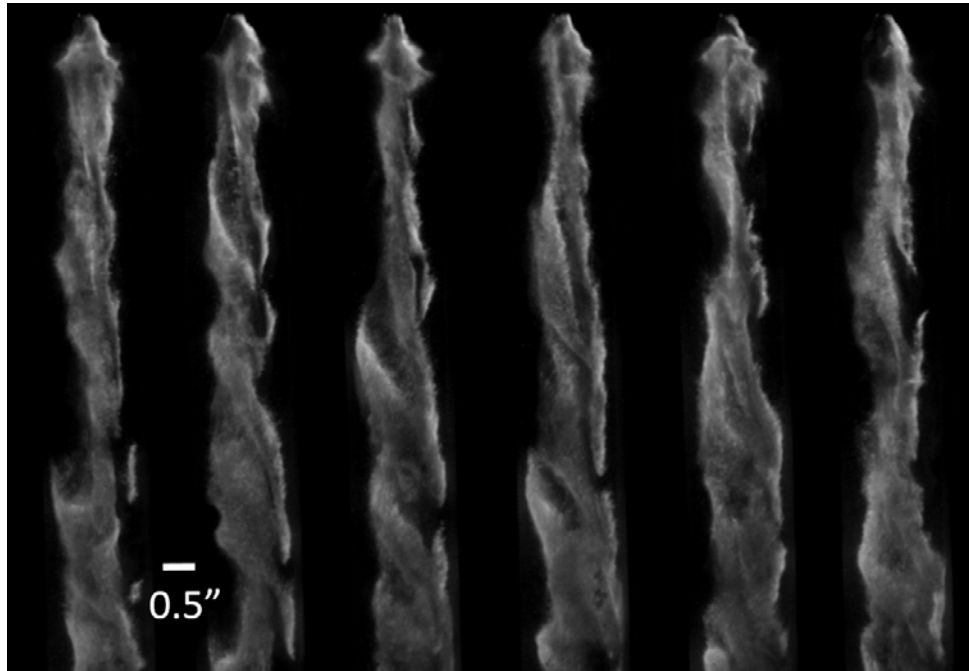


Figure 5-9. Steady State Aluminum–Air Flame — Combustion Test 34 — 2.5 ms Between Frames. Once the aluminum-air flame reached steady state, the flame was geometrically consistent. Besides the swirl that was purposely introduced, the flame was much more stable than the previous experiments with the high velocity feeder.

The time to reach steady-state during experiments was short, on the order of tenths of a second. Once at steady-state, the flame can be seen to have the swirl structure provided to the oxidizer by the angled holes in the spacer. Spatially, the flame is consistent and did not flare from the expected path. After experiments, there would be a slight layer of aluminum oxide on the quartz tube, but not as much as with the high velocity feeder which would constantly deposit on the walls.

Effect of Stoichiometry

Due to the nature of metal combustion and the diffusion flame that develops, the local stoichiometry will vary throughout the combustion volume. Therefore, the overall system stoichiometry will be documented. Earlier in the aluminum—steam tests, it was observed that

more aluminum, even fuel rich, reacted more than similar lean tests. Once the aluminum feeder was switched to the low velocity feeder, it was determined that 0.92 g/s of aluminum was the minimum amount to maintain repeatable and reliable flow. Since this was a relatively high amount of fuel for the size of the burner, the oxidizer flow was adjusted as opposed to increasing the aluminum mass flow. One drawback to this is that the velocity of the oxidizer changed and may have affected the mixing and residence times of particles. The residence time is the amount of time that the particle remains surrounded by an oxidizing environment. The longer the time, the more of the reaction will occur.

In the aluminum–air configuration, the stoichiometry was varied to determine the usable range for a potential igniter. The three equivalence ratios (ϕ), 1.6, 0.9, and 0.6, were tested. The aluminum feeder did not work well in ranges below 0.92 g/s; therefore, the air flow was varied to change the equivalence ration. At fuel lean and near stoichiometric conditions, $\phi = 0.6$ and $\phi = 0.9$, the aluminum ignited and attached to the injector tip. These conditions are shown respectively in Figure 5-10 and Figure 5-11. At fuel rich conditions, $\phi = 1.6$, the aluminum still ignited; however, it formed a thin stream that did not expand to a more flame like structure until farther down in the quartz tube, seen in Figure 5-12. These conditions did not seem suitable for any sort of application

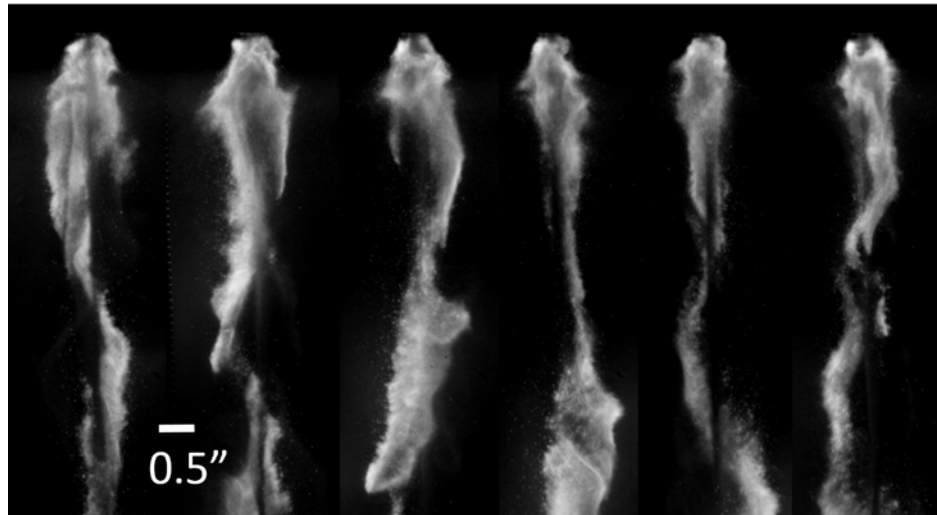


Figure 5-10. Combustion Test 38 — $\phi = 0.6$ — 2.5 ms Between Frames. In the lean case, the aluminum-air flame had a stable attached flame at the injector tip. In this experiment and other that were fuel lean, the flame ended before the bottom of the quartz tube due to lack of oxidizer to continue burning.

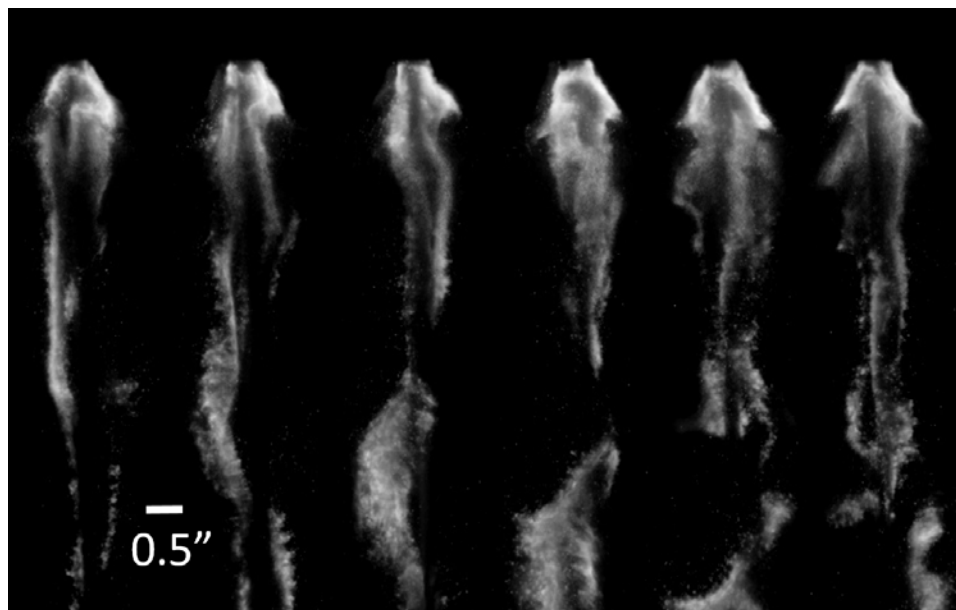


Figure 5-11. Combustion Test 35 — $\phi = 0.9$ — 2.5 ms Between Frames. For the near stoichiometric aluminum-air flame, the flame attached at the injector tip and continued to react the entire length of the quartz tube.

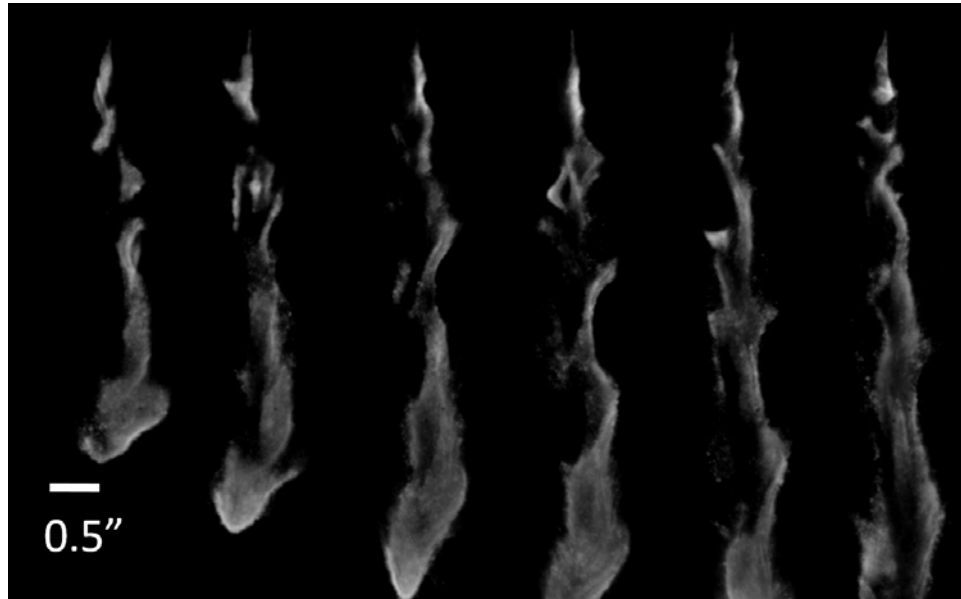


Figure 5-12. Combustion Test 40 — $\phi = 1.6$ — 2.5 ms Between Frames. Unlike the other two equivalence ratios, the fuel rich case did not have an attached flame at the injector tip. The flame relied significantly on the mixing as the mixture traveled down the quartz tube. The flame reaches its full width at the bottom of the figure.

The experiments at $\phi = 0.9$ provided significantly better results shown in Figure 5-13.

The flame structure was seated at the injector tip and the flame was long and consistent throughout the test.

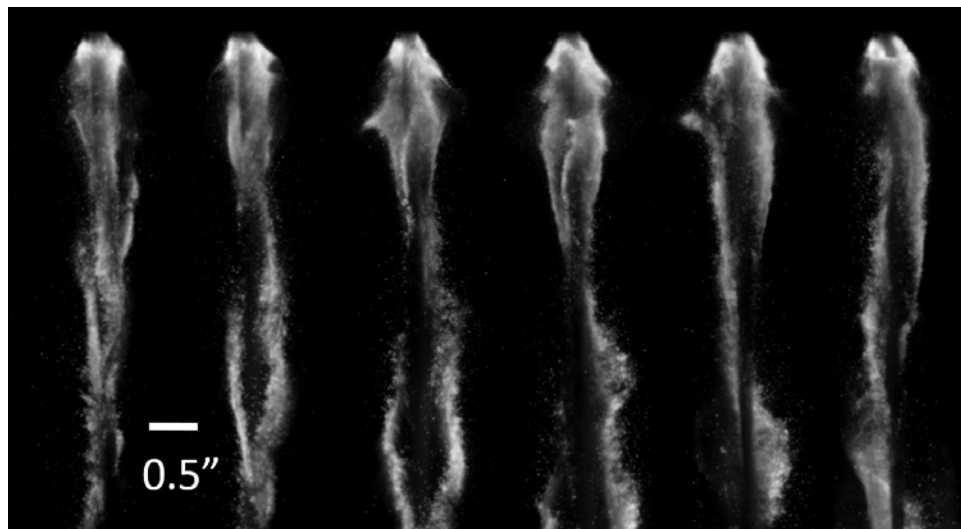


Figure 5-13. Combustion Test 39 — $\phi = 0.9$ — 2.5 ms Between Frames. Again the near stoichiometric flame is seated throughout the entire experiment.

At lean conditions of $\phi = 0.6$, the flame significantly shortens compared to the fuel rich conditions shown in Figure 5-14. Due to the lean conditions, the particles are able to burn completely due to the large amount of oxygen present compared to the previous two conditions.

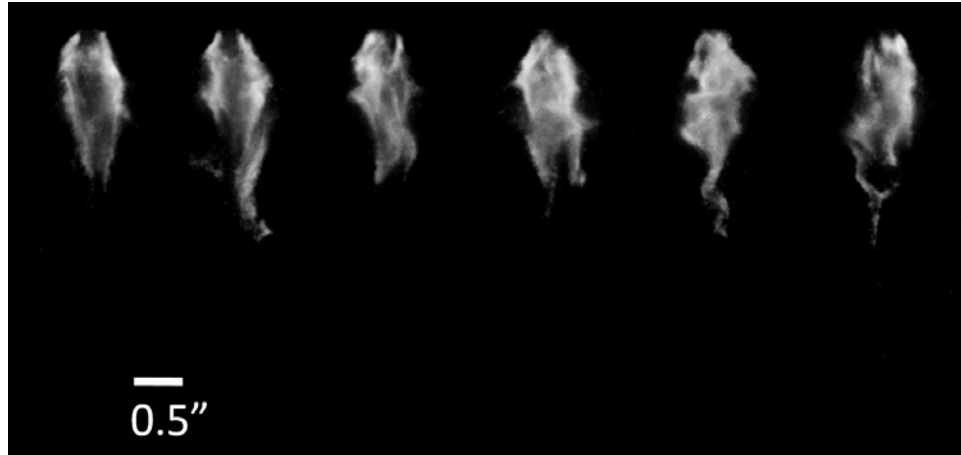


Figure 5-14. Combustion Test 39 — $\phi = 0.6$ — 2.5 ms Between Frames. The fuel lean flame is significantly shorter than the near stoichiometric flame. The lean case is completely attached to the injector tip. The shortness of the flame is likely due to the lack of oxidizer to continue burning the particles completely.

Comparing the different equivalence ratios, 0.9 was the best in terms of use for an application. The long stream of reacting particles would be easier to merge and ignite into another flow. It also has good stability at the injector tip and maintained a relatively consistent flame geometry which are favorable designs.

Premix Configuration

During the aluminum–air tests, the idea of premixing the fuel and oxidizer to increase burning was considered. It was thought that premixing the fuel and oxidizer would increase mixing and thus combustion. The air-and-aluminum mixture was routed through the inner tube of the burner. The argon gas was switched to the annulus region. A plasma easily formed on the outer tubing of the burner. Approximately 3 or 4 filaments formed, but were far less optically

dense than the filaments in the non-premixed configuration. During the test, fuel and oxidizer would fill the quartz tube and eventually a flame would propagate throughout the tube. There was no consistent flame. These tests further indicate that the interaction between the plasma filaments and the aluminum particles is the initiation reaction for combustion. Since the filaments were more spread out in the premixed case, far fewer initiation mechanisms occurred allowing for the observed behavior.

Figure 5-15 shows the propagation of built up aluminum and air in the quartz tube. After the propagation completed, there would be a period of no reaction similar to the first frame until more of the mixture built up again, or until enough particles reacted with the plasma to ignite other particles.

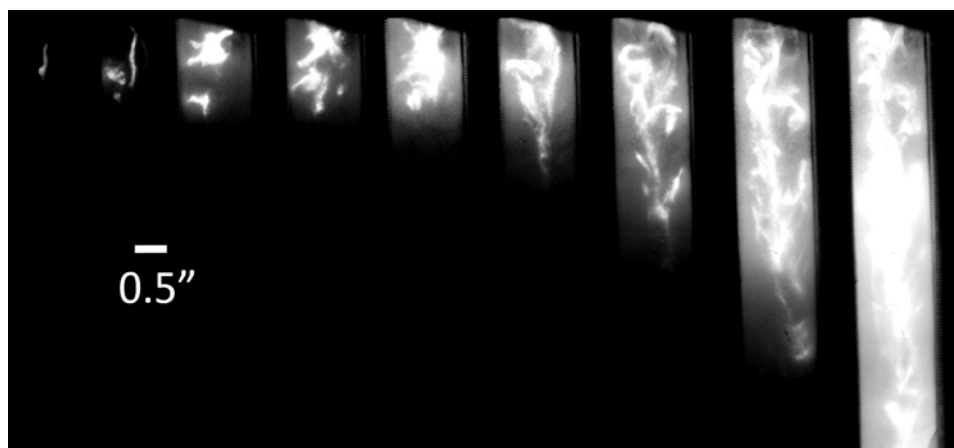


Figure 5-15. Propagation of Premixed Aluminum — Air Flame Showing Shock Tube-Like Propagation — Premixed 3 — 2.5 ms Between Frames. Premixing the aluminum and air was attempted to increase combustion. With the plasma on the outer tubing, the aluminum particles did not contact the plasma filaments as frequently. This resulted in periods of reactivity and periods of little reactivity. No reactivity would happen until a few particles interact with the filament setting off a propagation down the quartz tube.

Aluminum-CO₂ Combustion Tests

The oxidizer was switched to CO₂ to compare to the steam and air cases. CO₂ had the advantage over steam in that there was no condensation; however, the oxygen molecules were

attached to the carbon and needed energy to be broken. CO_2 is typically more difficult to use than air, but easier than air. CO_2 also can be stored in liquid form making it a useful oxidizer to study for potential applications. Figure 5-16 shows the progression of an aluminum- CO_2 flame with $\phi = 2.2$.

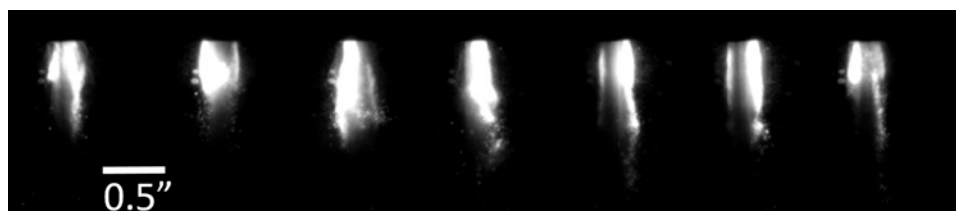


Figure 5-16. Aluminum- CO_2 Flame — Combustion Test 37 — $\phi=2.2$ — 2.5 ms Between Frames. The aluminum- CO_2 experiments only tested fuel rich cases due to equipment restraints. Surprisingly, the flame attached to the injector tip unlike the fuel rich aluminum-air flame. The luminous flame region was much smaller than when air was the oxidizer. This is likely due to the difficulty to extract the oxygen from CO_2 .

Successful ignition was achieved with the aluminum- CO_2 mixture. The flame structure itself was small compared to that seen with other oxidizers.

Particle Temperature Fitting

To quantify the combustion seen in the variety of tests, the broadband emission recorded with the spectrometer was fit to determine a temperature from Planck's Law (Equation 35). Since the spectrometer's raw data was non-linear with respect to wavelength, a calibration was needed. Non-linearity existed due to various optics, prisms and detector transmission curves. The spectrometer was set up with a fiber optics cable and a collimating lens and directed at a tungsten lamp. The current from the power supply was calculated by measuring the voltage over a precision resistor. Calibration of the lamp was provided by the manufacturer and complied with NIST standards. Further procedure is provided in Appendix D. For the needs of this experiment, the lamp was set to 2273 K, which was as high as the power supply connected to the lamp would

produce. In addition, calibration of the lamp should be as close as possible to the temperatures seen in the experiments. The current was matched to temperature calibration provided with the lamp. Aligned and powered to the correct temperature, a baseline spectrum was recorded. This would be our baseline for a known blackbody emission at 2273 K. Planck's Law, Equation 12, was solved for intensity, where C_1 and C_2 are defined by Equation 13 and 14. Solving for intensity yields:

$$i_{\lambda,T} = \frac{\varepsilon C_1}{\lambda^5} \cdot \frac{1}{e^{\frac{C_2}{\lambda T}} - 1}. \quad (39)$$

The spectral fitting was appropriate over the wavelengths of 550–900 nm as stated in the literature. The known function of emissivity with respect to wavelength, known temperature of the tungsten lamp, and constant were used to solve for the black-body intensity over the range of wavelengths. This represents what was emitted from the calibration lamp. The calculated theoretical intensity was then divided by the values actually recorded from the spectrometer focused on the tungsten filament lamp. The ratio of these two values is the correction factor due to the non-linearity of the spectrometer, which could then be used to correct future spectra. Once corrected, Equation 16 was used to plot $1/\lambda$ on the x-axis and $\ln(i_{\lambda,T} \times \lambda^{6.4})$. The temperature was then found by dividing the constants by the slope of the line.

The flames being fit in this work were all approximately 0.5 inches wide. The optical depth was found to be within the $\lambda^{-1.4}$ approximation due to being optically thin.

In the code used for temperature fitting, multiple text files collected from the spectrometer were used as inputs. A sample code is shown in Appendix C. The intensity-vs.-wavelength was plotted in Figure 5-17 to examine if the spectra contained a thermal profile sufficient for fitting. Spectra that contained various argon plasma lines, or significant noise-to-signal ratio were not used. As explained above, the code was trimmed to the 550–900 nm, which is the range over which an accurate fit can be applied. Equation 19 was then plotted over the

range of wavelengths to achieve a slope proportional to $1/T$. Figure 5-19 and similar plots can be examined to see how well the fit slope matches the experimental results. Finally, the temperatures of each input were plotted, shown in Figure 5-20. The x-axis of Figure 5-20 shows consecutive spectra inputs taken. Figure 5-18 shows the result of a corrected spectra for non-linearity. Table 5-3 and Table 5-4 show the temperatures for various combustion tests.

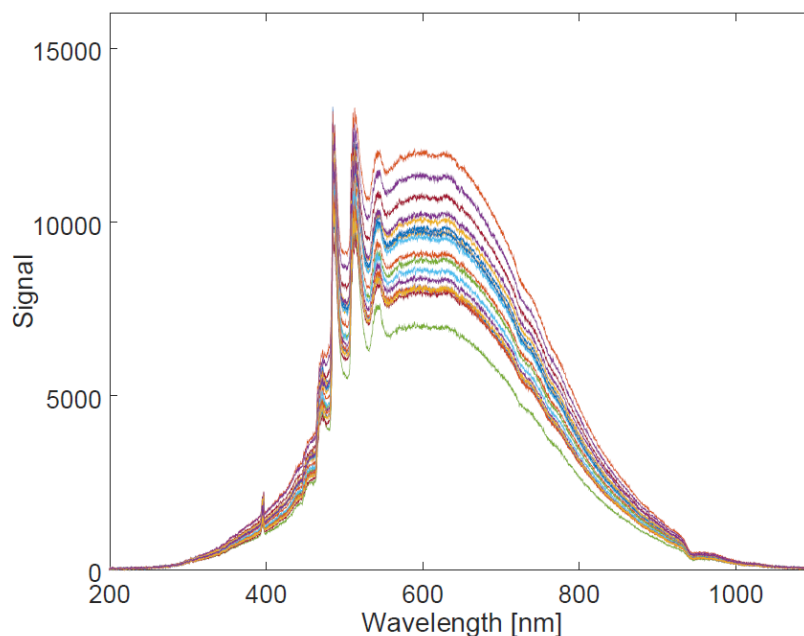


Figure 5-17. Example of Collected Raw Spectra — Combustion Test 35. Spectra were collected during combustion experiments with 5 ms integration time. In the low velocity configuration, there was little change from spectra to spectra since it was geometrically consistent.

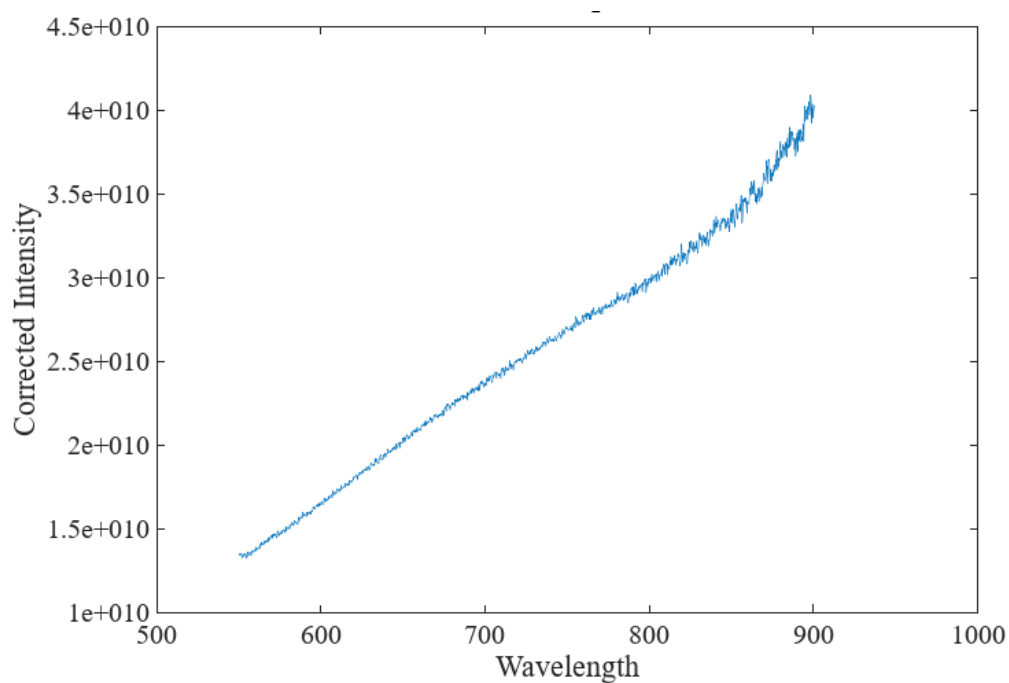


Figure 5-18. Corrected Singular Spectra for Non-linearity — Combustion Test 35. Appendix C and D were used to correct the non-linearity in the spectrometer. Correcting for this non-linearity significantly changes the particle temperature fitting.

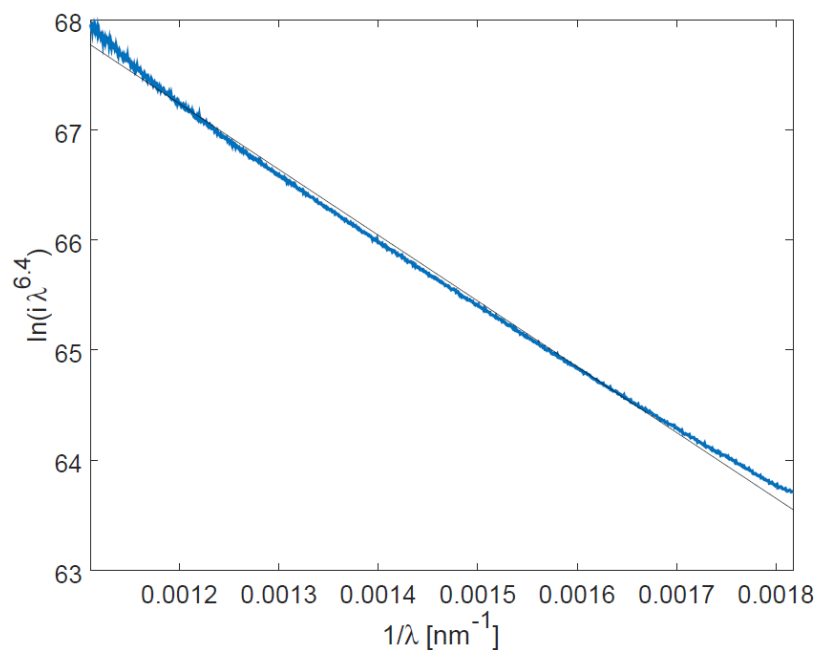


Figure 5-19. Thermal Emission Fitting of Equation. Planck's Law is plotted to solve for the slope, which can be converted into temperature. Accuracy of the fitting can also be checked. This figure shows a linear results with a little error at the ends. On poor fits, the plot does not resemble anything linear.

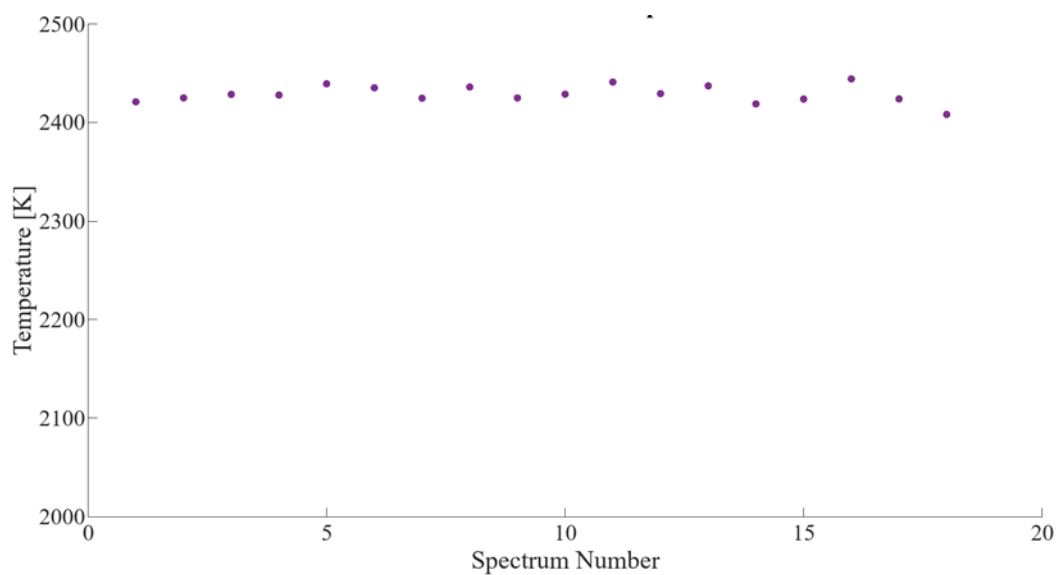


Figure 5-20. Temperature Output for Each Spectra — Combustion Test 35. For each particle temperature fit, a plot is generated with the temperatures and which spectra file was fit. This allows for observations of temperature change with time.

Table 5-3. High Speed Feeder Aluminum – Steam Test's Average Temperature

Test Name	Average Temperature (K)
Combustion Test 2	2159.6
Combustion Test 3	2009.6
Combustion Test 4	2554.1
Combustion Test 5	2453.4
Combustion Test 6	2093.3
Combustion Test 9	2419.3
Combustion Test 10	2163.5
Combustion Test 14	2348.4
Combustion Test 15	2251.4
Combustion Test 20	2351.1
Combustion Test 21	2209.2
Combustion Test 22	2347.9
Combustion Test 24	2317.9
Combustion Test 25	2120.4
Combustion Test 26	2213.1

Table 5-4. Low Velocity Feeder Test's Average Temperature (Kelvin)

Combustion Test 17	2365.2
Combustion Test 22	2173.0
Combustion Test 23	2248.8
Combustion Test 24	2266.3
Combustion Test 25	2303.2
Combustion Test 26	2290.4
Combustion Test 34	2438.0
Combustion Test 35	2422.2
Combustion Test 36	2414.0
Combustion Test 37	N/A
Combustion Test 38	2280.6
Combustion Test 39	2485.9
Combustion Test 40	2477.2
Combustion Test 41	2443.1

Across all of the experiments, there is little variation in the temperature measured. All values are between 2000 and 2500 K, with the vast majority between 2250–2450 K. These values match well with the burning temperature of the particles reported in the literature. Experiments that have temperatures closer to 2000 K with aluminum–steam reaction may have had water condense on hot particles cooling them down. In the aluminum–air experiments, the low temperatures occur around Combustion Tests 22–24, which was during submission of the exhaust in water. These experiments contained propagation of a flame, much like a shock tube and may not be reliable like the other tests that measured a flame.

The lack of major temperature shift can be attributed to the fundamentals of a diffusion flame. In the diffusion flame, the fuel reacts when there is enough oxidizer locally around the particle. Therefore, even if the bulk stoichiometry is changed, the particle will still react at the same temperature, but the amount of particles that react will change. Also, in the view path of the spectrometer, the hottest (and broadest) particle emission will mask the other cooler temperatures. Even if only a few particles react, the measured emission will correspond to those temperatures.

It was difficult to determine any temperature trends with respect to equivalence ratio. In the early high velocity tests, there was not a flame structure, and therefore no way to consistently compare reaction zones from one test to another.

Effect of Microwave Power on the Flame

During various tests, the microwave power was turned off after combustion began to meet the requirement set for an igniter design. Once the power was turned off for Combustion Tests 17 and 18, the flame did not extinguish, but shifted downward in the tube approximately 8 inches, shown in Figure 5-21. In each setup, there is a residence time based on the mixing of the aluminum and air. These two tests had relatively low oxidizer flow, which indicates less shear

mixing and explains the shift in flame. These tests also indicated that the plasma is critical in initiating the reaction. Even if the reactants are not mixed entirely, the filaments begin the reaction and provide enough energy to continue the reaction as the oxidizer diffuses.

Figure 5-22 shows Combustion Test 31 in which ignition was achieved and, one second later, the microwave power was shut off. In this experiment, the equivalence ratio was lowered to 0.9 (1.7 in Combustion Test 17). The flame continued to burn for ≈ 8 seconds before the aluminum source was shut off. The ability for the device to have an anchored flame with only microwave power for ignition was a success. The two main parameters that affected the ability to anchor the flame are the oxidizer volumetric flow and the aluminum mass flow. Comparing the flame before and after the microwave power was shut off, one can easily see the difference in intensity of the burning aluminum. The flame also shifts down after power is stopped; however, it is only around 1/8 inch compared to the ≈ 8 inches in the previous tests. Mixing is significantly better as seen by the wide flame at the injector tip.

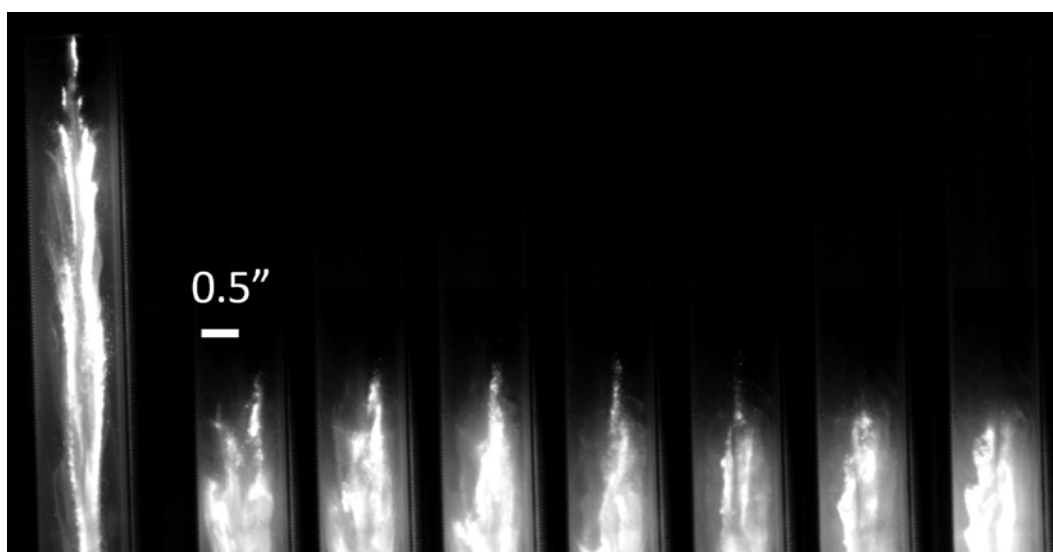


Figure 5-21. Shifting of Aluminum—Air Flame after Stopping Microwave Power — Combustion Test 17 — 2.5 ms Between Frames. In the fuel rich case, the flame lifted from the injector tip and stabilized around 8 inches down the quartz tube. Mixing is likely the reason for stabilization. The mixing time is significantly longer than that of the lean and near stoichiometric experiments.

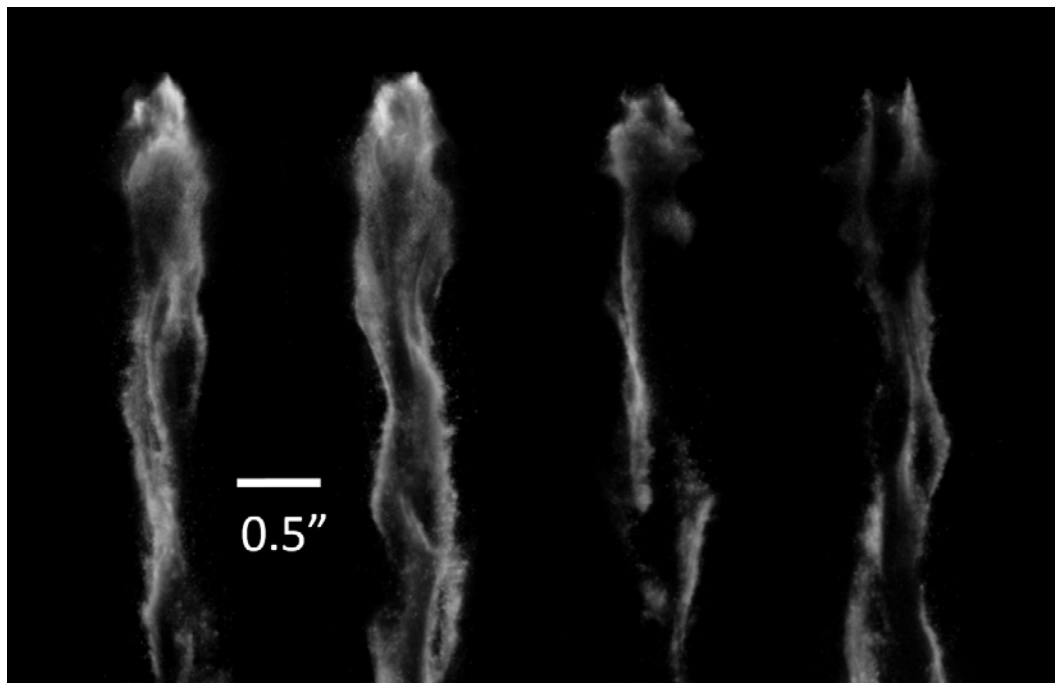


Figure 5-22. Combustion Test 31 — First Two Images with Microwave Power (200 W) Second Two Images No Microwave Power — 2.5 ms Between Frames. The intensity of the flame significantly decreases after the microwave power is turned off. The flame does continue to burn and stay attached to the injector tip, even without a plasma present.

When comparing the two tests seen above, the area right below the injector tip is significantly different. In Combustion Test 17, the flame begins as a thick filament region. Approximately; 1 inch below, the flame begins to spread take a more stable configuration. In Combustion Test 31 begins with a broad flame. The increased air flow seen in Combustion Test 31 is believed to significantly increase mixing and allow for quicker reactions to take place.

Additionally, during Combustion Test 31, temperature measurements were taken at the injector tip before and after the microwave power was turned off. There is a significant shift in temperature shown in Figure 5-23. Possible sources are that the flame slightly lifted off the injector making the region in the view slightly less reactive or the addition of microwave power may have enhanced combustion and provided higher temperatures. It does show that although not necessary in this configuration, the plasma enhances the reactions.

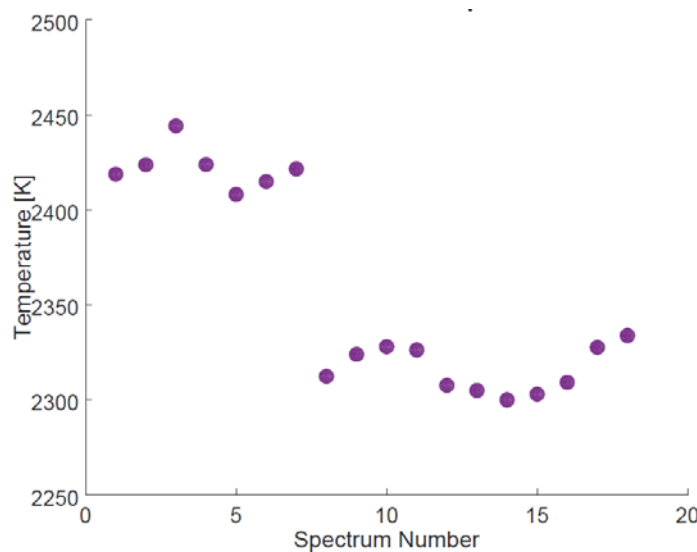


Figure 5-23. Combustion Test 31 — Temperature Difference with and Without Microwave Power. After microwave power is shut off, the temperature at the injector tip decreases significantly. This makes sense since less power is being introduced into the system and burning will take slightly longer.

Chemical Equilibrium Analysis

NASA's Chemical Equilibrium with Applications (CEA) code was used to determine approximate temperatures of the tests that were performed and to compare the accuracy of the temperature fittings. The inputs to the code are the reactants of combustion and then outputs the composition and temperature of the products at chemical equilibrium. The experimental tests will not be in complete equilibrium; however, it will still provide relative numbers that can then be compared.

The aluminum–air fuel rich case corresponding to Combustion Test 29–35 was performed in CEA and the results are shown in Table 5-5. The resultant temperature was 2537 K, which is slightly higher than measured using the temperature fitting. Reasons for this include that the reactants do not reach chemical equilibrium and no losses due to radiation are taken into account.

Table 5-5. CEA Reactants and Products for Combustion Test 29-35

REACTANT		MOLES	ENERGY	TEMP
			KJ/KG-MOL	K
FUEL	AL(cr)	0.0341000	-124.381	293.000
OXIDANT	Air	0.0422850	-275.387	293.000
NAME	Ar	0.0017897	-107.049	293.000
NAME	N2	0.0097000	-149.985	293.000

O/F= 0.96952 %FUEL= 50.773797 R,EQ.RATIO= 2.884451 PHI,EQ.RATIO= 2.887321

THERMODYNAMIC PROPERTIES

P, BAR	1.0132
T, K	2525.86
RHO, KG/CU M	2.1470-1
H, KJ/KG	-7.0466
U, KJ/KG	-478.99
G, KJ/KG	-17646
S, KJ/(KG)(K)	6.9833
M, (1/n)	44.499
MW, MOL WT	39.173
(dLV/dLP)t	-2.32156
(dLV/dLT)p	28.6114
Cp, KJ/(KG)(K)	109.0018
GAMMA _s	1.0889
SON VEL,M/SEC	716.9

MOLE FRACTIONS

*AL	0.04866
ALN	0.00001
*ALO	0.00007
AL2	0.00011
AL2O	0.16509
AL2O2	0.00004
*Ar	0.03441
*CO	0.00021
*N2	0.63170
ALN(L)	0.08173
AL2O3(L)	0.03796

Plasma Temperature Fitting

Specair is a software capable of temperature fitting emission spectra of plasma radiation. It was used to calculate the approximate electronic, rotational, translational, and vibrational temperatures of the argon plasma. Measurements of the argon plasma achieved in the low velocity configuration were taken at 2-mm intervals down the length of the plasma. The parameters of the flows measured were: 0.6 SLM argon in the center tube, 7 SLM of nitrogen in the swirl ports, and 200 W of microwave power. The wavelengths from 320–385 nm were chosen to be fit since that range contained nitrogen, one of the gases that could be fit. In this range of wavelengths, both the nitrogen second positive ($N_2(2+)$) and nitrogen first negative ($N_2(1-)$), were present. Figure 5-24 shows an example of the recorded spectra and a fitting of $N_2(2+)$ and $N_2(1-)$. Nitrogen is relatively reliable for measure plasma temperature due to its long excited lifespan.

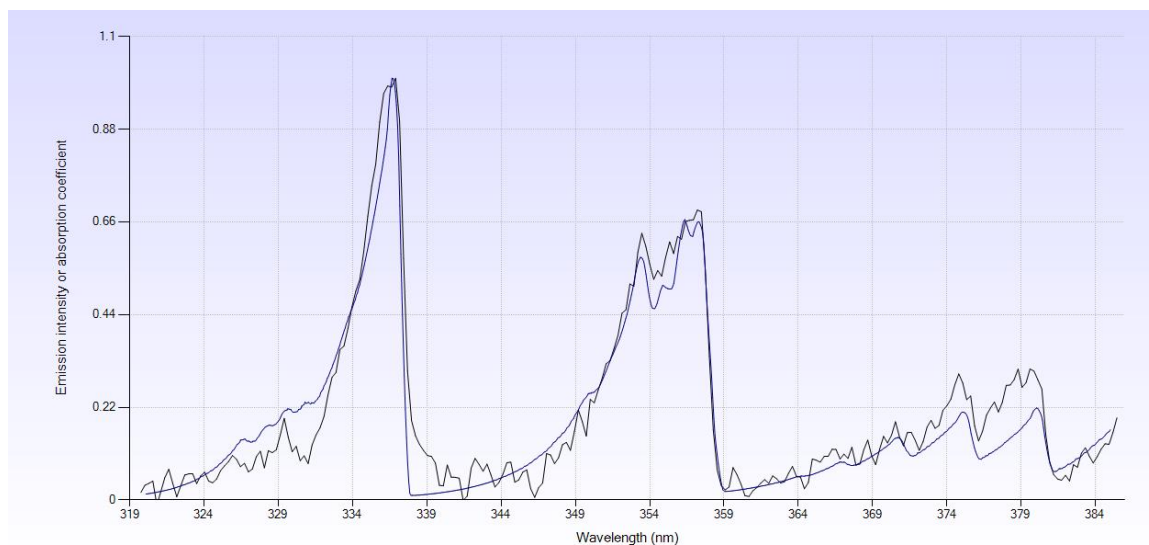


Figure 5-24. Example of Fitted Spectra in Specair — Raw Data (Black) and Fitted Curve (Blue).

Specair can import a spectra and can temperature fit the various modes available. In this case, nitrogen was used and fit $N_2(2+)$ and $N_2(1-)$. These are typically used when fitting plasmas due to their longevity. The argon plasma was approximately 2500-3500 K.

XRD

X-ray diffraction (XRD) along with post processing elemental fitting was used selectively during experimentation to examine the products of combustion. Specifically, the PANalytical Empyrean at Penn State's Millennium Science Center. Initially, the raw aluminum powder was tested to set a baseline.

Three separate aluminum peaks appeared in Figure 5-25, which was expected for the range of angles being scanned. Samples taken from the walls of the quartz tube from Combustion Test 39 were processed. Aluminum oxide peaks, shown in Figure 5-26, were found in the product sample; however, the aluminum lines were still very intense, indicating a low burning percentage of the particles deposited on the wall.

Since the samples were taken from the walls of the burner, the results may not accurately indicate the bulk amount of aluminum burned. A better indication would be examining the products in the bucket of water for the ventilation system. The powder collected was mostly white, indicating a large amount of aluminum oxide. Further XRD needs to be performed to verify the peaks in the collection bucket. However, complete combustion is not expected as this thesis focuses on an igniter design, not a combustor.

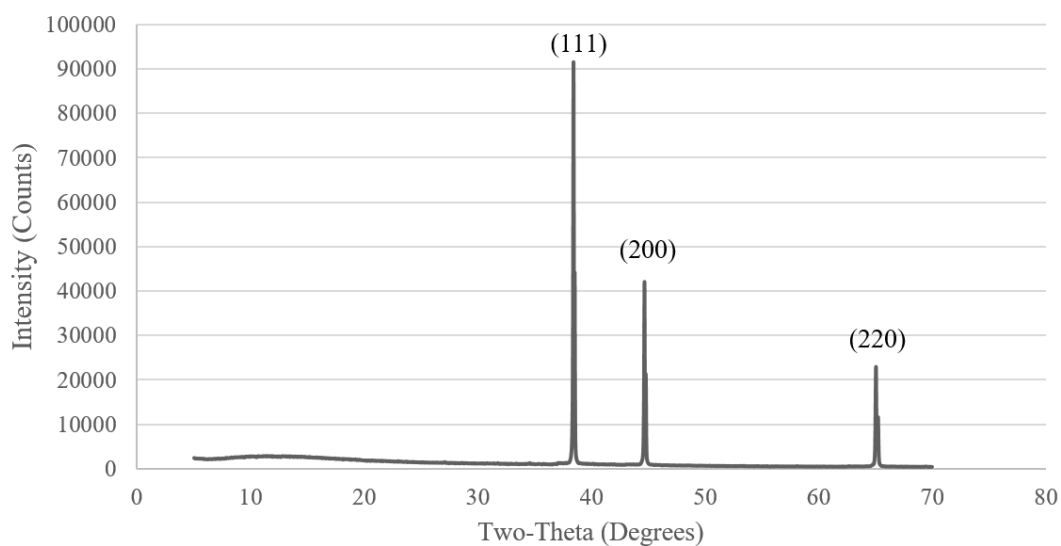


Figure 5-25. XRD Results from Raw Aluminum Sample. As expected, the raw aluminum only shows the three peaks.

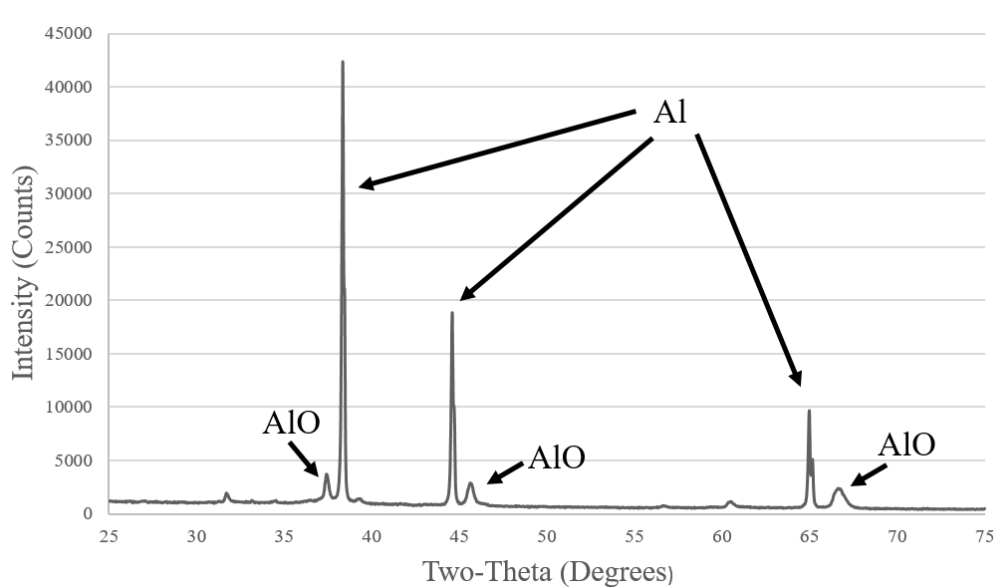


Figure 5-26. XRD Results from Burnt Combustion Products — Combustion Test 39. Combustion product results show aluminum as well as aluminum oxide lines. The aluminum oxide lines are short compared to the aluminum lines suggesting a small burning percentage. Further experiments need to be done to get a better sample of the bulk flow.

Chapter 6

Conclusions and Future Work

Conclusions

A successful configuration for a microwave argon plasma based aluminum igniter was developed and the physics between the aluminum – plasma filaments interaction were investigated. In the low velocity feeder configuration discussed above, the following flows produced the best conditions for an igniter: $\Phi = 0.9$, $u_0 = 8.8$ m/s (10° swirl), $u_i = 1.0$ m/s, and 200 W of microwave power with air in the outer flow and argon and aluminum powder in the core flow.

Of the three oxidizers used, air reacted more and allowed for a better flame structure than steam and carbon dioxide. The aluminum–air tests had several advantages: higher percentage of particles combusted, longer flame structure, and best interaction with the argon plasma structure. Although difficult, steam was ignited in both aluminum feeder configurations. A stable flame structure similar to that seen with air was achieved. Further investigation is needed to determine how to repeat that result. Aluminum–carbon dioxide provided a small but consistent flame. Both the steam and carbon dioxide tests only burn a small fraction of the aluminum provided due to the lack of free oxygen and lack of plasma interaction with the particles.

It was determined that the plasma filaments were above the 2300 K temperature needed to break the oxide shell of the aluminum particle to initiate the reaction. The optical emission of the argon plasma was temperature fit using the Specair software. The plasma had a rotational temperature of 2550–3650 K, which can be estimated as the thermal gas temperature of the plasma. This fitting showed that the plasma filaments were hot enough to melt the aluminum in the particle and crack the oxide shell. These results were confirmed experimentally by passing

aluminum particles through an argon plasma with no oxidizer. Particles were seen popping, which was due to the aluminum boiling and vaporizing, in addition to a strong blue light emitted from the reacting aluminum oxide shell. When this test was performed in the low velocity feeder configuration, the particles remained vaporized throughout the length of the quartz tube and reacted with the surrounding oxygen at the bottom of the tube. This test showed that vaporized particles remained in the vapor phase for the entire length scale of the igniter.

The thermal emission from the particles was fit using Planck's Law accounting for the emissivity change with respect to wavelength. For the optimal configuration, the particle temperatures reached 2414–2438 K. It is important to see that these particle were hotter than the 2300 K needed to break the oxide shell. Although the temperatures did not show any trends as far as equivalence ratio, they did match burning temperatures suggested in the literature.

Equivalence ratio did have an effect on the flame structure. At an equivalence ratio of 3.1, the flame was thin at the injector tip and did not develop a flame holding structure. It required about half the length of the tube before the flame widened. At equivalence ratios of 1.6 and 1.0, the flame structure was anchored around the injector. Anchoring of the flame provided one of the criteria set for a good injector design because the structure is better defined and less disturbed by instabilities. These values were set as a range of potential equivalence ratios that were possible to use. It should be noted that, in varying the equivalence ratio, the aluminum mass flow was held constant and the oxidizer flow was increased or decreased. The change in oxidizer flow caused a significant change in the velocity of the flow and thus the mixing. Although there is ambiguity as to which factor dominated, equivalence ratio or mixing, it can be said that the low mixing high equivalence ratio is not favorable, while the high mixing and slightly fuel rich configuration was successful. It was also shown that the igniter can work over a fairly large range of conditions, although it may not be optimized.

Through tests, it was determined that, for the lower equivalence ratio tests (1.0 and 1.6) that the microwave power could be shut off and the flame would remain burning and maintain a similar structure. This capability was another one of the criteria for a successful igniter. It is important that the plasma could be turned off to minimize the amount of power and hardware needed for successfully achieving ignition. It is also important to see that with certain equivalence ratios, the flame remained in the same location and did not lift off. Fittings of the temperature at the injector tip were made before and after the microwave power was turned off. The temperature shifted from ≈ 2425 K to ≈ 2300 K after the power was turned off. It is believed that the flame moved slightly down from the injector tip, as seen in the high speed video. In addition, the intensity of the flame diminished after the power was terminated. Although the flame continued without power, the flame seated on the injector better with the plasma on.

Future Work

To improve upon the current work of this thesis, tests should be performed at varying equivalence ratios, but maintaining the same relative velocities. The low velocity aluminum feed system would need to have its orifice size altered or another system developed altogether. In addition, it would be interesting to test the aluminum – steam combustion again with steam at approximately $400\text{ }^{\circ}\text{C}$ to determine if there was better success with no condensation. Potentially, heat from the aluminum reaction was being absorbed by condensed liquid water rather than being transferred to other particles. Further analysis should be completed to determine the percentage of unburned aluminum under a larger variety of conditions, specifically the amount of unburned aluminum when the plasma is on compared to the amount unburned when it was off.

Additionally, it would be interesting to investigate further if a microwave plasma can be used to separate the oxygen of CO_2 to increase the reaction rates.

To expand upon the microwave plasma aluminum igniter, it will be important to understand the effects of pressure on the igniter. In the current configuration, it would be difficult to pressurize everything including the waveguide. Other methods of coupling microwave energy into the coaxial burner should be explored. In a combustor application, the pressure would rise significantly to operating conditions. Potentially, the igniter would experience this high pressure during startup, or if needed to reignite the combustor.

It would be interesting to develop an experiment to measure the flame velocity of aluminum with and without a plasma present. A different setup that followed the propagation through a tube may be appropriate.

References

1. Babbitt, C., and Lindner, A., "A Life Cycle Inventory of Coal Used for Electricity Production in Florida," *Journal of Cleaner Production*, Vol. 13, No. 9, 2005.
2. Tadeusz, Z., "Metal Combustion Chamber to Generate Hot Gases, Particularly Propellants for Gas Turbine Installations," U.S. Patent: S2654219A, issued date June, 9, 1950.
3. Blomshield, F. S., "Lessons Learned In Solid Rocket Combustion Instability," *43rd AIAA/ASME/SAE/ASEE Joint Propulsion Conference & Exhibit*, 2007.
4. Glassman, I., "Metal Combustion Processes," *ARS Preprint No. 938-59*, AFOSR T.N. No. 59-1093, Princeton University Aero Eng'g Lab Report No. 473.
5. Yetter, R., A., Risha, G., A., and Son, S., F., "Metal Particle Combustion and Nanotechnology," *Combustion Institute*, Vol. 32, 2009, pp. 1819–1838.
6. Miller, T., F., Walter, J., L., and Kiely, D., H., "A Next-Generation AUV Energy System Based on Aluminum-Seawater Combustion," *Proceedings of the IEEE Symposium on Autonomous Underwater Vehicle Technology*, 111-119, 10.1109/AUV.2002.1177213.
7. Waters, D., F., Cadou, C., P., and Eagle, W., E., "Quantifying Unmanned Undersea Vehicle Range Improvement Enabled by Aluminum–Water Power System", *Journal of Propulsion and Power*, Vol. 29, No. 3, 2013, pp. 675-685.
8. Miller, T. F., Paul, M. V., and Oleson, S., R., "Combustion-based Power Source for Venus Surface Missions," *Acta Astronautica*, Volume 127, October–November 2016, Pages 197–208.
9. Glassman, I., and Yetter, R., "The Criterion for Vapor-Phase Combustion," *Combustion*, 4th Ed., Elsevier, Massachusetts, 2008.
10. Glassman, I., and Yetter, R., "Burning of Small Particles – Diffusion versus Kinetic Limits," *Combustion*, 4th Ed., Elsevier, Massachusetts, 2008.
11. Summerfield, M., and Krier, H., "Role of Aluminum in Suppressing Instability in Solid Propellant Rocket Motors," Princeton University, 1968.
12. Friedman, R., and Maček, "Ignition and Combustion of Aluminium Particles in Hot Ambient Gases," *A., Comb. and Flame*, 6, 9, 1962.
13. Friedman, R., Maček, A., "9th Symposium (International) on Combustion," *Academic Press*, 1963.
14. Bazyn, T., Krier, H., and Glumac, N., "Evidence for the Transition from the Diffusion-Limit in Aluminum Particle Combustion," *Proceedings of the Combustion Institute*, 31 II, 2021-2028. 2007.
15. Bucher, P., et al., "PLIF Species and Ratiometric Temperature Measurements of Aluminum Particle Combustion in O₂, CO₂ and N₂O Oxidizers, and Comparison with Model Calculations," *Proc. Combust. Inst.*, 27, 2421, 1998.
16. Yetter, R. A., and Dryer, F.L., "Microgravity Combustion: Fire in Free Fall," H. Ross, Ed., Academic Press, Chapter 6, 2001.
17. Goroshin, S., Bidabadi, M., and Lee, J.H.S., "Quenching Distance of Laminar Flame in Aluminum Dust Clouds," *Combustion and Flame*, Vol. 105, No. 1–2, 1996.
18. Goroshin, S., Fomenko, I., and Lee, J.H.S., "Burning Velocities in Fuel-Rich Aluminum Dust Clouds," *Twenty-Sixth Symposium (International) on Combustion/The Combustion Institute*, 1996/pp. 1961–1967.
19. Shoshin, Y., and Dreizin, E. L., "Laminar Lifted Flame Speed Measurements for Aerosols of Metals and Mechanical Alloys," *AIAA Journal*, Vol. 42, No. 7, July 2004.

20. Risha, G.A., Huang, Y., Yetter, R.A., and Yang, V., "Experimental Investigation of Aluminum Particle Dust Cloud Combustion," *43rd AIAA Aerospace Sciences Meeting and Exhibit*, 10 - 13 January 2005.
21. Beckstead, M. W., "A Summary of Aluminum Combustion," *RTO/VKI Special Course on 'Internal Aerodynamics in Solid Rocket Propulsion'*, RTO-EN-023, Utah, 2004.
22. Huang, Y., Risha, G., & Yang, V., and Yetter, R. A., "Analysis of Nano-Aluminum Particle Dust Cloud Combustion in Different Oxidizer Environments," *43rd AIAA Aerospace Sciences Meeting and Exhibit - Meeting Papers*. 10.2514/6.2005-738, 2005.
23. Washburn, E. B., Trivedi, J. N., Catoire, L., and Beckstead, M. W., "The Simulation of the Combustion of Micrometer-Sized Aluminum Particles with Steam," *Combustion Science and Technology*, 180:8, 1502-1517, 2008
24. Chen, F., *Introduction to Plasma Physics*. 1st edition, Plenum Press, New York, 1974, Chap. 1.
25. Phuoc, T. X., "Laser Spark Ignition: Experimental Determination of Laser-Induced Breakdown Thresholds of Combustion Gases," *Optics Communications*, Vol. 175, No. 4-6, 2000, Pages 419-423, ISSN 0030-4018.
26. Wang F. et al., "Transient Plasma Ignition of Quiescent and Flowing Air/Fuel Mixtures," *IEEE Transactions on Plasma Science*, Vol. 33, No. 2, pp. 844-849, April 2005.
27. Starikovskaia, S. M., "Plasma Assisted Ignition and Combustion," *J. Phys. D: Appl. Phys.* 39 R265, 2006.
28. Mintoussov, E.I., Pancheshnyi, Sergey and Starikovskii, A., "Propane-Air Flame Control by Non-Equilibrium Low-temperature Pulsed Nanosecond Barrier Discharge," *AIAA Paper*. 10.2514/6.2004-1013, 2004.
29. Reed, "Induction Coupled Plasma Torch," *Journal of Applied Physics*. 32. 821, 1961.
30. Musil, J., "Microwave Plasma: Its Characteristics and Applications in Thin Film Technology," *Vacuum*, Volume 36, Issues 1-3, Pages 161-169, ISSN 0042-207X, 1986.
31. Moisan, M. et al, "An Atmospheric Pressure Waveguide-Fed Microwave Plasma Torch: the TIA Design," *Plasma Sources Sci. Technol.* 3 584, 1994.
32. Uhm, H. S. et al, "A Microwave Plasma Torch and its Applications," *Plasma Sources Sci. Technol.* 15 S26, 2006.
33. Cullen, P. J., and Milosavljević, V., "Spectroscopic Characterization of a Radio-Frequency Argon Plasma Jet Discharge in Ambient Air," *Progress of Theoretical and Experimental Physics*, No. 063J01, 2015, pp. 1-17.
34. J. R. Fuhr and W. L. Wiese, *NIST Atomic Transition Probability Tables*, CRC Handbook of Chemistry & Physics, 77th Edition, D. R. Lide, Ed., CRC Press, Inc., Boca Raton, FL, 1996.
35. Ni, G., Zhao, P., Cheng, C., Song, Y., Toyoda, H., and Meng, Y., "Characterization of a Steam Plasma Jet at Atmospheric Pressure," *Plasma Sources Sci Technol* 2012;21:015009
36. Goroshin, S., Mamen, J., Higgins, A., Bazyn, T., Glumac, N., and Krier, H., "Emission Spectroscopy of Flame Fronts in Aluminum Suspensions," *Proceedings of the Combustion Institute*, Vol. 31, No. 2, 2007, Pages 2011-2019, ISSN 1540-7489,
37. H.G. Wolfhard, and W.G. Parker, "A New Technique for the Spectroscopic Examination of Flames at Normal Pressures," *Proc. Phys. Soc. A* 62 (8), 523-529, 1949.
38. Kalman, J., Allen, D., Glumac, and N., Krier, H., "Optical Depth Effects on Aluminum Oxide Spectral Emissivity," *Journal of Thermophysics and Heat Transfer*, Vol. 29, No. 1 ,2015.
39. Ermakov, V. A., Razdobreev, A. A., Skorik, A. I., Pozdeev, V. V., and Smolyakov, S. S., "Temperature of Aluminum Particles at the Time of Ignition and Combustion," *Combustion, Explosion and Shock Waves*, Vol. 18, No. 2, 1982.
40. Lee, S., Noh, K., Lim, J., and Yoon, W., "A Steam-Plasma Igniter for Aluminum Powder Combustion," *Plasma Science and Technology*, Vol. 17, No. 5, May 2015.

41. Palomino, J.,E., "Ignition of Aluminum Powder with A 2.45-GHz Microwave Plasma Torch (Master's Thesis)," Penn State University, 2016.
42. Dahm, W., Frieler, C., and Tryggvason, G., "Vortex Structure and Dynamics in the Near Field of a Coaxial Jet," *Journal of Fluid Mechanics*, 241, 1992.
43. Pierce, C., and Moin, P., "Progress-Variable Approach for Large-Eddy Simulation of Non-Premixed Turbulent Combustion," *Journal of Fluid Mechanics*, 504, 2004.
44. Risha, G. A., Huang, Y., Yetter, R. A., and Yang, V., "Experimental Investigation of Aluminum Particle Dust Cloud Combustion," *43rd AIAA Aerospace Sciences Meeting and Exhibit*, 2005.
45. Kwon, Y. S., Gromov, A. A., Ilyin, A. P., Popenko, E. M., and Rim, G. H., "The Mechanism of Combustion of Superfine Aluminum Powders," *Combustion and Flame* 133, 2003.
46. Conrads, H., and Schmidt, M., "Plasma Generation and Plasma Sources," *Plasma Sources Sci. Technol.* Vol. 9, 2000.

Appendix A

Aluminum – Steam Combustion Checklist

Date: _____

Test Description: _____

Aluminum Mass Flow (psi): _____

Steam Mass Flow (g/s): _____

Argon Plasma Mass Flow (SLM): _____

Nitrogen Swirl Mass Flow (SLM): _____

Microwave Power (W): _____

Boiler Pressure (psi): _____

Steam Temperature (°C): _____

Argon Thermocouple (°C): _____

Exposure Time: _____

Optics: _____

Spectrometer Height: _____

Preliminary Setup

- ☐ Ensure ceiling exhaust fan is on
- ☐ Turn on MKS programmer
- ☐ Fill boiler with DI water
- ☐ Make sure both valves are closed
- ☐ Ensure steam exhaust line is leading outside and not passing over anything that can melt
- ☐ Check air pressure in machine shop (≈ 90 psi)
- ☐ Check that the lab supply is open (On wall in machine shop near sink)
- ☐ Turn on air valve on wall in test cell
- ☐ Turn on pressure transducer
- ☐ Plug in boiler pug in Room 127 (hybrid room)
- ☐ Turn switch position to open and set knob to 90% above the pressure transducer
- ☐ Make sure red light in hybrid room is on
- ☐ Take aluminum filled tube and place it on the extender rod

- ☐ Check that the bottom holder is below the tube on the rod
- ☐ Assemble shearing device
- ☐ Carefully place over tube
- ☐ Secure with bolts
- ☐ Screw in bottom holder
- ☐ Connect line from shearing device to the Y union
- ☐ Check pressure of boiler and switch to “control”
- ☐ Set up appropriate cameras and DAQ (make sure there is enough space and is labeled correctly)
- ☐ Turn on controller, with enable disabled
- ☐ Turn on high power supply
- ☐ Open bottles of gas
- ☐ Open garage door

Pre-Test Run

- ☐ Turn on shop vac
- ☐ Run Argon plasma alone for a period (annulus)
- ☐ Turn off plasma
- ☐ Turn on both heating tapes
- ☐ Set desired temperature
- ☐ Ensure everyone is ready and in place
- ☐ Begin swirl flow
- ☐ Begin plasma flow
- ☐ Begin carrier gas flow
- ☐ Begin steam flow
- ☐ Linear Rate of Actuator (#): _____
- ☐ Aluminum Mass Flow (g/s): _____
- ☐ Steam Mass Flow (g/s): _____
- ☐ Argon Plasma Flow (SLM): _____
- ☐ Carrier Gas Flow (SLM): _____
- ☐ Nitrogen Swirl Flow (SLM): _____
- ☐ Nitrogen Ejector Flow (SLM): _____
- ☐ Microwave Power (W): _____
- ☐ Boiler Pressure (psi): _____
- ☐ Heating Tape Temperature (°C): _____
- ☐ Steam Temperature Second Thermocouple (°C): _____
- ☐ Argon Line Thermocouple (°C): _____
- ☐ Exposure Time: _____
- ☐ Set microwave power
- ☐ Check that the plasma looks stable

DAQ

- ☐ Subtract the background of the spectra
- ☐ Set the appropriate exposure time, file save path and the amount of files that will be saved
- ☐ Set the trigger method to level
- ☐ **Place the software in recording mode (Red Floppy Disk)**
- ☐ For the high speed camera, start capturing on the camera software
- ☐ Ensure that the camera is in focus and the correct parameters are set

Testing

- ☐ Begin recording on the instrunet DAQ system
- ☐ Enable controller with feed set at 0
- ☐ Make sure data is being recorded
- ☐ Begin flow of aluminum

Post Test and Shut Down

- ☐ Stop flow of aluminum
- ☐ Set feed to 0
- ☐ Disable microwave power
- ☐ Turn off steam
- ☐ Turn off Argon
- ☐ Turn off Carrier gas
- ☐ Let Nitrogen swirl purge
- ☐ Stop recording
- ☐ Turn off heat tape
- ☐ Turn off boiler
- ☐ Disable controller for actuator
- ☐ Turn off magnetron
- ☐ Turn off shop vac
- ☐ Begin venting of steam (close black valve also)
- ☐ Turn off shop air
- ☐ Close gas bottles
- ☐ Unplug MKS
- ☐ Turn off fan
- ☐ Make sure data was named appropriately
- ☐ Transfer to project folder
- ☐ Add to weekly notebook sheet

Comments:

Appendix B

Aluminum – Air Procedure

Before beginning any test, the coaxial injector system should be examined for damage and cleaned of residue from previous tests. Judgement will need to be used for any damage on the outer tubing. It has been seen in previous tests that damage, when severe enough, significantly affects the plasma structure. When adjusting components in coaxial injector, it is important to make sure the inner and outer tubing is coplanar. Again, when placing the top adapter plate back on the waveguide, place the injector tip coplanar with the bottom of the bottom adapter plate. Aligning these maximizes the microwave coupling. The quartz tube will need to be cleaned after each test. Dispose of the aluminum by-products properly. Then wash any remaining residue with common dish soap and the glassware brush kept near the sink in the machine shop. Usually this is satisfactory. After many tests, aluminum may build up at the top. Either the tube needs to be flipped around, scrubbed with other chemicals or totally replaced. Once the coaxial injector and quartz tubing are reattached, check that all the gas lines are reattached as well.

The shop vac and other ventilation should now be setup. Move the shop-vac outside of the test cell and keep the garage door slightly cracked. Turn the overhead fan on. Place the plastic bucket filled with water directly under the quartz tube. At least a 1/4" should be left between the bottom of the quartz and the top of the water. This prevents backpressure from forming and affecting the fluid dynamics of the test. The hose of the shop-vac should be placed facing the top of the water to capture any dust or products that are not trapped by the water. The Nikon D90 can be placed on the tripod in the test cell. The two plugs for the solenoid and controller should be plugged in. The shop air to the test cell, high speed camera, shop-vac, flow programmer, and magnetron should all be turned on. All necessary gas bottles should be opened. If necessary, fill the aluminum feeder with powder. Setup the high speed camera by selecting the desired framerate and EDR values. Set the exposure $\approx 50\text{--}100$ microseconds to see plasma ignition. Once the plasma is in a desired structure, the exposure can be lowered to the appropriate amount. As of 5/4/18, the flowing channels are Channel 1 – air, Channel 3 – argon, Channel 4 – nitrogen.

A test data sheet should be printed out and the parameters of the test determined. Microwave power, air, argon and nitrogen volumetric flows, aluminum feeder pressure, optics location, and exposure time should all be determined and set on the respective instrument.

To set up the high speed camera for recording, open up the PCC software and select the live tab. Open up the camera under the pulldown tab. If the large red button says "Capture" click

on it to enter capture mode. This will erase the previous video. The setting for exposure and EDR can also be set from the computer as well as when the section of recording pre and post trigger.

In Ocean Optics, the spectrometer can be set up by first opening the software. On the left tab, set the desired integration time. Delete the background using the unlit lightbulb. Then click on the save setup button and create a new folder to save the files to. Then route the correct folder in the save setup, select numerical numbering of files, check the “save all files button”, make sure that the “stop after (#) files” is unchecked and set the record time to a large enough value. Once all settings are done, click apply and close out of that window. Click back over on the left and switch the trigger type to “level”. The spectra should freeze. Now the “record mode” button and the save button should turn red. The spectrometer will now record when triggered from LabVIEW.

Once a plasma is formed and all recording devices are set, the following sets should be performed for a combustion test. In the linear velocity dialog box, type “-1” which will trigger the high-speed camera and spectrometer. Immediately after pressing enter, switch the “Al Feed” on. When the test is complete, turn off the microwave power, turn off the “Al Feed”, and turn off the oxidizer. These are the most important for extinguishing the flame. Now the other flows can be turned off as well. Save the high-speed video.

Begin the procedure over again if more tests are to be run that day, or begin the shutdown procedure.

After the gas flows are off, close all bottles. Turn off the magnetron, shop air, and shop-vac and unplug the solenoid. The garage door can be closed after the room is considered properly vented. The ceiling fan can also be turned off. The bucket of water used for product collection will have to occasionally be evaporated to dispose of the solid products.

Appendix C

Thermal Fitting Code

```

clc
clear
close all

% constants
h = 6.626070040e-34; % J*s
k = 1.38064852e-23; % J/K
c = 3e8; % m/s
C1 = 2*h*c^2; % Planck's
C2 = h*c/k;
T_lamp = 2273; % [K] lamp calibration temperature
N = 18; % number of spectra

Run2_temp=importdata('Subt2_00210.txt','\t');
data(:,1) = Run2_temp.data;
Run3_temp=importdata('Subt2_00211.txt','\t');
data(:,2) = Run3_temp.data(:,1);
Run4_temp=importdata('Subt2_00212.txt','\t');
data(:,3) = Run4_temp.data(:,1);
Run5_temp=importdata('Subt2_00213.txt','\t');
data(:,4) = Run5_temp.data(:,1);
Run6_temp=importdata('Subt2_00214.txt','\t');
data(:,5) = Run6_temp.data(:,1);
Run7_temp=importdata('Subt2_00215.txt','\t');
data(:,6) = Run7_temp.data(:,1);
Run8_temp=importdata('Subt2_00216.txt','\t');
data(:,7) = Run8_temp.data(:,1);
Run9_temp=importdata('Subt2_00217.txt','\t');
data(:,8) = Run9_temp.data(:,1);
Run10_temp=importdata('Subt2_00218.txt','\t');
data(:,9) = Run10_temp.data(:,1);
Run11_temp=importdata('Subt2_00219.txt','\t');
data(:,10) = Run11_temp.data(:,1);
Run12_temp=importdata('Subt2_00220.txt','\t');
data(:,11) = Run12_temp.data(:,1);
Run13_temp=importdata('Subt2_00221.txt','\t');
data(:,12) = Run13_temp.data(:,1);
Run14_temp=importdata('Subt2_00222.txt','\t');
data(:,13) = Run14_temp.data(:,1);
Run15_temp=importdata('Subt2_00223.txt','\t');
data(:,14) = Run15_temp.data(:,1);
Run16_temp=importdata('Subt2_00224.txt','\t');
data(:,15) = Run16_temp.data(:,1);
Run17_temp=importdata('Subt2_00225.txt','\t');
data(:,16) = Run17_temp.data(:,1);
Run18_temp=importdata('Subt2_00226.txt','\t');
data(:,17) = Run18_temp.data(:,1);
Run19_temp=importdata('Subt2_00227.txt','\t');
data(:,18) = Run19_temp.data(:,1);

figure('color',[1 1 1]);
for i = 1:N
    plot(data(:,1,i),data(:,2,i)); hold on;
end
set(gca,'fontname','times new roman','fontsize',20)
xlabel('Wavelength [nm]'); ylabel('Signal'); title('Spectral Intensity')
xlim([200 1100]); ylim([0 16000])

T = zeros(N,1);
l_range_index = 1334:2711; % 550-900 nm
l_range = data(l_range_index,1,1); % wavelength range
data = data(l_range_index,:); % trims the raw data from 550 nm to 900 nm

```

```

TH_lamp_2000 = importdata('Subt2_11-58-33-239.txt','\t'); % read in calibration
data
TH_lamp_2000 = TH_lamp_2000.data(l_range_index,:); % cut calibration data to 550-
900 nm
e_lamp = Tungsten_Fil_Em(l_range,T_lamp); % find lamp emissvity
BB = e_lamp.*C1./(l_range/(1e9)).^(5).*(exp(C2./(l_range/(1e9))/T_lamp)-1).^(-1); %
BB emission at lamp temperature multiplied by the lamp emissivity
spec_cor = BB./TH_lamp_2000(:,2); % detection system spectral response correction
for i = 1:N
    spec_int = spec_cor.*data(:,2,i); % calculate corrected spectral intensity
    x = 1./l_range; % inverse of wavelength [1/nm]
    y = log(spec_int.*l_range.^6.4); % ln(intensity*wavelength^5/e(lambda))
    linCoeff(i,:) = polyfit(x,y,1); % calculate the slope of xx and yyy
    T(i) = -1.4388*10^7/linCoeff(i,1); % constant (C2) from Planck's Law divided
by slope to find temp
end

figure('color',[1 1 1]); plot(x,y,'color',[0, 0.4470, 0.7410],'linewidth',2); hold
on
plot(x,linCoeff(i,1)*x+linCoeff(i,2),'k'); xlim([min(x) max(x)])
set(gca,'fontname','times new roman','fontsize',20)
xlabel('1/\lambda [nm^-1]'); ylabel('ln(i\lambda^6.^4)'); title('Thermal-
Emission Fitting')
figure('color',[1 1 1]); sz = 120; c = [0.4940, 0.1840, 0.5560];
scatter(1:N,T,sz,c,'filled')
limits=axis([0,20,2000,2500])
set(gca,'fontname','times new roman','fontsize',36)
xlabel('Spectrum Number'); ylabel('Temperature [K]'); title('Thermal-Emission
Temperature')
figure('color',[1 1 1]); plot(x,y,'color',[0, 0.4470, 0.7410],'linewidth',2);
plot(l_range,spec_int)
set(gca,'fontname','times new roman','fontsize',20)
xlabel('Wavelength'); ylabel('Corrected Intensity'); title('Corrected Spectrum')
T

```

Appendix D

Calibrating a Spectrometer Using the Tungsten Filament Lamp at the HPCL

To calibrate a spectrometer for the visible and infrared, a tungsten lamp can be used. First, set up the spectrometer with a fiber optic cable and small collimating lens focused on the center of the filament, or the location marked for calibration. The temperature of the lamp is then set based on the current provided. For the strip lamp at the HPCL, the following values can be used:

Current [A]	Temperature [°C]
8.69	800
9.22	900
9.87	1000
10.63	1100
11.58	1200
12.7	1300
13.93	1400
15.31	1500
16.84	1600
18.46	1700
20.07	1800
21.76	1900
23.57	2000
25.49	2100
27.52	2200
29.6	2300

To measure the current accurately, a multimeter should be used to measure the voltage over a known precision resistor. Current can then be calculated. Once the desired temperature is set, record several spectra. Planck's law can then be used to calculate the actual thermal emission.

$$\ln \left(\frac{i_{\lambda,T} \times \lambda^5}{\varepsilon(\lambda,T)} \times 2\pi \times C_1 \right) = \frac{C_2}{\lambda T}$$

The following code was used for the tungsten emissivity:

```

function [e] = Tungsten_Fil_Em(lambda,T)

T_min = 2000; % K
T_max = 2800; % K

l_min = 500; % nm
l_max = 1000; % nm

T_range = 2000:200:2800; % K
e_max = [.462 .458 .453 .449 .447];
e_min = [.382 .379 .370 .367 .364];

if T < T_min
    e = interp1([l_min l_max],[e_max(1) e_min(1)],lambda);
elseif T > T_max
    e = interp1([l_min l_max],[e_max(5) e_min(5)],lambda);
else
    e_min2 = interp1(T_range,e_min,T);
    e_max2 = interp1(T_range,e_max,T);
    e = interp1([l_min l_max],[e_max2 e_min2],lambda,'linear','extrap');
end

```

The theoretical intensity can then be plotted after substituting the correct temperature and constants. The ratio of the theoretical intensity to the intensity captured by the spectrometer should then be found. This ratio can then be multiplied by future spectra to provide a linear response over wavelengths. The beginning of the code in Appendix C can be used to find a correction. Note that the correction will only work over the range of the thermal emission of the tungsten lamp. Wavelengths where intensity start to drop, or no intensity at all will be inaccurate.